Vol. 1, No. 1, March 2025
jams.hsu.ac.ir

JOURNAL OF APPLIED MATERIAL SCIENCE

Hakim Sabzevari University

JOURNAL OF
APPLIED
MATERIAL
SCIENCE
jams.hsu.ac.ir

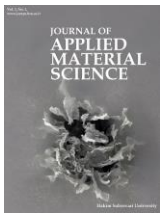

Contents

Volume 1, No. 1, March 2025

Editorial **210128**

Aims and scope of the journal, a brief submission guideline, and the list of the editorial board.

Ahmad Allahbakhsh

doi: 10.22034/jams.2025.210128

Graphene-Based Nanostructures for Future Dental Composites **210129**

This review paper provides a systematic overview of the latest advancements in the development of next-generation dental composites utilizing graphene, graphene-based nanostructures, and biomaterials. Allahbakhsh indicates that nanotoxicity is a significant barrier to the widespread use of graphene-based nanostructures in dental composites. He believes that addressing this issue could pave the way for new developments in future dental composites.

Ahmad Allahbakhsh

doi: 10.22034/jams.2024.210129

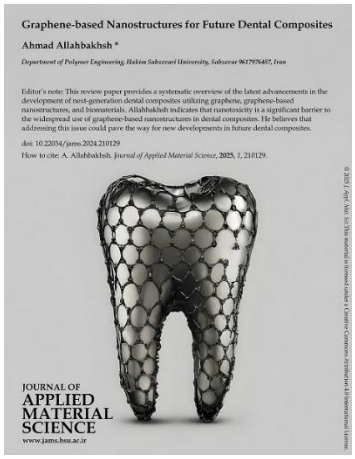

Tunable Morphology of Polyaniline/Multi-wall Carbon Nanotube for Organic Solar Cells **210130**

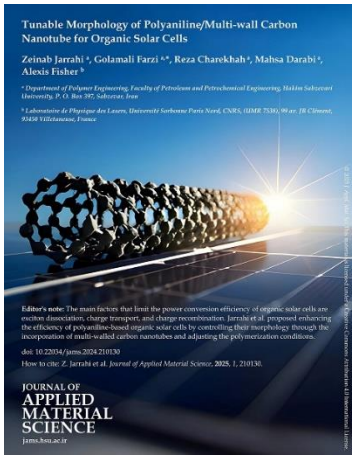

The main factors that limit the power conversion efficiency of organic solar cells are exciton dissociation, charge transport, and charge recombination. Jarrahi et al. proposed enhancing the efficiency of polyaniline-based organic solar cells by controlling their morphology through the incorporation of multi-walled carbon nanotubes and adjusting the polymerization conditions.

Zeinab Jarrahi, Golamali Farzi, Reza Charekhah, Mahsa Darabi, Alexis Fisher

doi: 10.22034/jams.2024.210130

© 2025 *J. Appl. Mat. Sci.* This material is licensed under a Creative Commons Attribution 4.0 International License.

An Overview of Silane-based Hybrid Sol-gel Coatings for Highly Efficient Metal Corrosion Protection 210131

This invited mini-review presents an overview of the corrosion protection potential of hybrid silane-based coatings applied through sol-gel fabrication on different metal substances. Sheydaei and Edraki focused on the environmental impact of such coatings and the importance of corrosion inhibitors on the final performance of silane-based corrosion protection systems for different application fields.

Milad Sheydaei, Milad Edraki

doi: 10.22034/jams.2024.210131

Mechanically Synthesized Zirconium-based MOFs for Adsorptive Removal of Nerve Agent Simulants 210132

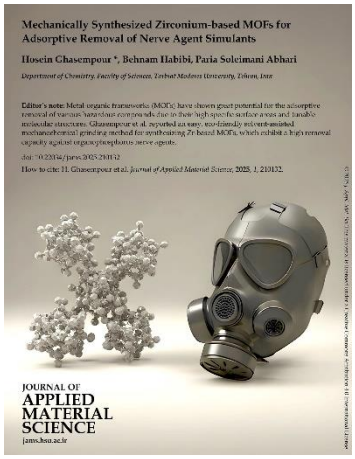

Metal-organic frameworks (MOFs) have shown great potential for the adsorptive removal of various hazardous compounds due to their high specific surface areas and tunable molecular structures. Ghasempour et al. reported an easy, eco-friendly solvent-assisted mechanochemical grinding method for synthesizing Zr-based MOFs, which exhibit a high removal capacity against organophosphorus nerve agents.

Hosein Ghasempour, Behnam Habibi, Paria Soleimani Abhari

doi: 10.22034/jams.2025.210132

Synthesis and Characterization of Novel Polyamide-imides Containing Thioether Linkages, Thiazole, and Nitrophenyl Units with High Solubility and Processability for Optical Film Applications 210133

Polyamide-imides (PAIs) are remarkable polymers that merge the beneficial properties of both polyamides and polyimides, making them suitable for various applications. Jalali synthesized a novel diimide-diacid monomer and utilized it to develop several sulfur-containing PAIs with high processability and solubility for optical film applications.

Aazam Jalali

doi: 10.22034/jams.2025.210133

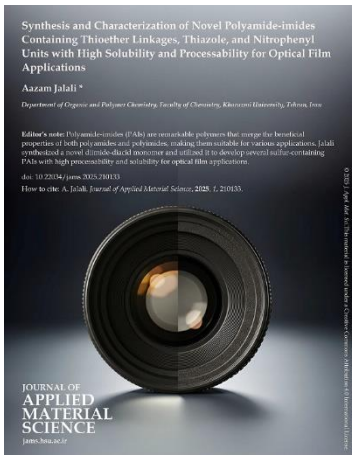

© 2025 *J. Appl. Mat. Sci.* This material is licensed under a Creative Commons Attribution 4.0 International License.

From Waste Polypropylene to Carbon Dots 210134

Converting plastics into advanced nanomaterials is an effective recycling strategy that addresses the growing problem of polymer waste, making it crucial for environmental sustainability. Mahdavian et al. introduced a two-step method to convert polypropylene waste from food packaging into carbon dots, which can be utilized in bioimaging, energy conversion, and sensing applications.

Faezeh Mahdavian, Haleh Naeim, Denis Rodrigue

doi: 10.22034/jams.2025.210134

ABOUT COVER

Graphene-based aerogels are three-dimensional, nanoporous materials characterized by high specific surface areas and customizable surface properties. Reduced graphene oxide (rGO) aerogels are a specific type of graphene-based aerogel typically created through the self-assembly of rGO nanosheets. The cover features a regenerated image based on a field emission scanning electron microscope (FESEM) image of an rGO aerogel, which was prepared using the hydrothermal reduction of graphene oxide nanosheets.

(Note: The covers of this journal are created in part using artificial intelligence (AI) technologies, with direct human supervision. AI and AI-assisted technologies are permitted only for generating graphical abstract suggestions. If such technologies are used in the manuscript preparation, it must be clearly disclosed in the Acknowledgments section.)

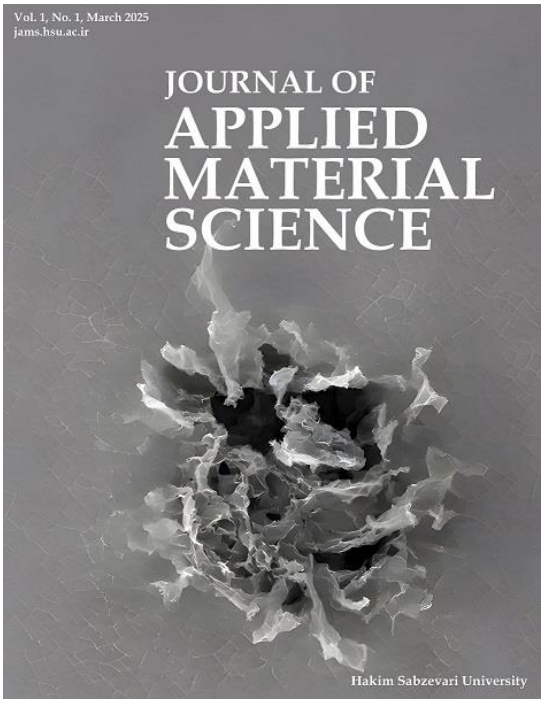

© 2025 *J. Appl. Mat. Sci.* This material is licensed under a Creative Commons Attribution 4.0 International License.

www.jams.hsu.ac.ir JOURNAL OF APPLIED MATERIAL SCIENCE

Journal of Applied Material Science:

a new *open-access* platform to publish scientific developments in all aspects of material science under the *highest publication qualities* and *the fastest peer-review process*

The new Journal of Applied Material Science, published by Hakim Sabzevari University, aims to cover a broad range of scientific discoveries in materials, polymers, biomaterials, nanomaterials, and advanced materials. Additionally, the journal provides a platform for researchers interested in exploring the interactions between living components and non-living materials, as well as between different classes of materials. The journal accepts scientific reports introducing innovative applications for new materials, covering device design and the use of materials in various applications. Additionally, the journal considers engineering materials and formulations related to the development of these materials.

The journal welcomes research on future materials and biomaterials, scientific reports on sustainable materials, biological materials, and living materials. It also encourages studies on drug delivery systems and all other aspects of bioengineering. Additionally, the journal accepts original research, review papers, and mini-reviews on the impact of different biomaterials on humans and the environment.

The Journal of Applied Material Science is seeking original research in the form of ***communications*** and ***full papers***, as well as ***reviews***, invited ***mini-reviews***, and invited research news. Dr. Ahmad Allahbakhsh, along with an international team of editors, leads the journal to meet the highest publication standards. We are looking forward to receiving your submissions.

Editor-in-Chief: Dr. Ahmad Allahbakhsh (Hakim Sabzevari University)

Director in charge: Prof. Gholamali Farzi (Hakim Sabzevari University)

International Editorial Board Members:

Prof. Ahmad Reza Bahramian (Tarbiat Modares University),
Prof. Mohammadhosein (Momo) Safari (Hasselt University),
Prof. Denis Rodrigue (Laval University),
Prof. Ursula Windberger (Medical University of Vienna),
Prof. Gholamali Farzi (Hakim Sabzevari University),
Dr. Ahmad Allahbakhsh (Hakim Sabzevari University)

To submit a manuscript: Please consult the aim and scope of the journal at:
https://jams.hsu.ac.ir/journal/aim_scope

Guide for Authors is available at: https://jams.hsu.ac.ir/journal/authors.note

To submit your paper, please visit: https://jams.hsu.ac.ir/contacts?_action=loginForm

https://doi.org/10.22034/jams.2025.210128
J. Appl. Mat. Sci., **2025**, *1*, 210128.
© 2025 *J. Appl. Mat. Sci.* This material is licensed under a Creative Commons Attribution 4.0 International License.

Graphene-based Nanostructures for Future Dental Composites

Ahmad Allahbakhsh *

Department of Polymer Engineering, Hakim Sabzevari University, Sabzevar 9617976487, Iran

Editor's note: This review paper provides a systematic overview of the latest advancements in the development of next-generation dental composites utilizing graphene, graphene-based nanostructures, and biomaterials. Allahbakhsh indicates that nanotoxicity is a significant barrier to the widespread use of graphene-based nanostructures in dental composites. He believes that addressing this issue could pave the way for new developments in future dental composites.

doi: 10.22034/jams.2024.210129

How to cite: A. Allahbakhsh. *Journal of Applied Material Science*, **2025**, *1*, 210129.

JOURNAL OF
APPLIED
MATERIAL
SCIENCE
www.jams.hsu.ac.ir

© 2025 *J. Appl. Mat. Sci.* This material is licensed under a Creative Commons Attribution 4.0 International License.

Journal of Applied Material Science **2025**, *1*, 210129
How to cite: A. Allahbakhsh, *Journal of Applied Material Science*, **2025**, *1*, 210129.
Journal homepage: **www.jams.hsu.ac.ir**

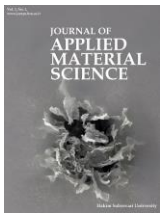

Review

Graphene-based Nanostructures for Future Dental Composites

Ahmad Allahbakhsh *

Department of Polymer Engineering, Hakim Sabzevari University, Sabzevar 9617976487, Iran

Abstract

Dental composites are becoming more important as an alternative to traditional dental materials. However, their low mechanical properties have limited their widespread use. Recently, there has been a lot of research interest in using graphene-based nanostructures to improve the mechanical properties of dental composites. The challenge now is to ensure that these future dental composites are biocompatible. This review paper provides an overview of the latest research on developing graphene-based dental composites, covering their structure, mechanical properties, and biocompatibility. It first gives a brief overview of dental composites and their structures, then introduces and compares different types of graphene-based nanostructures. Finally, the paper presents recent advances in developing graphene-based dental composites. The overview confirms that the mechanical properties of dental composites can be significantly improved by incorporating graphene-based nanosheets. However, further studies on other types of graphene-based nanostructures, specifically on the biocompatibility of these future dental composites, seem necessary.

Keywords: Graphene, Nanostructures, Dental composites, Biomaterials.

1. Introduction

Over the past few years, there has been a remarkable increase in research on the use of graphene-based nanostructures in dental restorations [1]. Graphene and its derivatives are being explored as promising materials for creating dental adhesives [2], substrates and scaffolds for dental pulp stem cells [3, 4], teeth whitening [5], dental implants [6, 7], dentin erosion protective coatings [8], and dental composites [9, 10]. The extensive potential applications of these materials stem from their impressive properties and their customizable nature [11]. The high surface area of graphene allows for easy modification of this material by adding different functionalities to its basal plane and edges [12]. Furthermore, 3D graphene-based nanostructures can be produced through the one-pot self-assembly of graphene derivatives [13]. Hence, graphene-based nanostructures could pave the way for the development of future dental materials, particularly dental composites.

Graphene-based nanostructures can be divided into three main categories [14]: (i) graphene-based nanosheets, which include graphene, graphene oxide (GO), reduced graphene oxide (rGO), and functionalized GO or rGO nanosheets, (ii) graphene-

* Corresponding authors.
Email addresses: a.allahbakhsh@hsu.ac.ir (A. Allahbakhsh)

Received 26 October 2024
Revised 2 December 2024
Accepted 2 December 2024
Available online 3 December 2024

https://doi.org/10.22034/jams.2024.210129
© 2025 The Authors. This article is licensed under a Creative Commons Attribution 4.0 International License.

based porous nanostructures, such as rGO and GO hydrogels, aerogels, and foams, and (iii) graphene-based composites. The latter type is widely used in the design of dental composites. In these composites, graphene-based nanostructures are dispersed in the structure of a polymeric resin used in dental composites [15]. Moreover, graphene-based porous nanostructures provide large specific surface areas and highly porous structures with very low densities, which can be beneficial for the development of lightweight dental composites [16].

Different classes of graphene-based nanostructures have already been used in the development of biomaterials and biosystems. However, nanotoxicity is the major limit for any biological applications of most graphene-based nanostructures [17]. Nanotoxicity in graphene-based nanostructures is closely related to the type and concentration of these materials [18]. Consequently, understanding the mechanisms involved in the nanotoxicity of graphene-based nanostructures can provide a roadmap to develop next-gen dental composites based on advanced nanostructures such as graphene-based nanostructures.

In this review paper, a systematic overview of the recent advances in the development of graphene-based dental composites is provided. The first section introduces dental composites, followed by an exploration of graphene-based nanostructures applicable to the design of dental composites. Finally, the recent advances in the development of high-performance graphene-based dental composites are covered.

2. Dental composites

The replacement of dental amalgams with dental composites has been increasingly accelerated in recent decades due to aesthetic and health reasons [19]. However, commercially available resin-based dental composites still have some significant shortcomings that require further research. One of the main drawbacks of dental composites is their lower mechanical properties compared to dental amalgams. The modulus of commercially available composites is about 30-50% lower than dentine [20]. Additionally, the average lifetime of dental composites is in the range of 3-5 years, which is much lower than that of amalgams (7-10 years). Issues such as hydrolysis of the filler due to water absorption and the release of chemical compounds over time are also significant concerns with current dental composite technologies [20]. Therefore, there is a clear need for more reliable dental composites with more advanced matrix and filler systems.

Dental composites have some key advantages, such as a tooth-like appearance, resistance to the oral environment, easy handling, and the ability to cure with light. However, they also have some drawbacks, including shrinkage during the curing process, the risk of secondary cavities, high thermal expansion, and low wear resistance [21]. Also, the leaching of uncured monomers due to an uneven curing process can be a significant concern in practical applications, as these monomers can cause cytotoxic effects in the surrounding gum tissues [22].

The main components of a dental composite formulation are (i) an organic matrix, usually based on 2,2-Bis[p-(20-hydroxy-30-methacryloxypropoxy)phenylene]propane (Bis-GMA) or 1,6-bis(methacryloxy-2-ethoxycarbonylamino) -2,4,4-trimethylhexane (UDMA) and the co-monomer triethylene glycol dimethacrylate(TEGDMA) to control viscosity, (ii) a reinforcing filler, such as clay, quartz, or fused silica, and (iii) a coupling agent, such as γ-methacryloxy propyltrimethoxysilane, to enhance bonding between the filler and resin matrix.

Recent studies suggest using nanomaterials instead of traditional reinforcing fillers to enhance the mechanical properties of dental composites [23]. Various types of nanomaterials such as nano clay [23], nano SiO2 [24], alumina [25], and different carbon nanomaterials [5, 26, 27] have been utilized in the development of dental composites. Among these materials, graphene-based nanostructures show great promise due to their superior mechanical properties and are considered for the development of next-gen dental composites [5, 28].

3. Graphene-based nanostructures

Graphene-based nanostructures have been a major focus in nanotechnology over the past decade. The unique structure of graphene nanosheets gives them exceptional properties, including a large surface area of 2630 m2/g, Young's modulus of approximately 1.0 TPa, and a breaking strength of around 40 N/m [29]. Moreover, the large surface area of graphene can be easily modified with different functionalities to achieve

© 2025 The Authors. This article is licensed under a Creative Commons Attribution 4.0 International License.

a wide range of surface chemistries with various properties. This tunable surface can be used to create high-performance resin-based nanocomposites with a high degree of compatibility between nanosheets and the polymeric matrix [30, 31]. More importantly, this customizable functionality can be utilized to impart important characteristics to resin-based composites, such as antibacterial properties [32], biocompatibility [28], and low toxicity [33]. This is a key reason for the significant research interest in graphene and its derivatives for biomedical applications [34, 35].

The unique surface functionality of GO can be utilized to create high-performance porous nanostructures with a large specific surface area and diverse surface chemistries [36]. These nanoporous platforms offer increased surface areas at low densities, resulting in enhanced mechanical properties and reduced resin shrinkages due to strong matrix-filler interactions [20]. Moreover, these structures can be easily converted to bioactive materials by impregnating their porous structure with different bioactive agents [20]. However, there is limited studies on the application of graphene-based porous nanostructures in dental materials, and only a few on graphene in fabricating dental composites.

4. Graphene-based dental composites

Both graphene oxide (GO) and nitrogen-doped graphene (N-graphene) show potential for use in dental composite applications [37]. However, reduced graphene oxide (rGO) may not be suitable for this application. In comparison to rGO nanosheets, GO nanosheets have low cytotoxic effects and cause oxidative stress without damaging cell membranes [37]. Nitrogen-doped graphene nanosheets also have lower cytotoxic effects than rGO nanosheets. However, some antioxidant activity was observed for N-doped graphene nanosheets, especially at high doses [37].

GO nanosheets showed no effect on the cell cytoskeleton at concentrations ranging from 4-20 µg/mL [37]. In contrast, rGO nanosheets disrupted the microtubule network at a wide range of doses (4-40 µg/mL). Furthermore, condensation and loss of adhesion were reported at high doses of N-doped graphene nanosheets (40 mg/mL). Additionally, GO nanosheets demonstrate good biocompatibility in nanocomposite form, making them ideal candidates for the development of dental composites (Figure 1).

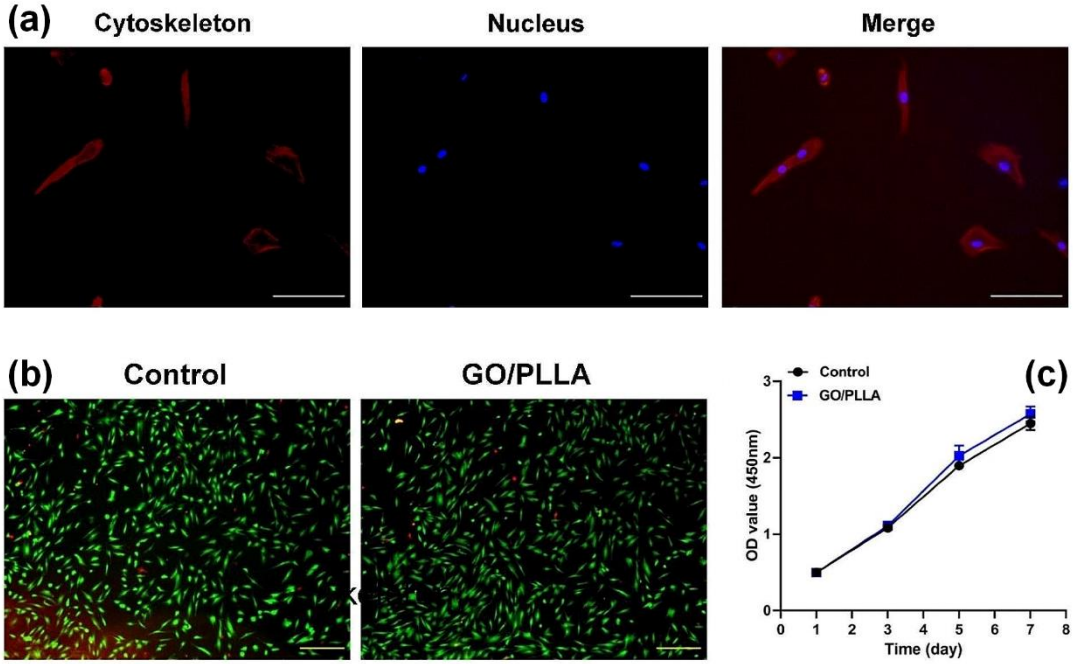

Figure 1. (a) The cytoskeleton staining results of dental pulp stem cells on composite scaffolds based on GO and poly-L-lactic acid (PLLA) with the cytoskeleton stained in red and the nucleus stained in blue, (b) fluorescence microscopic images of GO/PLLA scaffolds, (c) cell viability study of the GO/PLLA scaffold (scale bars in a and b panels show 200 and 500 µm, respectively) [4].

© 2025 The Authors. This article is licensed under a Creative Commons Attribution 4.0 International License.

As discussed earlier, graphene-based nanostructures can also be employed in fabricating dental adhesives [1]. Micro-cavities form between the healthy tissue and the dental composite due to the composite shrinkage can cause dental restoration failure, as bacteria can access dental tissues through these cavities [38]. Consequently, dental composites should be bonded to the hard tissues of teeth to make non-invasive caries removal achievable. Moreover, since biofilms play a major role in periodontal diseases, anti-biofilm dental adhesive can be a perfect strategy to overcome these issues. Anti-biofilm dental adhesives can be fabricated by embedding antibacterial agents in the adhesive material [39].

Graphene and its derivatives have been considered widely as antimicrobial materials and substrates and therefore, these nanostructures have a high potential to be employed in fabricating anti-biofilm adhesives. Three main mechanisms have been suggested for such a performance of these nanostructures. (1) These 2D structures can wrap the cells and induce mechanical stress, which leads to the prevention of nutrient uptake. (2) The sharp edges of these nanosheets can act as nano-knifes and disrupt the biofilm. (3) The oxidative stress production, which prevents the biofilm formation.

In a comparison between functionalized and unfunctionalized graphene nanosheets, it was found that oxygen-containing functional groups on the basal plane and edges of GO nanosheets can enhance the adhesion of bacteria to the nanosheet because surface structural defects increase biofilm adhesion to a surface [40]. However, while oxygen-containing functional groups can improve the compatibility between nanosheets and the polymeric matrix, these functionalities can also affect the cytotoxicity of nanosheets. Akhavan and Ghaderi [40] suggested that the higher antibacterial activity of the reduced form of nanosheets could be attributed to the improved charge transfer between the bacteria and the sharper edges of reduced nanosheets through nanosheet-bacteria interactions. This aligns closely with the findings of Bregnocchi and colleagues [41], who studied the antimicrobial and anti-biofilm performance (against *S. mutans*) of Bis-GMA-based dental adhesive composites in the presence of graphene nanosheets (Figure 2).

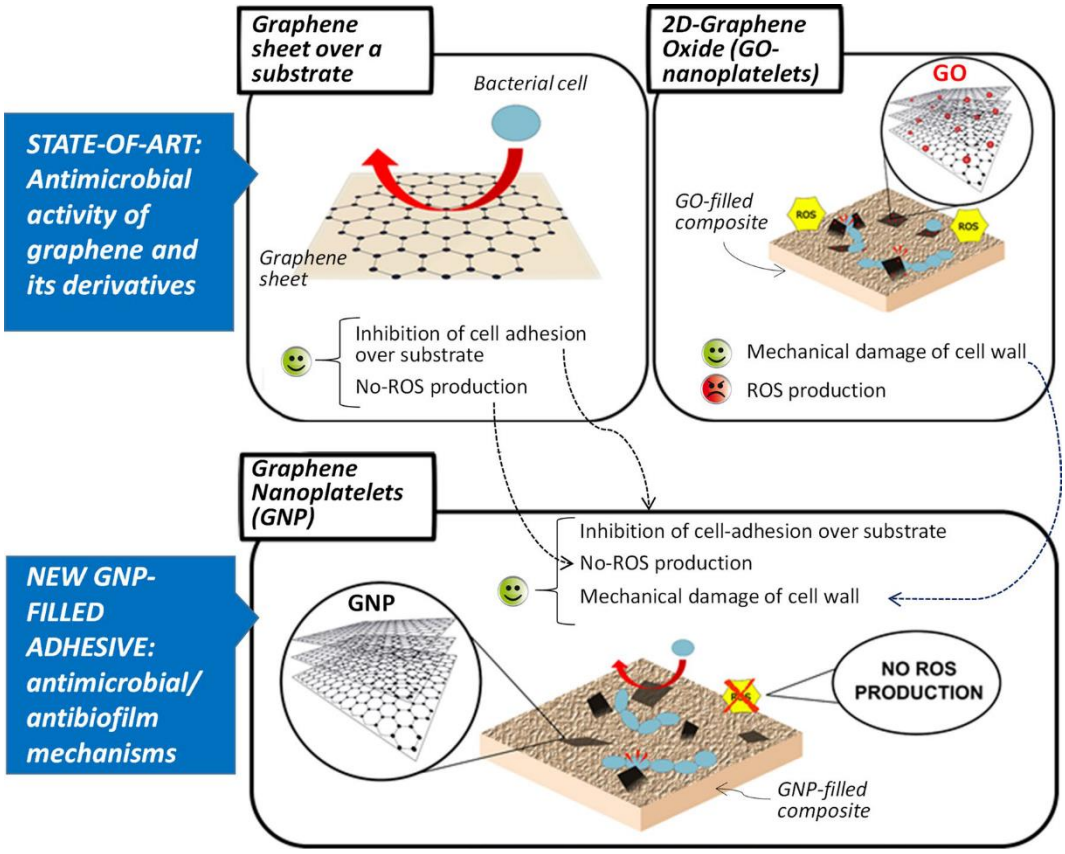

Figure 2. A schematic presentation for the anti-biofilm and antimicrobial characteristics of graphene, GO, and rGO nanosheets [41].

© 2025 The Authors. This article is licensed under a Creative Commons Attribution 4.0 International License.

Bregnocchi *et al.* [41] utilized 0.2%wt graphene nanosheets, which were prepared by thermally expanding graphite, to fabricate nanocomposite adhesive systems with anti-biofilm properties. The nanocomposite adhesive showed almost no difference in μ-TBS compared to a commercial adhesive. Using 0.2%wt graphene nanosheets led to a more than 50% reduction in biofilm formation (Figure 3). However, it was suggested to control the shear rate applied to the nanocomposite adhesive, as low shear rate regimes resulted in processing difficulties. The antibacterial properties of graphene-based dental composites are reported in Table 1.

Graphene-based nanosheets, including GO and rGO, can be further modified with functional groups such as grafting with polymeric agents like BisGMA-UDMA to improve compatibility with the resin matrix [45]. Such a grafting can extremely improve the compatibility between graphene-based nanosheets and the resin matrix. Additionally, silane surface modification has been found to be a promising technique for enhancing the compatibility of fillers and the matrix in dental composites [46, 47]. GO nanosheets can be surface-modified with silane modifiers to improve the compatibility of nanosheets and the polymeric matrix [48]. However, it is important to consider the

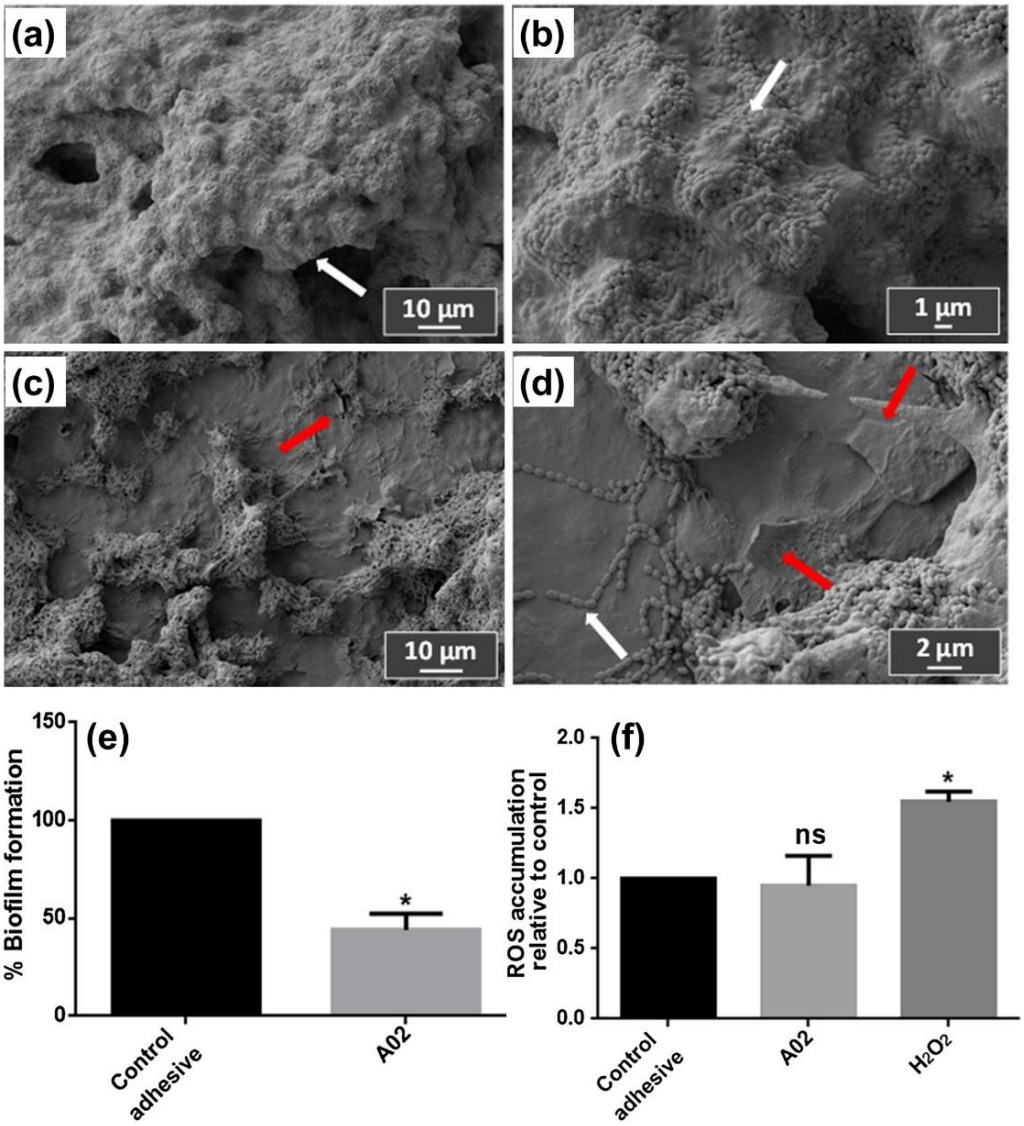

Figure 3. (a, b) Scanning electron microscopy (SEM) images of *S. mutans* biofilm growth on the teeth coated with the control adhesive and (c, d) a dental nanocomposite adhesive with 0.2wt% graphene nanosheets in the structure (A02), (e) biofilm formation percentage and (f) ROS accumulation of the A02 adhesive [41].

© 2025 The Authors. This article is licensed under a Creative Commons Attribution 4.0 International License.

Table 1. Antibacterial properties of different graphene-based nanostructures in dental composites

Resin	Nanomaterial	Concentration (wt.%)	antibacterial activity	Ref.
BisGMA/TEGDMA	GO-SiO2	1.8	*S. aureus*	[42]
BisGMA/HEMA	Graphene	0.2	*S. mutans*	[41]
PMMA	GO	2	*Candida albicans*	[43]
Glass ionomer cements	Fluorinated graphene	4	*S. aureus* and *S. mutans*	[44]
BisGMA/TEGDMA	GO	3	*S. mutans*	[9]

cytotoxicity of silane-based monomers when using them for surface modification of graphene-based nanosheets for dental composite applications [49].

The strong compatibility between nanosheets and the resin matrix not only affects the shrinkage of the dental composite but also its mechanical properties. Sun et al. [44] used a fluorinated graphene nanosheet system to enhance the mechanical properties, wear-resistance, and antibacterial characteristics of conventional glass ionomer cements (GICs) at low loading contents (0.5-4 wt.%). A hydrothermal synthesis process was utilized to synthesize fluorinated graphene powder from GO nanosheets using hydrofluoric acid and nitric acid. Results showed that employing only 2 wt.% of fluorinated graphene nanosheets led to more than 60% enhancement in microhardness and 59% enhancement in compressive strength of the dental composites. The study also reported a significant increase in inhibitory rates against *S. mutans* and *S. aureus* (up to 85.3% and 88.1% with 4 wt.% of fluorinated graphene, respectively) in the fluorinated graphene-incorporated dental composites. Additionally, the results revealed that fluorinated graphene nanosheets not only improve the mechanical properties but also enhance the tribological properties of dental composites [44].

Wear resistance is another important characteristic of dental composites in their clinical applications. Occlusion, chewing, and tooth brushing can cause wear of dental composites [50]. Previous research has primarily focused on improving the wear resistance of dental composites by enhancing resin crosslinking degree, filler size, and morphology [50, 51]. In addition, the bonding between the reinforcing agent and the polymeric resin (the filler/resin interface) also significantly affects the wear resistance of dental composites [51].

Apart from the discussed mechanical and anti-microbial properties, graphene-based nanostructures can significantly enhance the wear resistance of dental composites. Graphene nanosheets, whether in single- or few-layer forms, are known for their exceptional wear resistance, even under harsh sliding conditions [52]. Furthermore, incorporating graphene nanosheets into a polymeric matrix can significantly reduce the wear rate of the polymer [53]. This characteristic can significantly enhance the practicality of dental composites reinforced with this type of reinforcement.

As previously mentioned, the limited mechanical properties of commercially available dental composites are a major constraint to their widespread use. The incorporation of graphene-based nanostructures has the potential to improve this key aspect of dental composites, even at very low concentrations. In a study by Malik et al. [54], graphene nanosheets at a very low content (0.2 wt.%) were utilized to enhance the mechanical properties of a polyacrylic resin-based dental composite. While the study did not report the dispersion state of the nanosheets, the results indicated a significant improvement, with a more than 22% increase in compressive modulus and a 27% enhancement in compressive strength of the dental composite when enhanced with 0.2 wt.% graphene nanosheets [54].

Bacali et al. [55] proposed using a hybrid nanostructure filler composed of silver nanoparticles and graphene nanosheets to improve the mechanical properties of poly(methyl methacrylate) (PMMA) dental composites (Figure 4). They were able to achieve a perfect dispersion and distribution of the hybrid Ag-graphene nanofiller system in the polymeric matrix. While the modulus of the systems showed only a minor increase of less than 10%, there was a meaningful improvement in compressive strength [55]. It is possible to infer from their results that the suggested hybrid Ag-graphene nanosystem may have a more significant impact on enhancing PMMA-based dental materials if interactions between the nanosystem and the matrix are observed. Additionally, a higher ratio of graphene to silver in the hybrid nanosystem, proposed as the reinforcing phase in this study, could lead to better mechanical enhancements.

© 2025 The Authors. This article is licensed under a Creative Commons Attribution 4.0 International License.

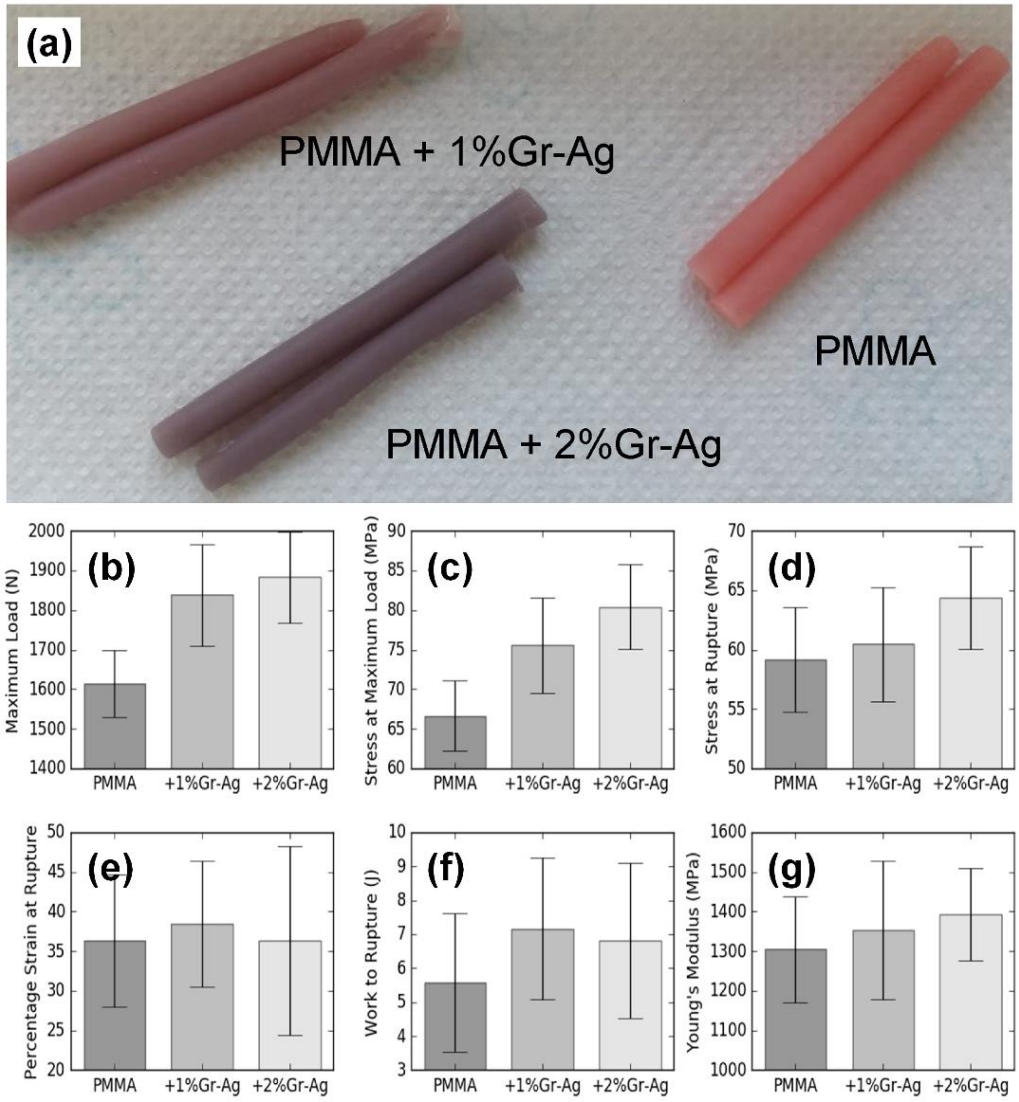

Figure 4. (a) a photograph showing the appearance of samples after curing; (b) maximum load, (c) stress at maximum load, (d) rupture stress, (e) rupture strain, (f) rupture work, and (g) Young's modulus of PMMA/graphene-Ag dental composites [55].

Moldovan et al. [56] investigated the use of GO-based filler systems in the development of dental composites. Specifically, they looked at GO-hydroxyapatite-SiO_2 (GS) and GO-hydroxyapatite-ZrO_2 (GZ) compared to a hydroxyapatite-Ag (CC) filler system. These composites were based on the Bis-GMA/TEGDMA matrix systems. The researchers used γ-methacryloxypropyltrimethoxysilane (A-174) to enhance the compatibility of the polymeric resin and nanofiller systems. They focused on evaluating the color stability of the dental composites when exposed to coffee and red wine, as well as assessing their antibacterial activity (Figure 5).

The color stability of dental composites was enhanced by using GO nanosheets. In comparison to the CC filler system, which exhibited the least stability, the GS filler system showed the greatest improvement in color stability of the dental composite, followed by the dental composite filled with the GZ filler system. Additionally, according to atomic force microscopy (AFM) studies, the dental composite filled with the GZ filler system demonstrated the best resistance to surface roughness and erosion, followed by the GS filler system [56].

The antibacterial properties of dental composites filled with different filler systems against *Staphylococcus*

© 2025 The Authors. This article is licensed under a Creative Commons Attribution 4.0 International License.

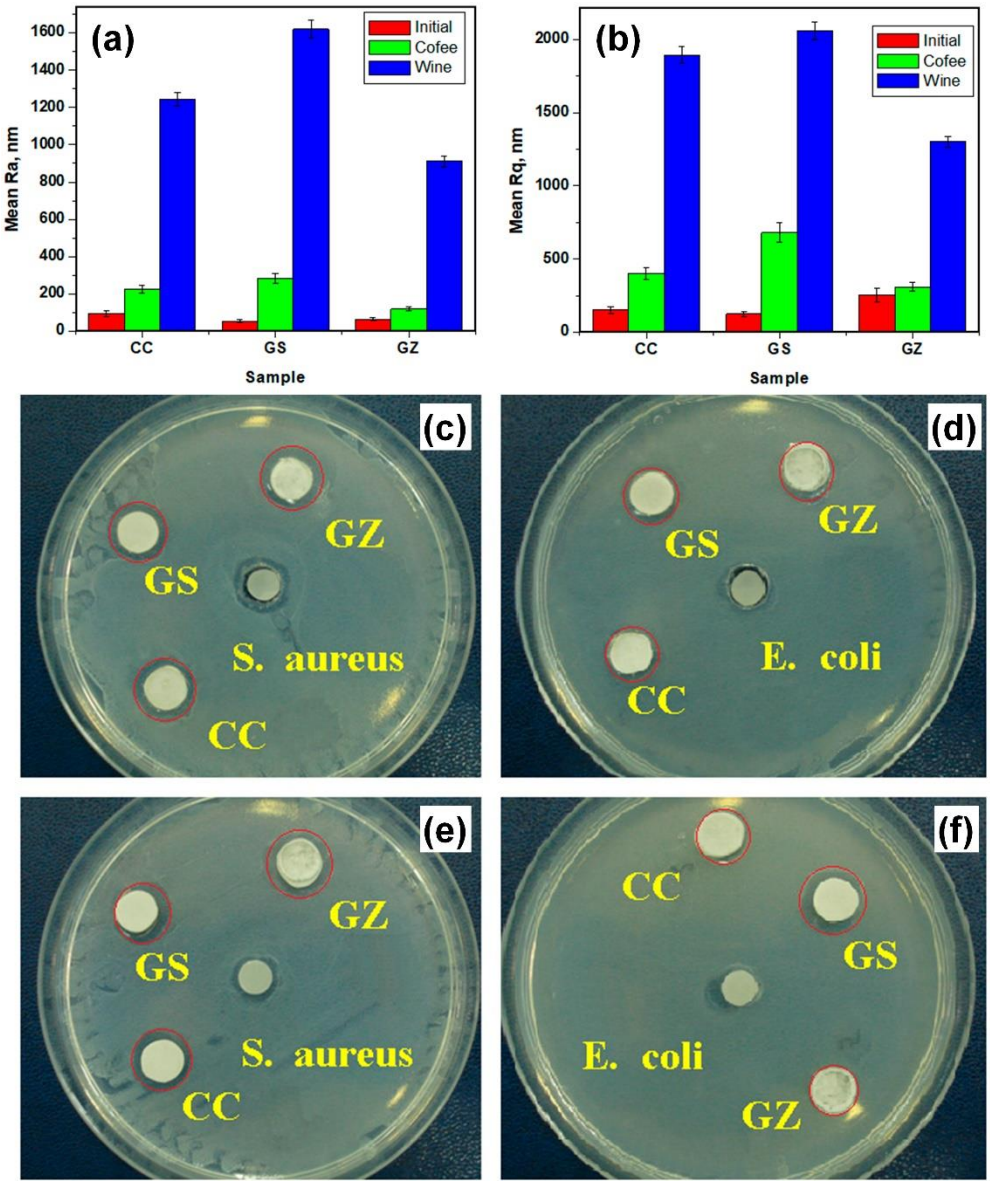

Figure 5. (a) Average roughness (R_a) and (b) root mean square roughness (R_q) of dental composites filled with GO-hydroxyapatite-SiO_2 (GS), GO-hydroxyapatite-ZrO_2 (GZ), and hydroxyapatite-Ag (CC) filler systems. Additionally, it includes disk diffusion (c, d) and well diffusion (e, f) antibacterial activity assays of dental composites [56].

aureus (*S. aureus*) and *Escherichia coli* (*E. coli*) were influenced by the presence of GO nanosheets in the filler systems. The dental composite filled with the GS filler system exhibited the strongest antibacterial activity against both bacteria strains, as shown by the size of the bacteria growth inhibition zones in Figure 5. Additionally, the dental composite filled with the GZ filler system showed moderate antibacterial activity compared to the GS and CC filler systems. The authors proposed that by using various oxides (SiO_2 or ZrO_2) as additional fillers in the system, the antibacterial activity of the dental composites filled with GO nanosheets could be further enhanced [56].

As previously mentioned, the main challenge in using graphene-based nanostructures in dental composites is their biocompatibility [57-59]. Several *in vitro* and *in vivo* studies have focused on the biocompatibility of various types of graphene-based nanostructures in dental

© 2025 The Authors. This article is licensed under a Creative Commons Attribution 4.0 International License.

applications [60-62]. However, most biocompatibility studies on graphene-based nanostructures found in the literature are related to bone regeneration due to the novelty of the subject [63-65].

Experimental studies on dental composites containing 0.3% rGO/ZrO2 and 0.3% TiO2-Ag-GO fillers in a Bis-GMA/UDMA/TEGDMA matrix showed that there was no significant toxicity or inflammation (Figure 6). However, the results indicated some oxidative stress in groups filled with GO-loaded dental composites. The presence of fibrous reaction near the test material suggests a healing response of body tissues around implants or foreign materials [66]. However, the complete picture in this study suggests that the implantation of the graphene-loaded dental composite is well-tolerated and is associated with a normal healing response, including inflammation and bone formation [66].

5. Conclusions

This review paper provided an in-depth overview of the latest research on the development of graphene-based dental composites, covering their structures, mechanical properties, and biocompatibility. The overview confirmed that incorporating graphene-based nanosheets can significantly improve the mechanical

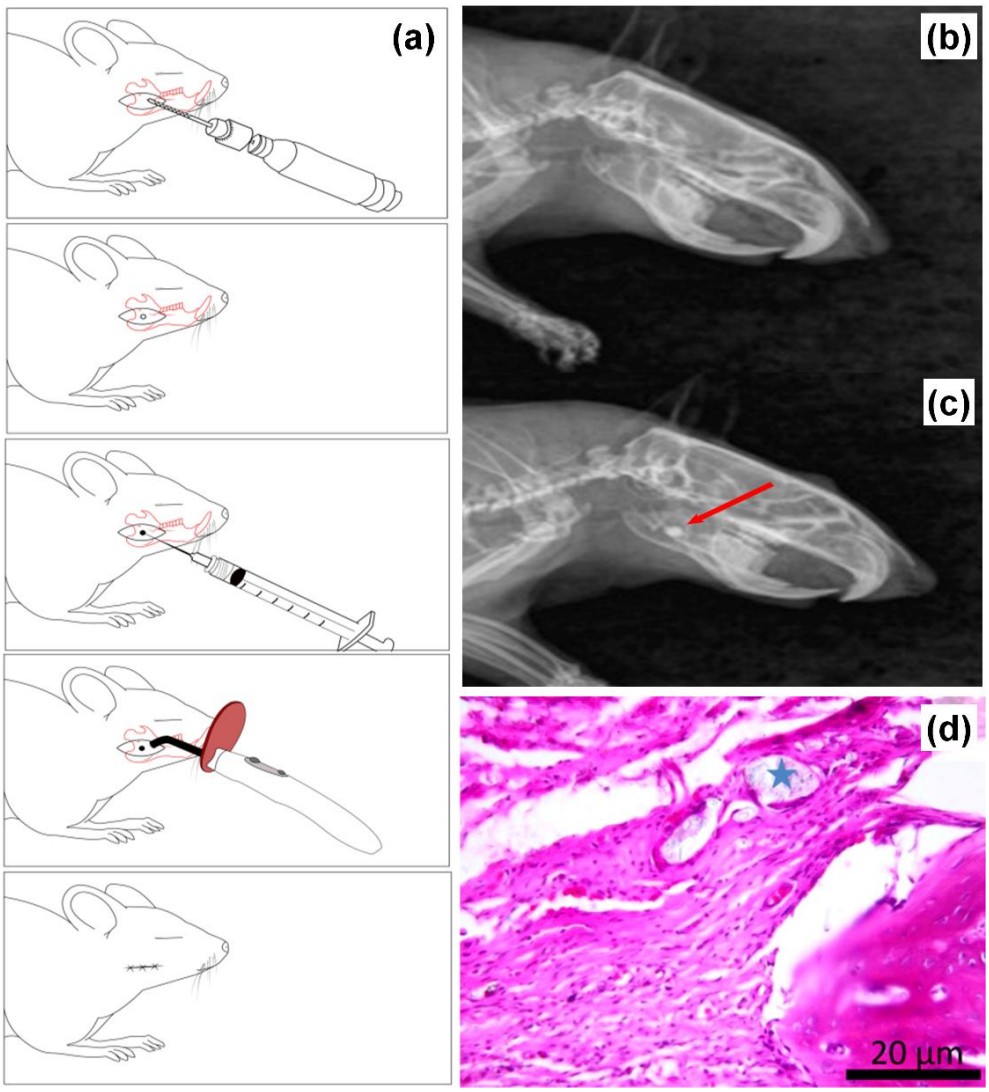

Figure 6. (a) The protocol followed for the in vivo experimental studies on graphene dental composites, the X-ray images of (b) control and (c) group filled with the graphene dental composite, and (d) fibrous reaction near the test graphene dental composite [66].

© 2025 The Authors. This article is licensed under a Creative Commons Attribution 4.0 International License.

properties of dental composites. Additionally, the discussions suggested that the biocompatibility of such dental composites has been proposed in the literature. However, the literature had limited content on graphene-based nanostructures and their types, making it difficult to reach a clear conclusion on the biocompatibility of graphene-based dental composites. Therefore, further exploration into other types of graphene-based nanostructures, particularly concerning the biocompatibility of these potential dental composites, seems necessary.

Acknowledgments

The author would like to acknowledge the support from the Research Department of Hakim Sabzevari University.

Conflict of Interest

The author declares no conflict of interest.

References

1. M. Roma and S. Hegde. Implications of graphene-based materials in dentistry: present and future. *Frontiers in Chemistry*, **2024**, *11*, 1308948.

2. S. Arslan, et al. Evaluation of the antibacterial activity of dental adhesive containing biogenic silver nanoparticles decorated nanographene oxide nanocomposites (Ag@nGO NCs) and effect on bond strength to dentine. *Odontology*, **2023**, *112*, 341.

3. S. López-García, et al. 3D Graphene/silk fibroin scaffolds enhance dental pulp stem cell osteo/odontogenic differentiation. *Dental Materials*, **2024**, *40*, 431.

4. Z. Qiu, et al. Effect of graphene oxide/ poly-L-lactic acid composite scaffold on the biological properties of human dental pulp stem cells. *BMC Oral Health*, **2024**, *24*, 413.

5. A.G. Williams, et al. Graphene-Based Materials in Dental Applications: Antibacterial, Biocompatible, and Bone Regenerative Properties. *International Journal of Biomaterials*, **2023**, *2023*, 1.

6. A. Al-Noaman and S.C.F. Rawlinson. A novel bioactive glass/graphene oxide composite coating for a polyether ether ketone-based dental implant. *European Journal of Oral Sciences*, **2023**, *131*, e12915.

7. X.-y. Zhang, et al. Antibacterial property of graphene quantum dots-modified TiO2 nanorods on titanium dental implant. *Transactions of Nonferrous Metals Society of China*, **2023**, *33*, 2395.

8. S. Nahorny, et al. Multi-walled carbon nanotubes/graphene oxide hybrid and nanohydroxyapatite composite: A novel coating to prevent dentin erosion. *Materials Science and Engineering: C*, **2017**, *79*, 199.

9. Z. Li, et al. Synthesis of ZnO Nanorod-Decorated Graphene Oxide for Application in Dental Resin Composites. *ACS Biomaterials Science & Engineering*, **2023**, *9*, 2706.

10. R. Wang, et al. Making graphene oxide (GO)-cladded SiO2 spheres (SiO2 @GO) as inorganic fillers for dental restorative resin composites. *Dental Materials*, **2023**, *39*, 1076.

11. A. Allahbakhsh, et al. Graphene-Based Engineered Living Materials. *Small Methods*, **2023**, *8*, 2300930.

12. M. Khalaj, et al. Structural, mechanical and thermal behaviors of novolac/graphene oxide nanocomposite aerogels. *Journal of Non-Crystalline Solids*, **2017**, *460*, 19.

13. A. Allahbakhsh, *Graphene-Based Advanced Nanostructures*, in *Handbook of Graphene*, E. Celasco, et al., Editors. **2019**, Wiley. 471.

14. A. Allahbakhsh, *High barrier graphene/polymer nanocomposite films*, in *Food Packaging*, A.M. Grumezescu, Editor. **2017**, Elsevier. 699.

15. M.H. Mobarak, et al. Advances of graphene nanoparticles in dental implant applications – A review. *Applied Surface Science Advances*, **2023**, *18*, 100470.

16. T. Shahnaz, et al. Graphene-based nanoarchitecture as a potent cushioning/filler in polymer composites and their applications. *Journal of Materials Research and Technology*, **2024**, *28*, 2671.

17. C. Kong, et al. Respiratory Toxicology of Graphene-Based Nanomaterials: A Review. *Toxics*, **2024**, *12*, 82.

18. Z. Gao, et al. Applications of graphene-based nanomaterials in drug design: The good, the bad and the ugly. *Expert Opinion on Drug Discovery*, **2023**, *18*, 1321.

19. A.A. Al-Asmar, et al. Clinical evaluation of reasons for replacement of amalgam vs composite posterior restorations. *The Saudi Dental Journal*, **2023**, *35*, 275.

20. S.B. Thorat, A. Diaspro, and M. Salerno. In vitro investigation of coupling-agent-free dental restorative composite based on nano-porous alumina fillers. *Journal of Dentistry*, **2014**, *42*, 279.

21. R. Yadav, et al. A comprehensive review: Physical, mechanical, and tribological characterization of dental resin composite materials. *Tribology International*, **2023**, *179*, 108102.

22. K.D. Jandt and B.W. Sigusch. Future perspectives of resin-based dental materials. *Dental Materials*, **2009**, *25*, 1001.

© 2025 The Authors. This article is licensed under a Creative Commons Attribution 4.0 International License.

23. A.K. Nikolaidis, et al. Synthesis and Characterization of Dental Nanocomposite Resins Filled with Different Clay Nanoparticles. *Polymers*, **2019**, *11*, 730.

24. J. Wang, et al. Study of POSS on the Properties of Novel Inorganic Dental Composite Resin. *Polymers*, **2020**, *12*, 478.

25. M.M.T. Piza, et al. Alumina-toughened zirconia nanocomposite: Aging effect on microstructural, optical, and mechanical properties. *Dental Materials*, **2023**, *39*, 1022.

26. N. Al-Harbi, et al. Bioactive hybrid membrane-based cellulose acetate/bioactive glass/hydroxyapatite/carbon nanotubes nanocomposite for dental applications. *Journal of the Mechanical Behavior of Biomedical Materials*, **2023**, *141*, 105795.

27. L. Shahkar, A. Malek Khachatourian, and A. Nemati. Fabrication and characterization of PMMA denture base nanocomposite reinforced with hydroxyapatite and multi-walled carbon nanotubes. *Diamond and Related Materials*, **2024**, *147*, 111377.

28. H. Xie, et al. Graphene for the development of the next-generation of biocomposites for dental and medical applications. *Dental Materials*, **2017**, *33*, 765.

29. D.G. Papageorgiou, I.A. Kinloch, and R.J. Young. Mechanical properties of graphene and graphene-based nanocomposites. *Progress in Materials Science*, **2017**, *90*, 75.

30. A. Allahbakhsh, et al. Poly(ethylene disulfide)/graphene oxide nanocomposites: Dynamic-mechanical and electrochemical properties. *European Polymer Journal*, **2020**, *130*, 109694.

31. A. Allahbakhsh. Polymethylene trisulfide/reduced graphene oxide nanocomposite electrodes: Deciphering microstructure/electrochemistry relationship. *European Polymer Journal*, **2024**, *215*, 113248.

32. J. He, et al. Killing Dental Pathogens Using Antibacterial Graphene Oxide. *ACS Applied Materials & Interfaces*, **2015**, *7*, 5605.

33. G. Reina, et al. Promises, facts and challenges for graphene in biomedical applications. *Chemical Society Reviews*, **2017**, *46*, 4400.

34. A. Allahbakhsh, et al. Three-dimensional nanoporous Cu-BTC/graphene oxide nanocomposites with engineered antibacterial properties synthesized via a one-pot solvosonication process. *Materials Chemistry and Physics*, **2022**, *277*, 125502.

35. A. Allahbakhsh, et al. Solar-powered and antibacterial water purification via Cu-BTC-embedded reduced graphene oxide nanocomposite aerogels. *Chemical Engineering Journal*, **2023**, *467*, 143472.

36. A. Allahbakhsh and A.R. Bahramian. Self-assembled and pyrolyzed carbon aerogels: an overview of their preparation mechanisms, properties and applications. *Nanoscale*, **2015**, *7*, 14139.

37. D. Olteanu, et al. Cytotoxicity assessment of graphene-based nanomaterials on human dental follicle stem cells. *Colloids and Surfaces B: Biointerfaces*, **2015**, *136*, 791.

38. A.M. Abraham and S. Venkatesan. A review on application of biomaterials for medical and dental implants. *Proceedings of the Institution of Mechanical Engineers, Part L: Journal of Materials: Design and Applications*, **2022**, *237*, 249.

39. H. Tebyaniyan, A. Hussain, and M. Vivian. Current Antibacterial Agents in Dental Bonding Systems: A Comprehensive Overview. *Future Microbiology*, **2023**, *18*, 825.

40. O. Akhavan and E. Ghaderi. Toxicity of Graphene and Graphene Oxide Nanowalls Against Bacteria. *ACS Nano*, **2010**, *4*, 5731.

41. A. Bregnocchi, et al. Graphene-based dental adhesive with anti-biofilm activity. *Journal of Nanobiotechnology*, **2017**, *15*, 89.

42. M. Moldovan, et al. Antibacterial activity and flexural strength for experimental composites with graphene. *Dental Materials*, **2017**, *33*, e54.

43. J.-H. Lee, et al. Nano-graphene oxide incorporated into PMMA resin to prevent microbial adhesion. *Dental Materials*, **2018**, *34*, e63.

44. L. Sun, et al. Improvement of the mechanical, tribological and antibacterial properties of glass ionomer cements by fluorinated graphene. *Dental Materials*, **2018**, *34*, e115.

45. M. Saleh Mohammadnia, S. Hemmati, and N. Ghasemi. Preparation of Reinforced poly (BisGMA-UDMA) Graphene-Based Nanocomposites Via Moderate in Situ SET-LRP. *Journal of Macromolecular Science, Part A*, **2017**, *55*, 49.

46. S.R. Kumar, A. Patnaik, and I.K. Bhat. Analysis of polymerization shrinkage and thermo-mechanical characterizations of resin-based dental composite reinforced with silane modified nanosilica filler particle. *Proceedings of the Institution of Mechanical Engineers, Part L: Journal of Materials: Design and Applications*, **2015**, *230*, 492.

47. F. Zhang, et al. Surface modification and microstructure of single-walled carbon nanotubes for dental resin-based composites. *Journal of Biomedical Materials Research Part B: Applied Biomaterials*, **2007**, *86B*, 90.

48. A. Allahbakhsh, et al. 3-Aminopropyl-triethoxysilane-functionalized rice husk and rice husk ash reinforced polyamide 6/graphene oxide sustainable nanocomposites. *European Polymer Journal*, **2017**, *94*, 417.

49. A. Aydınoğlu and A.B.H. Yoruç. Effects of silane-modified fillers on properties of dental composite resin. *Materials Science and Engineering: C*, **2017**, *79*, 382.

50. R. Wang, et al. Wear behavior of light-cured resin composites with bimodal silica nanostructures as fillers. *Materials Science and Engineering: C*, **2013**, *33*, 4759.

© 2025 The Authors. This article is licensed under a Creative Commons Attribution 4.0 International License.

51. Y. Tan, et al. Wear behavior of light-cured dental composites filled with porous glass–ceramic particles. *Journal of the Mechanical Behavior of Biomedical Materials*, **2010**, *3*, 77.

52. D. Berman, et al. Extraordinary Macroscale Wear Resistance of One Atom Thick Graphene Layer. *Advanced Functional Materials*, **2014**, *24*, 6640.

53. S.S. Kandanur, et al. Suppression of wear in graphene polymer composites. *Carbon*, **2012**, *50*, 3178.

54. S. Malik, et al. Graphene composites with dental and biomedical applicability. *Beilstein Journal of Nanotechnology*, **2018**, *9*, 801.

55. C. Bacali, et al. The Influence of Graphene in Improvement of Physico-Mechanical Properties in PMMA Denture Base Resins. *Materials*, **2019**, *12*, 2335.

56. M. Moldovan, et al. Chemical and Structural Assessment of New Dental Composites with Graphene Exposed to Staining Agents. *Journal of Functional Biomaterials*, **2023**, *14*, 163.

57. M. Tahriri, et al. Graphene and its derivatives: Opportunities and challenges in dentistry. *Materials Science and Engineering: C*, **2019**, *102*, 171.

58. M.Z.I. Nizami, S. Takashiba, and Y. Nishina. Graphene oxide: A new direction in dentistry. *Applied Materials Today*, **2020**, *19*.

59. L. Daneshmandi, et al. Graphene-Based Biomaterials for Bone Regenerative Engineering: A Comprehensive Review of the Field and Considerations Regarding Biocompatibility and Biodegradation. *Advanced Healthcare Materials*, **2020**, *10*, 2001414.

60. N. Mansouri, et al. Biodegradable and biocompatible graphene-based scaffolds for functional neural tissue engineering: A strategy approach using dental pulp stem cells and biomaterials. *Biotechnology and Bioengineering*, **2021**, *118*, 4217.

61. C. Bacali, et al. Flexural strength, biocompatibility, and antimicrobial activity of a polymethyl methacrylate denture resin enhanced with graphene and silver nanoparticles. *Clinical Oral Investigations*, **2019**, *24*, 2713.

62. A. Gholami, et al. Functionalization of Graphene Oxide Nanosheets Can Reduce Their Cytotoxicity to Dental Pulp Stem Cells. *Journal of Nanomaterials*, **2020**, *2020*, 1.

63. K. Kavitha, et al. Exploring the biocompatibility and healing activity of actinobacterial-enhanced reduced nano-graphene oxide in in vitro and in vivo model and induce bone regeneration through modulation of OPG/RANKL/RUNX2/ALP pathways. *Molecular Biology Reports*, **2024**, *51*, 702.

64. S.R. Silveira, et al. Osseointegration, antimicrobial capacity and cytotoxicity of implant materials coated with graphene compounds: A systematic review. *Japanese Dental Science Review*, **2023**, *59*, 303.

65. A.P.C. Souza, et al. Chitosan/Xanthan/Hydroxyapatite-graphene oxide porous scaffold associated with mesenchymal stem cells for dentin-pulp complex regeneration. *Journal of Biomaterials Applications*, **2023**, *37*, 1605.

66. A. Dreanca, et al. Systemic and Local Biocompatibility Assessment of Graphene Composite Dental Materials in Experimental Mandibular Bone Defect. *Materials*, **2020**, *13*, 2511.

Author Biography

Ahmad Allahbakhsh is an Assistant Professor and the Head of Department in the Department of Polymer Engineering at Hakim Sabzevari University. He received his Ph.D. in Polymer Engineering from Tarbiat Modares University in 2017. The research fields in which he has interest and expertise include graphene-based polymeric nanocomposites, graphene-based porous nanostructures, living materials, and sustainable polymer nanocomposites. He also works on graphene-based biomaterials, solar-to-thermal energy conversion systems and polymeric energy storage devices.

© 2025 The Authors. This article is licensed under a Creative Commons Attribution 4.0 International License.

Tunable Morphology of Polyaniline/Multi-wall Carbon Nanotube for Organic Solar Cells

Zeinab Jarrahi [a], Golamali Farzi [a,*], Reza Charekhah [a], Mahsa Darabi [a], Alexis Fisher [b]

[a] *Department of Polymer Engineering, Faculty of Petroleum and Petrochemical Engineering, Hakim Sabzevari University, P. O. Box 397, Sabzevar, Iran*

[b] *Laboratoire de Physique des Lasers, Université Sorbonne Paris Nord, CNRS, (UMR 7538), 99 av. JB Clément, 93450 Villetaneuse, France*

Editor's note: The main factors that limit the power conversion efficiency of organic solar cells are exciton dissociation, charge transport, and charge recombination. Jarrahi et al. proposed enhancing the efficiency of polyaniline-based organic solar cells by controlling their morphology through the incorporation of multi-walled carbon nanotubes and adjusting the polymerization conditions.

doi: 10.22034/jams.2024.210130

How to cite: Z. Jarrahi et al. *Journal of Applied Material Science*, **2025**, *1*, 210130.

JOURNAL OF
APPLIED
MATERIAL
SCIENCE
jams.hsu.ac.ir

© 2025 *J. Appl. Mat. Sci.* This material is licensed under a Creative Commons Attribution 4.0 International License.

Journal of Applied Material Science **2025**, *1*, 210130
How to cite: Z. Jarrahi et al., *Journal of Applied Material Science*, **2025**, *1*, 210130.
Journal homepage: **www.jams.hsu.ac.ir**

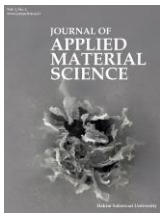

Original Research

Tunable Morphology of Polyaniline/Multi-wall Carbon Nanotube for Organic Solar Cells

Zeinab Jarrahi [a], Golamali Farzi [a,*], Reza Charekhah [a], Mahsa Darabi [a], Alexis Fisher [b]

[a] *Department of Polymer Engineering, Faculty of Petroleum and Petrochemical Engineering, Hakim Sabzevari University, P. O. Box 397, Sabzevar, Iran*

[b] *Laboratoire de Physique des Lasers, Université Sorbonne Paris Nord, CNRS, (UMR 7538), 99 av. JB Clément, 93450 Villetaneuse, France*

Abstract

Despite the great interest in applying polyaniline (PAni) in organic solar cells (OSCs), only a few studies deal with the morphology control of PAni-based OSCs. Here, comprehensive research has been conducted on the morphology control of PAni/multi-walled carbon nanotubes (MWCNTs) nanocomposites. Our results show that the morphology of PAni/MWCNTs can be tuned to tubular or cauliflower by controlling the synthesis parameters. The present study discusses the effect of the dopant's nature, the process's temperature, and the polymerization kinetics on the morphological dominance in the structure of PAni/MWCNTs nanocomposites. Also, the impact of the morphology of PAni/MWCNT on the efficiency of Photovoltaic cells based on these nanocomposites is investigated using Fourier transform-infrared spectroscopy, Hall effect measurements, UV-visible analyses for band gap measurements, and field emission scanning electron microscopy. The results revealed that by controlling morphology and achieving the desired morphology (tubular morphology), the conductivity of nanocomposite and mobility of the charge carriers increases. Consequently, it has been shown that the efficiency of PAni/MWCNTs OSCs increases due to the beneficial changes in short circuit current density, open voltage, and Fill Factor. Our results concluded that morphology control in synthesizing PAni/MWCNT nanocomposites plays a crucial role in the efficiency adjustment of the resultant photovoltaic devices.

Keywords: Polymer nanocomposites; Organic solar cells; Morphology control; Band gap.

1. Introduction

In recent decades, OSCs have garnered significant interest from researchers due to their lightweight nature, flexibility, cost-effective raw materials, and ease of processing. However, OSCs are challenged mostly due to their low efficiency [1-4]. The bottlenecks that limit the progress of power conversion efficiency for OSCs are exciton dissociation, charge transport, and charge recombination. [5-7] Hence, various approaches have

* Corresponding author.
Email addresses: farzi@hsu.ac.ir (G. Farzi)

Received 7 November 2024
Revised 18 December 2024
Accepted 25 December 2024
Available online 28 December 2024

https://doi.org/10.22034/jams.2024.210130
© 2025 The Authors. This article is licensed under a Creative Commons Attribution 4.0 International License.

attempted to improve these shortcomings [5, 8]. One strategy to accomplish this aim is incorporating carbon nanotubes (CNTs) into conducting polymers [9-14].

Conducting polymer/CNTs nanocomposites are a class of materials increasingly used in optical and electrical applications, particularly in polymer solar cells [15]. Effective utilization of CNTs for fabricating nanocomposites relies on the uniform dispersion of CNTs within the conductive polymer matrix. This uniformity optimizes the interfacial area for charge transfer between the CNTs and matrix [16, 17]. One effective method to achieve intimate dispersion of CNTs in a polymer matrix is in-situ polymerization [18].

Many polymers, such as polypyrrole, polyaniline (PAni), etc., have been used as matrix materials in these nanocomposites. Among these, polyaniline has been greatly considered due to the low cost and availability of raw materials, easy synthesis, relatively good environmental stability, high electrical conductivity, and simple doping/dedoping chemistry [19-25]. Polyaniline in emeraldine salt (ES) is synthesized through the oxidative polymerization of aniline using a chemical oxidant such as ammonium persulfate (APS) or ferric chloride (3FeCl), or via electrochemical oxidation in an acidic environment [25, 26].

Figure 1 illustrates the structure of each of the units of PAni, benzenoid diamine/quinoid diamine units, which are based on the reduction or the oxidation state. The formation of a charge-transfer complex between CNTs and polyaniline was demonstrated by the appearance of new absorption in the visible region [27]. Also, the observed enhanced conductivity effect was related to the fact that CNTs might serve as a conducting bridge between the PAni ES domains due to their large aspect ratio and surface area [28, 29].

Much research has been carried out on the conductivity of polyaniline/CNTs nanocomposites [28, 30]; however, to the best of our knowledge, there is no comprehensive investigation on the morphology control of these nanocomposites. The nanomorphology of BHJ blend films is at the center of the charge transfer process [31-33]. Controlling the nanomorphology in the active layer would improve the photocurrent conversion along with the FF [34] because efficient excitonic dissociation and charge transfer strongly depend on the fine morphology of the active layer [35, 36]. However, such performance can be improved when combined with device engineering.

Here, a comprehensive morphological study provides insight into different PAni/MWCNTs nanocomposite morphologies, including cauliflower (reported in our previous work [37]) and tubular. This was carried out by controlling several parameters influencing the aniline polymerization process. Then, in the next step, the active layer of the solar cell was fabricated based on polyaniline/MWCNTs nanocomposites, and the impact of the tuned morphology on the solar cell efficiency was understood. The physical and electrical properties of the two types of morphologies and their solar cells were comparatively investigated for a more in-depth insight. It was found that straw change in the synthesis parameters resulted in significant improvement of morphology and, consequently, the performance of the solar cell.

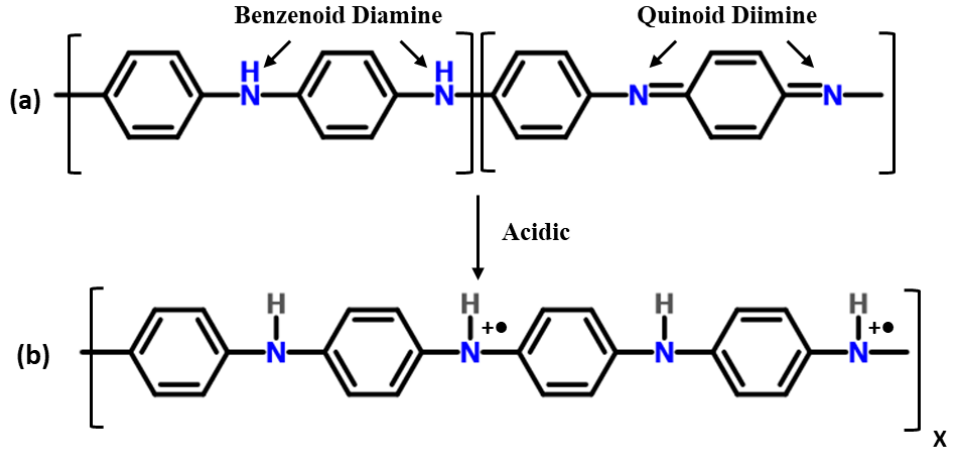

Figure 1. (a) Chemical structure of the undoped polyaniline (emeraldine base) and (b) its doped form (emeraldine base salt)

© 2025 The Authors. This article is licensed under a Creative Commons Attribution 4.0 International License.

2. Experimental

2.1. Materials

Aniline monomer (purchased from Merck), MWCNTs (multi-walled carbon nanotubes, with 20–30 nm diameter, 20 µm length, and density 2.1 g/cm³, purchased from Sigma-Aldrich), ammonium peroxydisulfate (APS, purchased from Merck), and p-toluene sulfonic acid (p-TSA, purchased from Sigma-Aldrich) were used as the starting materials. Several PAni/MWCNT nanocomposites were synthesized with varying MWCNTs weight percentages ranging from 0% to 10%. The two types of morphology, cauliflower and tubular, were obtained by controlling synthesis parameters such as temperature, ultrasonic duration, and reaction and polymerization rates. Multi-layer OSCs were fabricated using PAni/MWCNTs nanocomposites with different weight percentages of MWCNT. The detailed procedure for nanocomposite synthesis and solar cell fabrication has been reported in our previous work [37].

2.2. Measurements

FTIR (Fourier Transform Infrared Spectroscopy, PerkinElmer Spectrum Two) was utilized to identify the functional groups and chemical bonding within the nanocomposites, while UV-Visible Spectroscopy (Shimadzu UV-2600) provided insights into their optical absorption properties. Atomic Force Microscopy (AFM, Bruker Dimension Icon) was employed to study the surface morphology and roughness, and Thermal Gravimetric Analysis (TGA, TA Instruments Q500) was used to assess the thermal stability and decomposition behavior. Scanning Electron Microscopy (SEM, JEOL JSM-7610F) offered detailed morphological analysis to confirm the formation of nanostructures, and the Hall Effect technique (Keithley 2400) was applied to measure carrier concentration and mobility. Then, the photovoltaic and electrical properties of the fabricated solar cells were characterized by a I-V tracer (Sharif Solar IV-28) under the illumination of AM 1.5, 100 mWcm^{-2}.

3. Results and discussion

3.1. Synthesis and morphology control of tubular PAni/MWCNT nanocomposite

This section investigated the effects of synthesis parameters (the dopant's nature, the synthesis kinetics, and the synthesis temperature) on morphology control of PAni/MWCNT nanocomposites. Then, the band gap of the nanocomposites with either morphology (cauliflower / tubular morphologies) was compared.

Polyaniline (emeraldine base) is essentially different in some aspects, such as its behavior with other conjugated polymers [38]. Firstly, its structure is not conjugate and symmetric, so the energy band gap and Fermi level do not form in the center of the π-bond, so its conduction band and valence band are irregular. Its energy level position after dope differs from regular conjugated polymers, such as polyacetylene or polythiophene. Secondly, the carbon ring and nitrogen atoms are in their conjugate length and a polymer with an A-B structure; this is in contrast with that of polypyrrole or polythiophene, in which the non-main chain atoms are formed while they do not participate much in the formation of the π-bond. Thirdly, the emeraldine base can be converted from non-conductive to metal-like conductive by proton absorption in places N=, while the number of electrons is constant.

Figure 1 indicates an emeraldine base with an acid. The emeraldine salt state can form whose metallic features will be represented by creating a polar network in the structure. This feature will give rise to new optical and structural characteristics like the material. However, partial protonation can cause separation between protonated and non-protonated sites in the structure.

3.1.1. Nature of the dopant

The movement of electrons within the π-framework is the source of conductivity. However, a dopant is required to increase the level of conductivity for these nanocomposites [26]. In synthesizing PAni/MWCNT nanocomposite, suitable dopants for the cauliflower and tubular morphology are *p*-toluene sulfonic acid (*p*-TSA) and hydrochloric acid (HCl), respectively [37]. The process of HCl doping requires sodium dodecyl sulfate (SDS) to improve the dispersion of the carbon nanotubes in the polymer matrix. As seen in the map of electrostatic potential (MEP) in Figure 2, *p*-TSA acts with more surface dipole as a surfactant and does not require surface active materials, such as SDS, during its synthesis [39].

Because of the relatively high polarization of its molecules and, therefore, high attraction of its molecules to one another, non-doped polyaniline has low solubility, especially in non-polar solvents. This Van der

© 2025 The Authors. This article is licensed under a Creative Commons Attribution 4.0 International License.

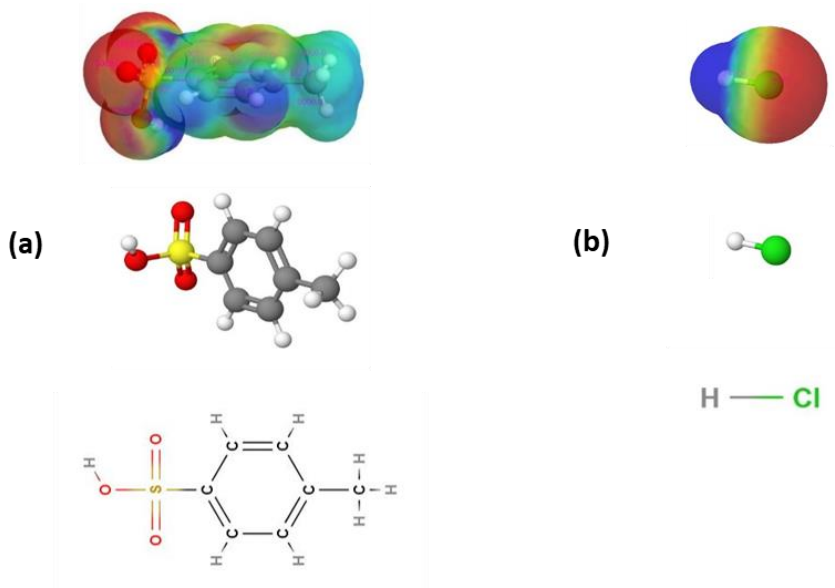

Figure 2. Molecular structure and MEP of (a) p-TSA and (b) HCl

Waals force between polyaniline molecules is such that even with its strong conventional polar solvents such as dimethylformamide (DMF) and N-methyl-2-pyrrolidone (NMP), non-doped polyaniline is not well solved and doped polyaniline has better solubility due to polarization changes and intermolecular force reduction [39].

In this context, a dopant such as *p*-TSA with a larger chain length than a small molecule such as HCl further reduces the polyaniline polarization, making it solvable more effectively by creating a greater gap between the molecules as a steric stabilizer agent. As shown in Figure 3, by increasing solubility, the separation of polyaniline chains in the synthesis environment increases, and the

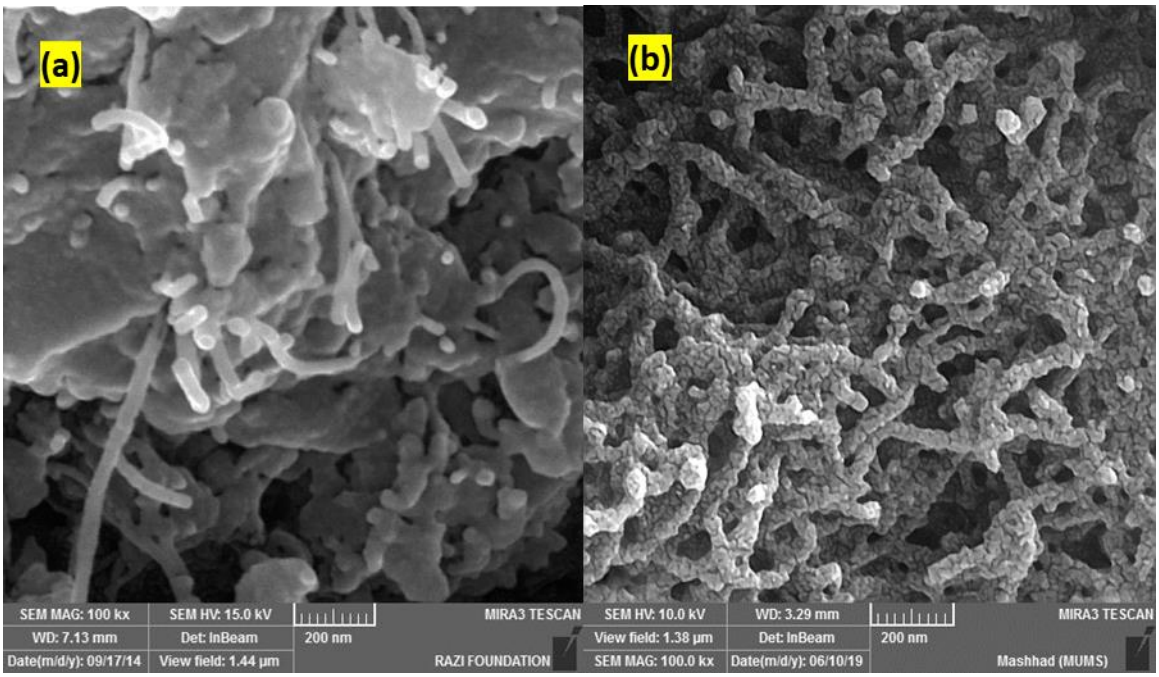

Figure 3. FESEM images of 10% MWCNTs/PAni: (a) cauliflower morphology by using HCl and (b) tubular morphology by using *p*-TSA.

© 2025 The Authors. This article is licensed under a Creative Commons Attribution 4.0 International License.

formation of large polyaniline masses (polyaniline coagulations) is reduced around the carbon nanotubes and, more specifically, on their surface. Therefore, the PAni/MWCNTs nanocomposite morphology changes from cauliflower to tubular, so that physical and photovoltaic properties are affected.

It was noted that polyaniline produced by doping with HCl had a higher conductivity than that produced by doping with *p*-TSA. The results obtained in a previous work by our group confirmed this issue, [37]. However, in the present study, after the synthesis of nanocomposites composed of CNTs and polyaniline, the results were reversed, and the conductivity of the nanocomposite produced by polyaniline doped with *p*-TSA was higher than HCl doped nanocomposite. The reason for this behavioral rotation could be that, in addition to the effect on the conductivity of polyaniline (due to the change of charge distribution in the aniline molecule and the effect on the movement of electrons in the length of conjugate bonds), the dopant also affected the morphology of the PAni/MWCNT nanocomposites and this could be due to the change in the interaction between polyaniline and nanotubes (depending on the nature of dopant and reaction condition). Therefore, although the use of *p*-TSA reduced the conductivity of pure polyaniline rather than the use of HCl, the resulting nanocomposite led to more electrons reaching into the preferred paths of carbon nanotubes due to the tubular morphology of low-amount polyaniline on the surface of the nanotubes, as shown in Figure 3b; thus, conductivity was higher than the doped nanocomposite with HCl due to the cauliflower morphology with high polyaniline thicknesses (greater domain size) and long paths for the electrons to reach the carbon nanotubes [40, 41]. In addition, increasing order in the polymer structure, more homogeneity, and the emergence of tubular morphology also increased the mobility of charge carriers [36].

Table 1 summarized the conductivity and electron mobility of nanocomposites with two morphologies achieved by Hall Effect measurement. As reported in this table, higher conductivity of the PAni/MWCNTs nanocomposite synthesized via *p*-TSA suggests that this nanocomposite is a better option for being used as the active layer leading to the improvement of photovoltaic characteristics due to tubular morphology (discussed below), increased solubility, as well as increased film formation ability, all of which are important parameters for fabricating solar cells.

The interaction between PAni and carbon nanotubes with different dopants can be investigated by examining the activity of the corresponding chemical bonds. Figure 4 shows the FTIR spectra of pure polyaniline (emeraldine salt), a cauliflower morphology 10% nanocomposite (doped by HCl), and a tubular morphology 10% nanocomposite (doped by *p*-TSA). As shown in Figure 4, peaks in the range 2897 cm^{-1} correspond to the S-O and C-H stretching in the benzenoid ring, peaks 551 and 657 cm^{-1} correspond to the C-H stretching vibrations, and also the presence of peaks 1044 of the $(SO_3)^-$ functional group, the peak of 750 cm^{-1} (stretching S-O) and the peak of 630 cm^{-1} (stretching C-S), which are related to the connection of $(SO_3)^-$ functional groups to the polyaniline aromatic rings confirm the presence of *p*-TSA in the nanocomposite (blue spectrum) in comparison with other spectra.

Also, the non-removal and maintenance of the ratio of quinoid and benzenoid peaks (1466 and 1559 cm^{-1}) representing polyaniline demonstrate π-interaction between the aromatic aniline and nanotube components and aniline absorption on the surface of the nanotubes in the nanocomposites (red and blue spectra). The wider peaks in this range indicate increased vibrational activity in their structure, and reducing the difference between quinoid and benzenoid peaks (i.e., increasing the intensity of quinoid peak) is due to the π-bonding of the carbon nanotube with the π-conjugated structure of polyaniline, particularly in quinoid units.

Peaks from 1125 cm^{-1} to 1148 cm^{-1} relate to the C-H plate bending vibrations formed during the polyaniline

Table 1. Conductivity and solubility of polyaniline synthesized with HCl and p-TSA in DMF, as well as conductivity and charge carrier of nanocomposites with two morphologies

Characteristic	PAni-HCl	Pani-*p*-TSA	Pani-HCl/MWCNTs (Cauliflower morphology)	Pani-*p*-TSA/MWCNTs (Tubular morphology)
Conductivity (S/cm)	3.32	2.11	3.6	3.95
Solubility at 25 °C (g/L)	4	9	4.5	8
Solubility at 5 °C (g/L)	1	3	0.8	2.1
Electron mobility (cm^2/V.s)	-	-	4.46×10^{-6}	5.48×10^{-4}

© 2025 The Authors. This article is licensed under a Creative Commons Attribution 4.0 International License.

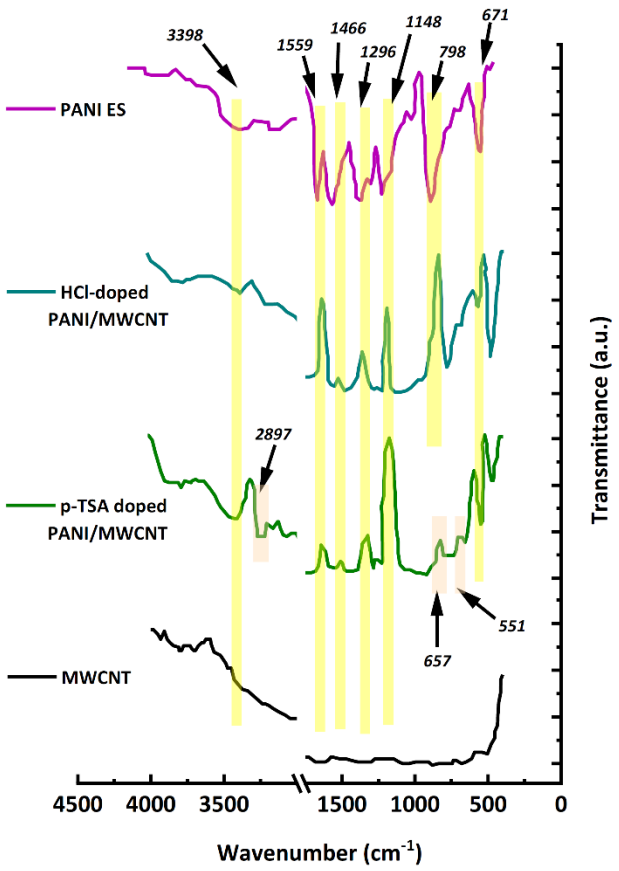

Figure 4. FTIR spectra of emeraldine salt, PAni/MWCNTs doped with HCl, PAni/MWCNTs doped with *p*-TSA, and MWCNTs.

chain's protonation. These peaks represent the non-localized state of electrical charges. As seen in this figure, in this range, the spectrum of doped nanocomposite with *p*-TSA is wider and shifted to fewer frequencies. This is due to the change like the anion produced by *p*-TSA $(SO_3)^-$ relative to HCl (Cl^-), which subsequently results in a change in the C-H plate bending and N-H stretching frequency variation and, as a result, in the different distribution of charge in the quinoid ring. This difference in the charge distribution of the quinoid ring reduces the conductivity of the polyaniline doped with *p*-TSA relative to the HCl-doped polyaniline.

N-H stretching vibrations are observed at 3354 – 3398 cm^{-1}. The intensity of this peak in the HCl-doped PAni/MWCNTs is greater than that of pure polyaniline and is the highest in *p*-TSA-doped PAni/MWCNTs. The sharpening of this peak represents a better transfer of proton from polyaniline to the carbon nanotube network and a better substitution of hydrogen atoms in the amine group. The carbon atom of carbon nanotubes competes with polyaniline nitrogen in absorbing anion. According to the MEP (map of electrostatic potential) of the two dopants (Figure 2), the absorption of $(SO_3)^-$ by the nanotubes is more than Cl^-, resulting in better adhesion of the polyaniline doped with *p*-TSA to the nanotube surface, which represent tubular morphology.

3.1.2. Sonication time

Before polymerization, a mixture of carbon nanotubes and aniline monomers is placed under ultrasonic conditions in aqueous media. The longer sonication time results in better homogenous dispersion of the nanotubes in the mixture of water and aniline, and consequently, the coagulation of MWCNTs is avoided.

3.1.3. Kinetics of the synthesis

In the previous stage, carbon nanotubes were well dispersed between aniline monomers, so many aniline molecules surrounded each nanotube. The rate of addition of the dopant and initiator blended to the

© 2025 The Authors. This article is licensed under a Creative Commons Attribution 4.0 International License.

reactor containing the mixture of carbon nanotubes and aniline monomers played a decisive role in the polymerization stage. The lower the addition rate, the more dopant and initiator molecules could join the aniline monomers on the surface of carbon nanotubes and prevent coagulation of polyaniline chains and phase separation. During this long period, initiator radicals could attack more aniline molecules located on the surface of the carbon nanotubes and begin the heterogeneous nucleation from the surface of the MWCNTs. Therefore, much of the carbon nanotube surface was covered with polyaniline chains, as shown in Figure 5a; thus, tubular morphology became predominant. Conversely, if the droplets were added more quickly, instead of attacking the aniline molecules on the surface of the MWCNTs, initiator radicals intended to attack the scattered available aniline molecules in the synthesis environment. Thus, as in

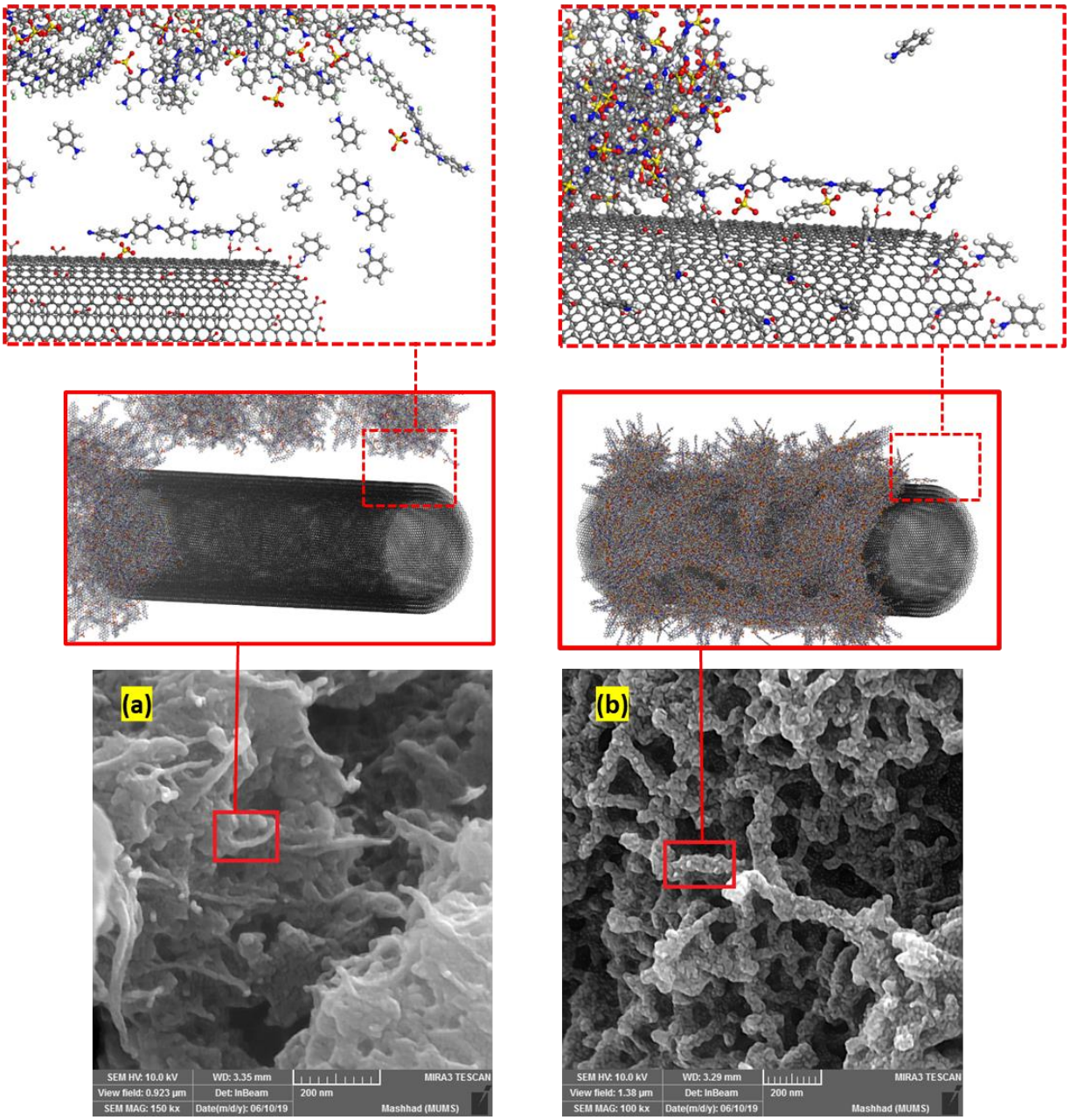

Figure 5. (a) Imperfect and (b) full function of the initiator and dopant in the aniline polymerization on the surface of 10% MWCNTs.

© 2025 The Authors. This article is licensed under a Creative Commons Attribution 4.0 International License.

Figure 5b, polymerization often occurred through homogeneous nucleation, and the cauliflower morphology predominated.

3.1.4. Reaction temperature

Since the polymerization process and free radical formation in the radical oxidation polymerization are considered exothermic reactions, removing heat from the synthesis environment (reducing the temperature of the synthesis environment) contributes to the development of the reaction and its optimal performance. Much research has been done on working out an appropriate temperature for aniline polymerization with high conversion (monomer to polymer) rates and appropriate crystallinity, most of which have reported low temperatures of about 3-5 ° C as the appropriate temperatures. In this study, the process of controlling aniline polymerization on the surface of the MWCNTs was performed at this temperature range, and tubular morphology was obtained.

3.1.5. Impact of morphology on the band gap

The band gap of the nanocomposites with two morphologies and their energy gap versus wavelengths are plotted in Figures 6a and 6b. As mentioned above, optimal dispersion and homogeneity of the nanotubes are achievable in the tubular morphology, and the ratio of the π-π bonds formed is more than the cauliflower morphology system [42]. Therefore, the band gap for transferring electrons from the valence bond to the conduction bond is lower—also, the transmission of wavelengths from blue to red covers a wider range in tubular morphology.

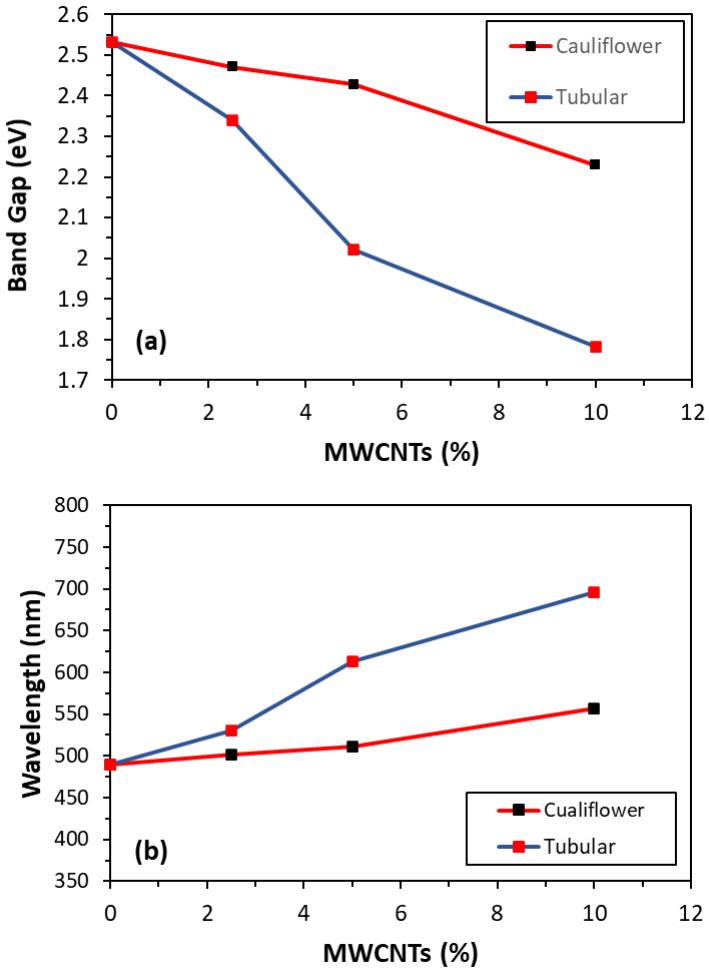

Figure 6. (a) The calculated band gaps and (b) the corresponding wavelengths for nanocomposites with two morphologies (Tubular and Cauliflower).

© 2025 The Authors. This article is licensed under a Creative Commons Attribution 4.0 International License.

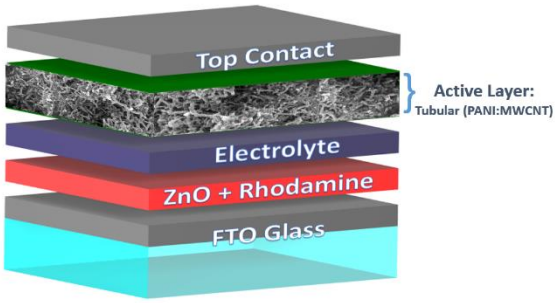

Figure 7. The schematic of the bulk heterojunction polymer solar cell structure with the tubular morphology PAni/MWCNT nanocomposite as the active layer.

3.2. PAni/MWCNT nanocomposite as an active layer of photovoltaic cell

The PAni/MWCNTs films were deposited over the FTO/ZnO glass substrate to prepare the polymer solar cell and used as an active layer. Figure 7 illustrates the scheme of the device structure.

3.2.1. The effect of MWCNT Wt. % on solar cell efficiency

To investigate the dependency of solar cell efficiency on the MWCNTs Wt. %, bulk heterojunction polymer solar cells were fabricated using PAni with a different percent of MWCNT (0%, 2.5%, 5%, and 10%). Figure 8 shows the J-V diagrams for these devices, and the results are abstracted in Table 2. It was observed that by increasing the amount of MWCNTs, the solar cell efficiency enhanced and the solar cells fabricated via the PAni/10 Wt.% MWCNTs as the active layer triggered the best device performance. As mentioned in the previous section, increasing the MWCNT Wt. % reduced the band gap and enhanced conductivity. As a result, the higher the amount of MWCNT, the easier it was to charge transfer, and ultimately, the efficiency of the solar cell increased. This is in agreement with the results obtained for the cauliflower morphology [37].

It is worth noting that by increasing the Wt. percent of MWCNTs, the increasing of efficiency rate gradually decreased, as shown in Figure 9. In addition to increasing the conductivity by adding MWCNTs, the mobility of the charge carriers and recombination was also enhanced. There was always a competition between the charge transfer and the recombination of charge carriers. In low amounts of MWCNTs, the charge transfer rate was higher than their recombination. Because there were enough paths to assist the charges to move away from each other, transferences were in the appropriate direction for collecting charges in the external circuit. When the amount of MWCNTs increased, the recombination rate also enhanced significantly (however, the separation rate was still higher than the recombination rate).

On the other hand, according to the results shown in Table 2, it can be seen that despite enhancing efficiency, increasing the amount of MWCNT led to a reduction of FF. One of the factors that greatly affected the FF was the recombination [43]. However, the addition of MWCNT had a greater impact on J_{SC} due to the creation of high percolation paths, and despite the reduction in FF, device performance was generally increased.

3.2.2. The dependency of solar cell efficiency on the morphology of the active layer

Table 3 presents the photovoltaic parameters of solar cells with the PAni/10% MWCNT nanocomposite as an active layer with tunable morphologies (cauliflower and tubular). The J_{sc} and V_{oc} of the cell with tubular morphology are increased significantly regarding a

Table 2. Photovoltaic properties of the PSCs based on PAni/MWCNTs tubular morphology with different weight percent of MWCNTs

MWCNTs Wt.%	V_{oc} (V)	J_{sc} (mA/cm^2)	FF (%)	η (%)
0	0.0477	0.0101	0.024	0.000063
2.5	0.2497	0.0579	35	1.05
5	0.6575	0.1249	17	2.25
10	1.7329	0.0959	20.1	3.01

© 2025 The Authors. This article is licensed under a Creative Commons Attribution 4.0 International License.

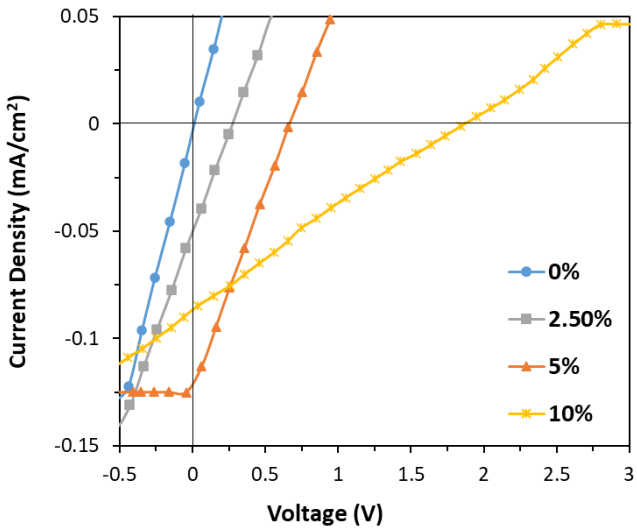

Figure 8. J-V diagrams of synthesized tubular nanocomposites with different weight percent of MWCNTs under the illumination of AM 1.5G, 100 mW/cm².

Table 3. Comparison between photovoltaic properties of PAni/10 Wt.% MWCNT nanocomposites with two morphologies

PSCs	V_{oc} (V)	J_{sc} (mA/cm²)	FF (%)	η (%)
Tubular morphology	1.7329	0.09592	20.1	3.01
Cauliflower morphology	0.5394	0.00111	0.34	1.04

device based on cauliflower morphology. Changing the active layer morphology from cauliflower to tubular form resulted in three times higher efficiency. The ratio of charge carrier recombination to separation depends strongly on the morphological tuning [44-47]. The recombination rate should reduce and the separation rate should increase to improve efficiency. Based on the experimental results obtained here, PAni/MWCNTs nanocomposites with the tubular morphology exhibited better photovoltaic behavior than nanocomposites with the cauliflower morphology. The reason for this behavior is the with the homogeneity of the components in tubular morphology, the photo-response of the nanocomposite improved. With the band gap reduction, the ability to charge transportation increased. In addition, enhancing FF leads to improved efficiency of

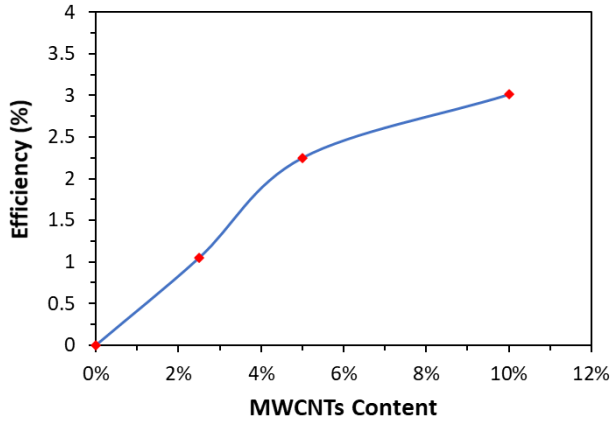

Figure 9. Efficiency versus MWCNTs weight percent behavior of PSCs based on PAni/MWCNTs with tubular morphology.

© 2025 The Authors. This article is licensed under a Creative Commons Attribution 4.0 International License.

devices (about seventy times higher FF in Table 3 for tubular morphology). Besides, charge transfer in a crystalline structure is faster than in a structure with amorphous networks. The formed tubes with MWCNT core act as conductive bridges for electron transfer, and once the light is emitted at a special wavelength, the charges transfer more easily. Furthermore, as shown in Figure 5a, in tubular morphology, most of the nanotube surface is covered by polyaniline chains. This increases the interface area between the polymer matrix and the carbon nanotube, which acts as a tunnel for electron transfer so that the separation and transfer of charges can be promoted and the recombination rate can be diminished [48].

4. Conclusions

This study focused on synthesizing PAni/MWCNT nanocomposites with tunable morphologies and evaluating their application in polymer solar cells. The findings highlighted that tubular morphology outperformed cauliflower morphology in terms of conductivity, electron mobility, and band gap due to the efficient charge transfer pathways provided by tubular structures. Morphology control led to significant improvements in photovoltaic performance, including higher V_{OC}, J_{SC}, and FF, resulting in threefold higher efficiency. These enhancements were attributed to the better alignment and uniformity of MWCNTs, forming an effective percolation network. This work underscores the potential of morphology tuning in advancing organic solar cell performance and paves the way for further research and eventual commercialization of these devices.

Conflict of Interest

The author declares no conflict of interest.

References

1. 1. I. Burgués-Ceballos, et al. Towards industrialization of polymer solar cells: material processing for upscaling. *Journal of Materials Chemistry A*, **2014**, *2*, 17711.

2. R.A. Janssen and J. Nelson. Factors limiting device efficiency in organic photovoltaics. *Advanced Materials*, **2013**, *25*, 1847.

3. M. Glatthaar, et al. Efficiency limiting factors of organic bulk heterojunction solar cells identified by electrical impedance spectroscopy. *Solar energy materials and solar cells*, **2007**, *91*, 390.

4. Y. Li, et al. Flexible and semitransparent organic solar cells. *Advanced Energy Materials*, **2018**, *8*, 1701791.

5. S. Liu, et al. Enhanced efficiency of polymer solar cells by adding a high-mobility conjugated polymer. *Energy & Environmental Science*, **2015**, *8*, 1463.

6. S.R. Cowan, et al. Charge formation, recombination, and sweep-out dynamics in organic solar cells. *Advanced Functional Materials*, **2012**, *22*, 1116.

7. C. Groves. Developing understanding of organic photovoltaic devices: kinetic Monte Carlo models of geminate and non-geminate recombination, charge transport and charge extraction. *Energy & Environmental Science*, **2013**, *6*, 3202.

8. A. Baumann, et al. A new approach for probing the mobility and lifetime of photogenerated charge carriers in organic solar cells under real operating conditions. *Advanced materials*, **2012**, *24*, 4381.

9. K. Zhu, et al. Enhanced charge-collection efficiencies and light scattering in dye-sensitized solar cells using oriented TiO2 nanotubes arrays. *Nano letters*, **2007**, *7*, 69.

10. H. Lin, et al. Conducting polymer composite film incorporated with aligned carbon nanotubes for transparent, flexible and efficient supercapacitor. *Scientific reports*, **2013**, *3*, 1353.

11. K.-M. Lee, et al. Incorporating carbon nanotube in a low-temperature fabrication process for dye-sensitized TiO2 solar cells. *Solar Energy Materials and Solar Cells*, **2008**, *92*, 1628.

12. J. Arranz-Andrés and W.J. Blau. Enhanced device performance using different carbon nanotube types in polymer photovoltaic devices. *Carbon*, **2008**, *46*, 2067.

13. G. Keru, P.G. Ndungu, and V.O. Nyamori. A review on carbon nanotube/polymer composites for organic solar cells. *International Journal of Energy Research*, **2014**, *38*, 1635.

14. I. Jeon, et al. Single-Walled Carbon Nanotubes in Emerging Solar Cells: Synthesis and Electrode Applications. *Advanced Energy Materials*, **2019**, *9*, 1801312.

15. H.A. Alturaif, et al. Use of carbon nanotubes (CNTs) with polymers in solar cells. *Molecules*, **2014**, *19*, 17329.

16. S. Berson, et al. Elaboration of P3HT/CNT/PCBM composites for organic photovoltaic cells. *Advanced Functional Materials*, **2007**, *17*, 3363.

17. X.-L. Xie, Y.-W. Mai, and X.-P. Zhou. Dispersion and alignment of carbon nanotubes in polymer matrix: a review. *Materials science and engineering: R: Reports*, **2005**, *49*, 89.

© 2025 The Authors. This article is licensed under a Creative Commons Attribution 4.0 International License.

18. Z. Jia, et al. Study on poly (methyl methacrylate)/carbon nanotube composites. *Materials Science and Engineering: A*, **1999**, *271*, 395.

19. F.C. Krebs. Fabrication and processing of polymer solar cells: A review of printing and coating techniques. *Solar energy materials and solar cells*, **2009**, *93*, 394.

20. A.C. Mayer, et al. Polymer-based solar cells. *Materials today*, **2007**, *10*, 28.

21. G. Li, R. Zhu, and Y. Yang. Polymer solar cells. *Nature photonics*, **2012**, *6*, 153.

22. M. Jørgensen, K. Norrman, and F.C. Krebs. Stability/degradation of polymer solar cells. *Solar energy materials and solar cells*, **2008**, *92*, 686.

23. H.-Y. Chen, et al. Polymer solar cells with enhanced open-circuit voltage and efficiency. *Nature photonics*, **2009**, *3*, 649.

24. S. Palaniappan and A. John. Polyaniline materials by emulsion polymerization pathway. *Progress in Polymer Science*, **2008**, *33*, 732.

25. C. Oueiny, S. Berlioz, and F.-X. Perrin. Carbon nanotube–polyaniline composites. *Progress in Polymer Science*, **2014**, *39*, 707.

26. S. Bhadra, et al. Progress in preparation, processing and applications of polyaniline. *Progress in polymer science*, **2009**, *34*, 783.

27. Y. Sun, S.R. Wilson, and D.I. Schuster. High dissolution and strong light emission of carbon nanotubes in aromatic amine solvents. *Journal of the American Chemical Society*, **2001**, *123*, 5348.

28. T.-M. Wu and Y.-W. Lin. Doped polyaniline/multi-walled carbon nanotube composites: Preparation, characterization and properties. *Polymer*, **2006**, *47*, 3576.

29. D.K. Kim, K. Wha Oh, and S.H. Kim. Synthesis of polyaniline/multiwall carbon nanotube composite via inverse emulsion polymerization. *Journal of Polymer Science Part B: Polymer Physics*, **2008**, *46*, 2255.

30. P. Jiménez, et al. Carbon nanotube effect on polyaniline morphology in water dispersible composites. *The Journal of Physical Chemistry B*, **2010**, *114*, 1579.

31. W. Ma, et al. Thermally stable, efficient polymer solar cells with nanoscale control of the interpenetrating network morphology. *Advanced Functional Materials*, **2005**, *15*, 1617.

32. Y. Huang, et al. Bulk heterojunction solar cells: morphology and performance relationships. *Chemical reviews*, **2014**, *114*, 7006.

33. S.N.K. Abad, et al. Growth mechanism and charge transport properties of hybrid Au/ZnO nanoprisms. *Journal of Alloys and Compounds*, **2019**, *777*, 1386.

34. F. Zhao, C. Wang, and X. Zhan. Morphology control in organic solar cells. *Advanced Energy Materials*, **2018**, *8*, 1703147.

35. B.C. Thompson and J.M. Fréchet. Polymer–fullerene composite solar cells. *Angewandte chemie international edition*, **2008**, *47*, 58.

36. Y. Liao, et al. Carbon nanotube/polyaniline composite nanofibers: facile synthesis and chemosensors. *Nano letters*, **2011**, *11*, 954.

37. R. Charekhah, et al. Bulk heterojunction solar cells based on polyaniline/multi wall carbon nanotube: from morphology control to cell efficiency. *Journal of Materials Science: Materials in Electronics*, **2019**, *30*, 26.

38. M. Campos and B. Bello Jr. Mechanism of conduction in doped polyaniline. *Journal of Physics D: Applied Physics*, **1997**, *30*, 1531.

39. S. Sinha, S. Bhadra, and D. Khastgir. Effect of dopant type on the properties of polyaniline. *Journal of Applied Polymer Science*, **2009**, *112*, 3135.

40. A. Imani and G. Farzi. VRH investigation of polyaniline–multiwalled carbon nanotube nanocomposite network. *Bulletin of Materials Science*, **2015**, *38*, 831.

41. A. Imani and G. Farzi. Low temperature process of electronic charge transport mechanism in PANi/MWCNT nanocomposites: tubular morphology. *Journal of Materials Science: Materials in Electronics*, **2017**, *28*, 10684.

42. S. Kondawar, M. Deshpande, and S. Agrawal. Transport properties of conductive polyaniline nanocomposites based on carbon nanotubes. *International Journal of Composite Materials*, **2012**, *2*, 32.

43. D. Bartesaghi, et al. Competition between recombination and extraction of free charges determines the fill factor of organic solar cells. *Nature communications*, **2015**, *6*, 7083.

44. D. Veldman, et al. Compositional and electric field dependence of the dissociation of charge transfer excitons in alternating polyfluorene copolymer/fullerene blends. *Journal of the American Chemical Society*, **2008**, *130*, 7721.

45. I.-W. Hwang, D. Moses, and A.J. Heeger. Photoinduced carrier generation in P3HT/PCBM bulk heterojunction materials. *The Journal of Physical Chemistry C*, **2008**, *112*, 4350.

46. T.M. Clarke, et al. Free energy control of charge photogeneration in polythiophene/fullerene solar cells: the influence of thermal annealing on P3HT/PCBM blends. *Advanced Functional Materials*, **2008**, *18*, 4029.

47. A. Gusain, R.M. Faria, and P.B. Miranda. Polymer Solar Cells—Interfacial Processes Related to Performance Issues. *Frontiers in chemistry*, **2019**, *7*, 61.

48. P. Peumans and S.R. Forrest. Separation of geminate charge-pairs at donor–acceptor interfaces in disordered solids. *Chemical Physics Letters*, **2004**, *398*, 27.

© 2025 The Authors. This article is licensed under a Creative Commons Attribution 4.0 International License.

An Overview of Silane-based Hybrid Sol-gel Coatings for Highly Efficient Metal Corrosion Protection

Milad Sheydaei [a,*], Milad Edraki [b]

[a] *Department of Chemical Engineering, Faculty of Engineering, University of Garmsar, Garmsar, Iran*

[b] *Department of Chemical and Polymer Engineering, South Tehran Branch, Islamic Azad University, Tehran, P.O. Box 19585-466 Iran*

Editor's note: This invited mini-review presents an overview of the corrosion protection potential of hybrid silane-based coatings applied through sol-gel fabrication on different metal substances. Sheydaei and Edraki focused on the environmental impact of such coatings and the importance of corrosion inhibitors on the final performance of silane-based corrosion protection systems for different application fields.

doi: 10.22034/jams.2024.210131

How to cite: M. Sheydaei and M. Edraki. *Journal of Applied Material Science*, **2025**, *1*, 210131.

© 2025 *J. Appl. Mat. Sci.* This material is licensed under a Creative Commons Attribution 4.0 International License.

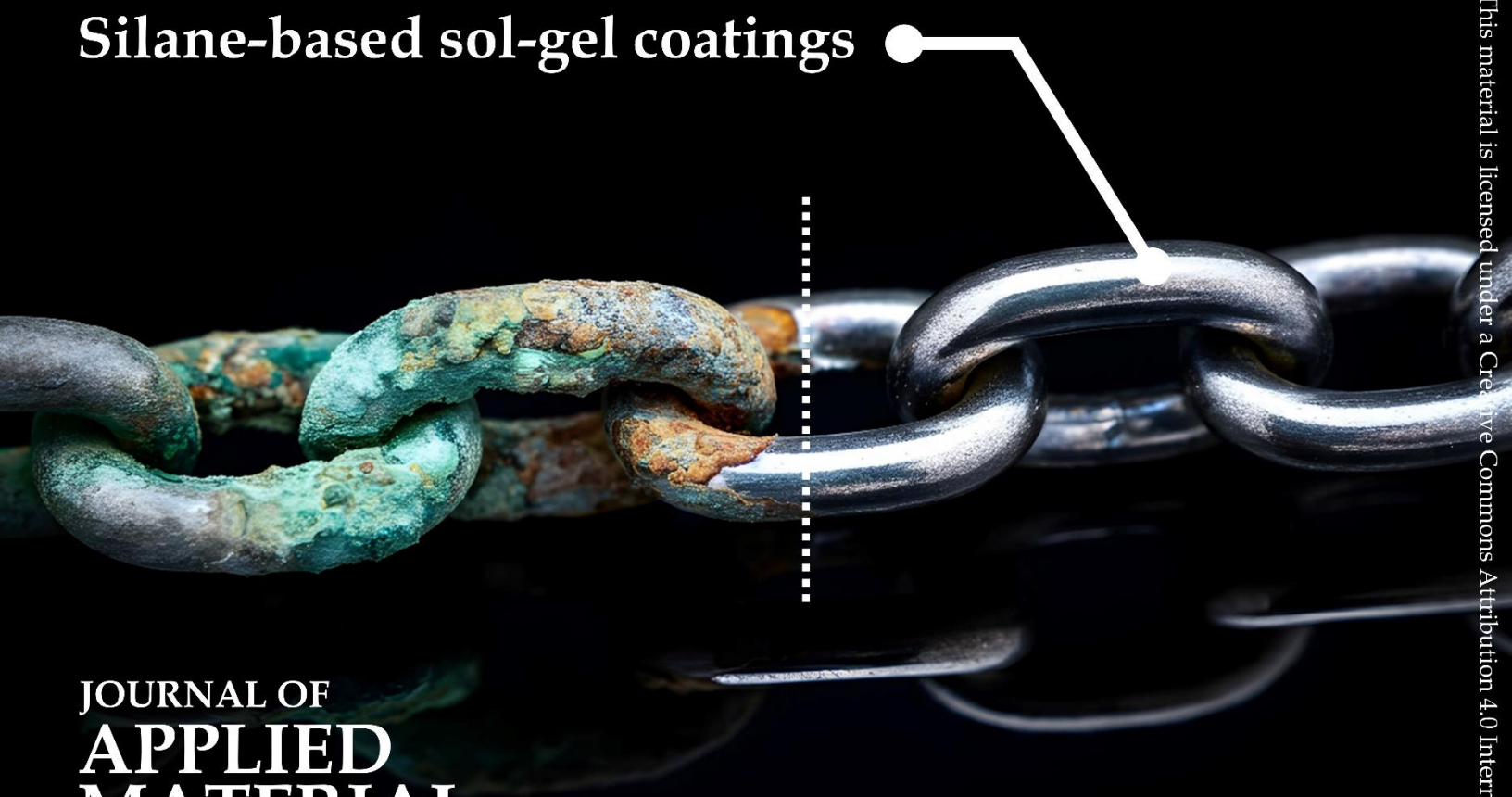

JOURNAL OF
APPLIED
MATERIAL
SCIENCE
www.jams.hsu.ac.ir

Journal of Applied Material Science **2025**, *1*, 210131
How to cite: M. Sheydaei and M. Edraki, *Journal of Applied Material Science*, **2025**, *1*, 210131.
Journal homepage: **www.jams.hsu.ac.ir**

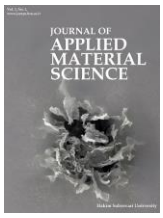

Invited Review

An Overview of Silane-based Hybrid Sol-gel Coatings for Highly Efficient Metal Corrosion Protection

Milad Sheydaei [a,*], Milad Edraki [b]

[a] *Department of Chemical Engineering, Faculty of Engineering, University of Garmsar, Garmsar, Iran*

[b] *Department of Chemical and Polymer Engineering, South Tehran Branch, Islamic Azad University, Tehran, P.O. Box 19585-466 Iran*

Abstract

The most important problem of metal structures is corrosion, which can lead to significant losses and is considered a serious threat to safety. Corrosion can be considered a slow but continuous phenomenon. Researchers are continually seeking low-cost, high-performance solutions. In the meantime, coatings have traditionally been the most popular method to mitigate corrosion. However, there is a growing focus on developing environmentally friendly protective coatings, as many conventional coatings can harm the environment after they deteriorate. Many coatings incorporate corrosion inhibitors, providing a synergistic effect that helps prevent corrosion. Unfortunately, many of these inhibitors contain toxic and harmful substances posing additional environmental risks. Therefore, selecting the right coating is crucial. Among the various types of coatings, silane-based sol-gel coatings emerge as suitable candidates. This paper, discusses silane-based sol-gel coatings, the sol-gel method, and the factors that influence the efficiency of, these products. Additionally, it explores the use of plant-extracted inhibitors in sol-gel coatings.

Keywords: Environmental pollution, Green chemistry, Green inhibitors.

Contents

1. Introduction 1
2. Background 3
3. Using sol-gel coatings to prevent corrosion in metals 5
4. Conclusions 8

* Corresponding author.
Email address: md.sheydaei@fmgarmsar.ac.ir (M. Sheydaei)

Received 13 October 2024
Revised 13 November 2024
Accepted 21 November 2024
Available online 25 November 2024

https://doi.org/10.22034/jams.2024.210131
© 2025 The Authors. This article is licensed under a Creative Commons Attribution 4.0 International License.

1. Introduction

Metal structures, despite their unique properties, have a big problem, which is a vulnerability in corrosive environments [1]. Corrosion can be considered a mysterious and quiet phenomenon, but it is very damaging because it can cause huge costs [2]. Although corrosion occurs in very aggressive environments such as the sea, it appears and spreads very quickly [3]. Corrosion has been a concern of researchers and manufacturers of metal instruments for many years, and many methods have been investigated to delay and slow corrosion. Corrosion, in addition to creating financial costs, also causes environmental pollution [4]. Researchers have found that one factor in the release of heavy metals into the environment is corrosion [5]. Many industries such as oil and gas and marine are constantly involved in the phenomenon of corrosion and suffer economic damages [6,7]. Corrosion can be considered an electrochemical and spontaneous process, although many factors contribute to its creation and development, such as temperature, humidity, pH, and chemicals [8]. In the industry, manufacturers are always looking for low-cost and high-performance solutions, although the new legislations require the use of methods and chemicals that are safe for the environment and humans [9]. Figure 1 shows the various methods used to prevent corrosion.

Corrosion inhibitors are very effective, but many of them are toxic, such as chromates, and their release into the environment can cause serious harm [10,11]. Therefore, researchers are investigating green corrosion inhibitors (such as plant extracts, pharmaceuticals, and natural gums) [12]. It can be said that coatings have the best effect in corrosion protection [13]. They are an outer layer that prevents the penetration of corrosive species [14]. Among the classifications of coatings, polymers are in a special place due to properties such as hydrophobicity and self-healing [15].

Among the coating production methods, the sol-gel method has received much attention in the past years,

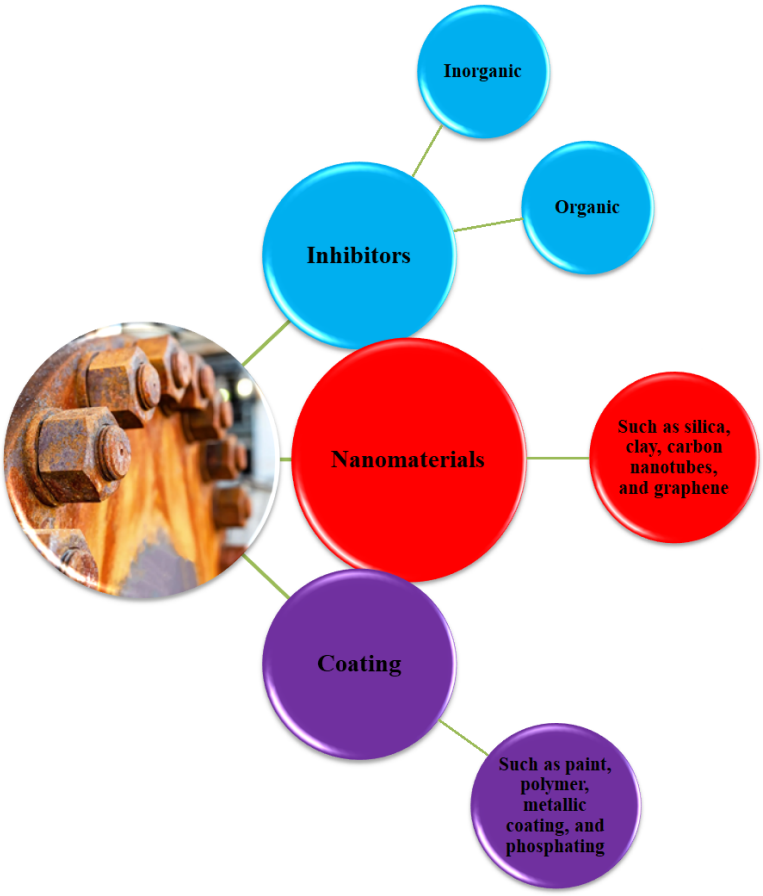

Figure 1. Different methods to prevent corrosion

© 2025 The Authors. This article is licensed under a Creative Commons Attribution 4.0 International License.

especially the silane-based hybrid coatings that are prepared by the sol-gel method [16]. The sol-gel method is very economical, low toxicity, and produces a high-purity product [17]. Considering the environmental concerns caused by chromate-containing coatings, silane-based hybrid coatings can be considered a suitable alternative for them. Hybrid organic-inorganic materials synthesized by sol-gel method have been widely used since the last decade. It can be said that the sol-gel method consists of three stages of hydrolysis, polycondensation, and thermal densification and can be applied at ambient temperature and atmospheric pressure [18]. In this review, research on the use of silane coatings to reduce the corrosion of metal substrates has been investigated.

2. Background

The history of using coatings resistant to environmental factors goes back thousands of years [19]. The Egyptians developed wax-based weatherproof coatings that were applied in the molten state [20]. Natural bitumen was also used as a coating to protect the wooden body of ships [21]. Coatings are prepared to create a barrier and separate the object from the environment. There is no such thing as perfect (lifelong) coating, and no coating can provide complete protection [22]. In general, as the effective life and efficiency of the coating system increases, the costs of its implementation also increase. With the expansion of various types of surface coatings, organic-inorganic hybrid coatings that were prepared by the sol-gel process have received much attention (see Figure 2).

These coatings provide the possibility of achieving special properties by having organic and inorganic materials together. Hybrid organic-inorganic coatings that have inorganic particles on a nanoscale are proposed as nanocomposite coatings. Composites are the result of the physical mixing of two or more materials, in which two main phases are called the matrix phase and the dispersed phase. Usually, the purpose of preparing a composite is to create properties that the constituent phases alone do not have. Organic-inorganic hybrid nanocomposites prepared by the sol-gel method have uniform morphology and good

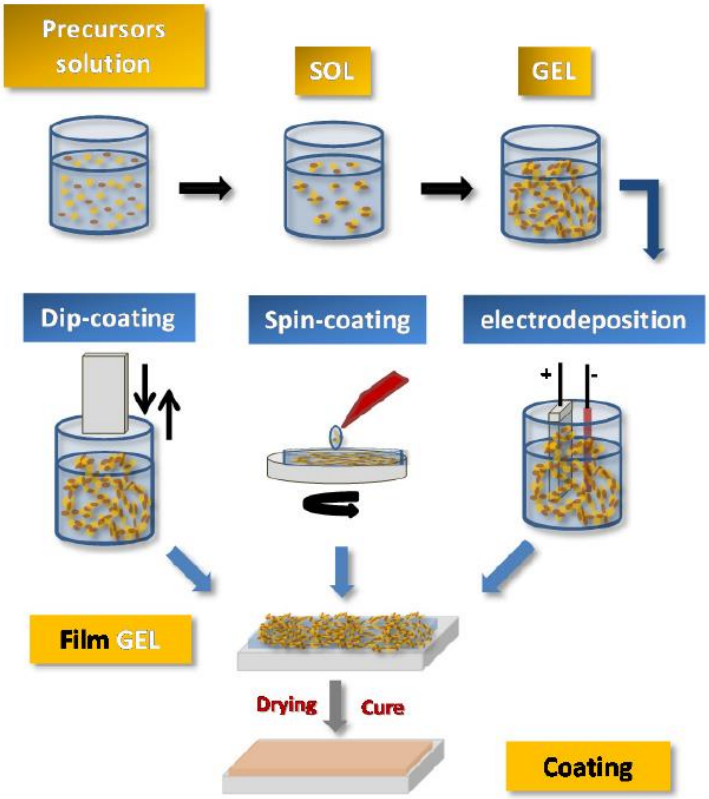

Figure 2. Example of processing routes to obtain sol-gel coatings for a surface. Reprinted with permission from [23]. 2016, MDPI.

© 2025 The Authors. This article is licensed under a Creative Commons Attribution 4.0 International License.

properties and can be used in many applications such as anti-wear, anti-scratch, anti-corrosion, anti-fungal and bacterial coatings and even in the field of pharmaceuticals [24,25]. A group of sol-gel coatings is based on silanes, which, contrary to their high corrosion protection potential, are electrochemically inactive unless they have chemically active groups [26]. Therefore, these coatings do not provide active protection. The protection they provide is generally based on passive protection through the formation of a layer that adheres well to the surface. However, long-term exposure of these coatings to water/electrolyte eventually causes moisture to penetrate the metal/coating interface [27]. The protective properties of sol-gel coatings can be improved by using active species such as corrosion inhibitors that add an active protective mechanism to the coating (see Figure 3) [28]. Corrosion inhibitors can be added directly to the formulation or immobilized in places to reduce possible interactions with the matrix and control the release of the inhibitor [6-8].

A sol is a colloidal dispersion of nano-solid particles in a liquid medium, and a gel is defined as a colloidal system that is more like a solid than a sol [29]. Sol-gel chemistry is related to the process in which a gel is formed by the accumulation of sol [16]. As a result of hydrolysis reactions with the help of an acid or base catalyst, a sol is formed, and condensation reactions lead to the gelation of this sol [16,29]. In fact, as a result of condensation reactions, molecules with high molecular weight are produced, which are continuously joined together [30].

The effective factors in the sol-gel process are the molar ratio of reactants, solvent, temperature, and pH [16,17,29]. Some of the advantages of the sol-gel method include low process temperature (close to ambient temperature), ease of operation, high chemical diversity, the possibility of coating different geometric shapes, the strong interaction of the coating with the surface, simple process, low price, and chemical and physical stability [16,30,31]. Also, in the sol-gel process, it is possible to add special properties to the coating by adding additives, based on which sol coatings with properties such as UV resistance and anti-reflection are prepared [16,17,30]. Despite the mentioned advantages, this method also has disadvantages, such as that some raw materials used in this method are sensitive to environmental factors such as humidity [32]. Also, the possibility of the solvent remaining in the coating and creating cracks in the coating [16,32].

In the past years, special attention has been paid to the production of organic-inorganic hybrid coatings using the sol-gel method, which showed good corrosion protection properties [33]. For several reasons, organic-inorganic hybrid coatings synthesized by the sol-gel method are used more than pure organic or inorganic sol-gel coatings to protect the corrosion of metal surfaces, which are mentioned below [16,17,33]. The hybrid coating leads to the formation of a film without cracks better than organic or pure inorganic coatings, and for heat treatment, they usually require lower temperatures (usually 100 °C) than the pure organic or inorganic sol-gel coatings (600-800 °C) [34,35]. On the other hand, there is a possibility of compatibility with various added anti-corrosion agents such as inhibitors and pigments for organic-inorganic hybrid coatings [34].

Hybrid coatings are divided into two groups based on the interaction between organic and inorganic implementation [16,17]. The first group is coatings in which there is no chemical bond between organic and inorganic components and these components are only together by weak van der Waals or hydrogen interactions [34,35]. The hybrid coating in this group is formed by mixing organic and inorganic phases in the presence of a contacting organic polymer [35]. Therefore, these composites show little stability against moisture. In the second group, there are strong covalent bonds between organic and inorganic [34]. Regarding the

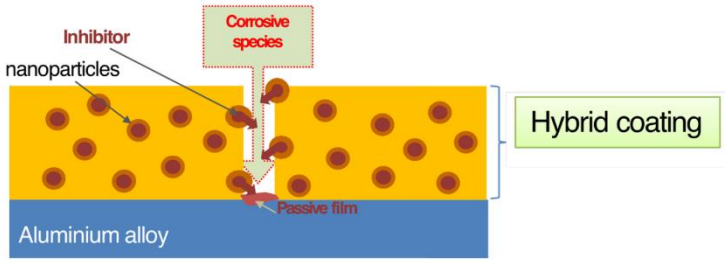

Figure 3. Generic scheme of the corrosion healing mechanism of a ca hybrid sol-gel coating containing inhibitory nanoparticles. Reprinted with permission from [23]. 2016, MDPI.

© 2025 The Authors. This article is licensed under a Creative Commons Attribution 4.0 International License.

second group, we can mention organo alkoxysilane [16,17,35]. One of the advantages of these coatings is increasing the adhesion of the final coating to the metal surface and other coatings, increasing the mechanical resistance of the coating, and producing a crack-free and completely uniform coating [36]. In summary, it can be said that in the sol-gel process, the hydrolysis reaction is performed by increasing the water content and replacing the alkoxy groups (OR) with OH groups (see Figure 4 (a and b)). Next, successive condensation reactions between Si-OH and Si-OR groups occur, and Si-O-Si is produced with alcohol as well as water as by-products (see Figure 4c). In this section, the sol-gel process was briefly reviewed, and the studies conducted are discussed in the next section.

3. Using sol-gel coatings to prevent corrosion in metals

Corrosion prevention has always been a concern and various methods based on electrochemical principles have been explored for this task, although methods of separating metal from aggressive media have been a field of study and investigation in materials science for many years [23]. Corrosion and subsequent rate of reaction depend on two physical and chemical factors of the substrate, and also, the type of corrosion (such as pitting, filiform, and bimetallic) depends on the substrate and the aggressive media. Meanwhile, aggressive species such as chloride ions play an important role in determining the type of corrosion and its reaction rate [37]. One of the popular and developing methods of surface coating is the sol-gel method [38]. The most common sol-gel coating matrices are based on silane, some of their precursors are reported in Table 1.

Coatings based on silanes such as TEOS are very popular because they have high thermal stability and their reactivity is possible in a wide range of temperatures [38,39]. Also, this class of precursors provides good wear resistance, adhesion, and corrosion protection [39]. Rodríguez-Alonso et al. [40] investigated corrosion protection of AZ61 magnesium alloys by using sol-gel method (the precursors were TEOS and 3-

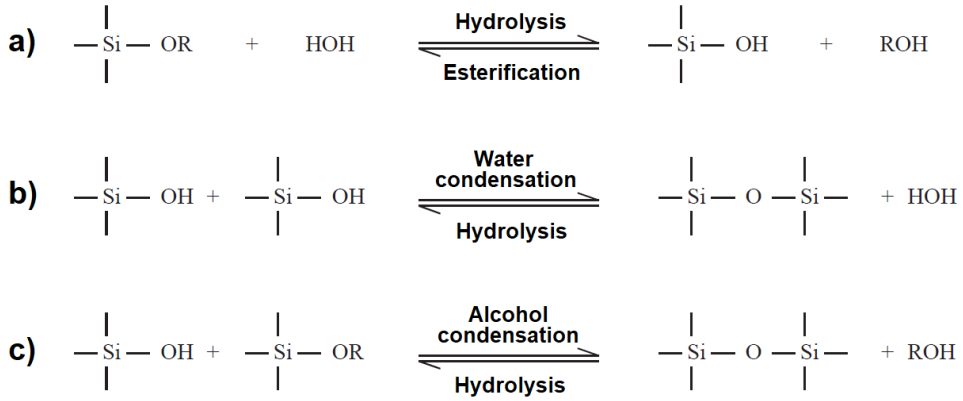

Figure 4. Hydrolysis and condensation reactions in sol-gel processes. Reprinted with permission from [37]. 2005, IPPI.

Table 1. Full names and abbreviations of some precursors of silane (data from [37,39])

Chemical Name	Abbreviation
Tetraethoxysilane	TEOS
3-Glycidoxypropyltrimethoxysilane	GPTMS
Methyltriethoxysilane	MTES
Glycidoxy propyl trimethoxy silane	GPS
Polymethyltrimethoxysilane	PMTMS
3-Aminopropyltrimethoxysilane	APS
Bis [3-(triethoxysilyl)propyl]tetrasulfide	BTESPT
Methylmethoxysilane	MTMS
3-Glycidoxypropyltrimethoxysilane	GPTMS
Methyltriethoxysilane	MTES

© 2025 The Authors. This article is licensed under a Creative Commons Attribution 4.0 International License.

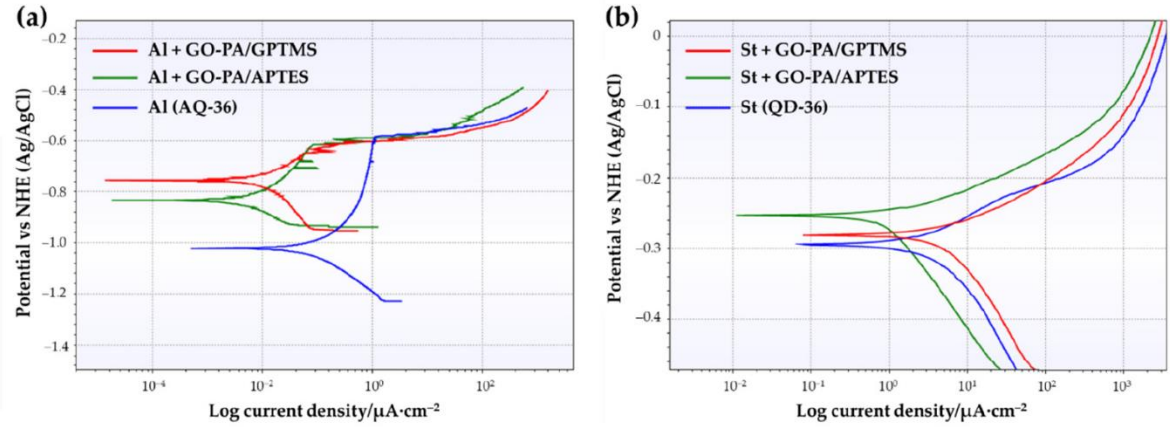

Figure 5. Polarization curves of aluminum (a) and steel (b). Reprinted with permission from [41]. 2022, MDPI.

(Trimethoxysilyl)propyl methacrylate) and inhibitors such as L-cysteine, dimethyl glyoxime, quinine, 2-Aminopyridine, graphene oxide sheet; and titanium dioxide nanoparticles. The results showed that these coatings have good adhesion and performance even without any pretreatment. The results showed that these coatings have good adhesion and performance even without any pretreatment. All inhibitors improved corrosion resistance except graphene. Sfameni et al. [41] prepared a coating using graphene oxide (GO) and phytic acid (PA), as well as GPTMS and APTES precursors. The performance of coatings on aluminum and steel layers was investigated. The results of the polarization (see Figure 5) and neutral salt spray test (see Figure 6) showed improved anti-corrosion performance.

Li et al. [42] created a coating on Q235 carbon steel substrate using MTMS, colloidal silicon dioxide nanoparticles, silica, and titania powders by sol-gel method. Electrochemical impedance spectroscopy results showed that this coating shows excellent anti-corrosion properties. Also, the authors clearly showed the process of the sol-gel process using Transmission Electron Microscopy (TEM) images (see Figure 7).

Inorganic thin films prepared using the sol-gel method are used in various fields. These layers contribute to low conductivity and high purity for excellent sensitivity. Finally, materials with high surface area and porosity increase the sensitivity in mechanisms dominated by surface phenomena [43].

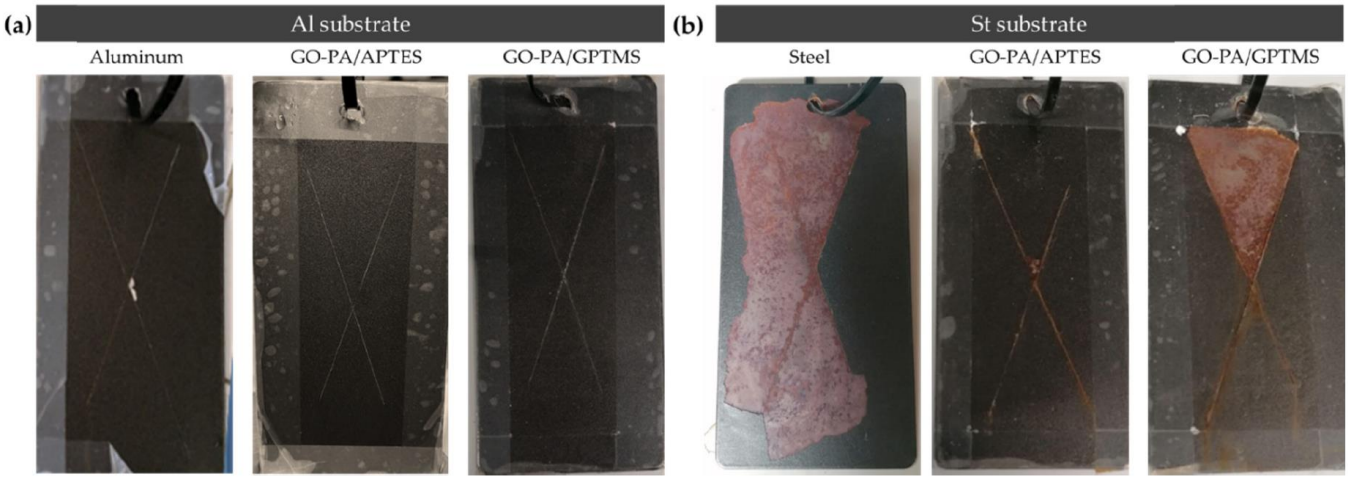

Figure 6. Visual images of coated substrates without and with nanofiller after salt spray test (aluminum: 900 h; coated aluminum 1300 h; steel: 50 h; coated steel: 400 h). Reprinted with permission from [41]. 2022, MDPI.

© 2025 The Authors. This article is licensed under a Creative Commons Attribution 4.0 International License.

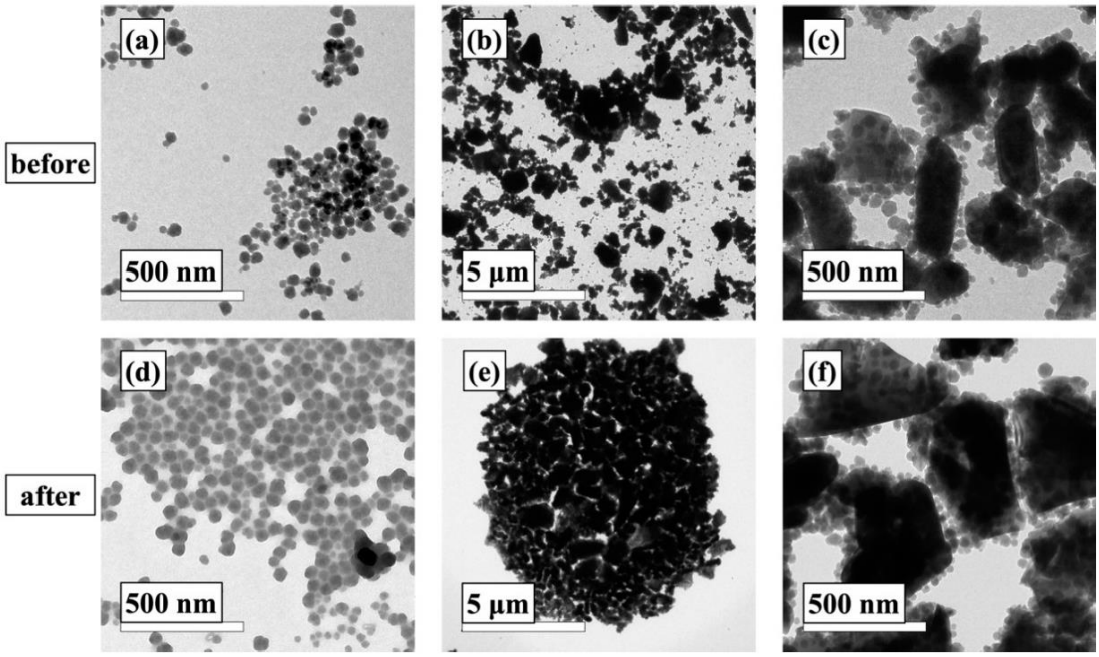

Figure 7. TEM images of colloidal silica nanoparticles (a,d) and silica nanoparticles/filler mixture before (b,c) and after (e,f) the sol-gel process. Reprinted with permission from [42]. 2019, MDPI.

Table 2. Performance results of some coatings in different corrosion environments

Coatings	Sol-Gel Solution Composition	Substrate	Corrosive medium	Effect	Ref.
Bare sol-gel coating	Mixing TEOS and GPTMS	AZ31	Sodium chloride (NaCl) (0.1 M)	The hybrid coatings reduced the corrosion current density by about three orders and the protection range increased up to 160 mV.	44
Sol-gel coating + corrosion inhibitor	Mixing MTES, GPTMS, and TEOS	AZ31	Simulated Body Fluid (SBF) solution	The Rf of silane coating modified with hydroxyapatite nanoparticles was more than 100 times higher than that without modification after being soaked for 4 days.	45
Composite sol-gel coating (PEO/sol-gel)	Mixing TEOS and MTES.	AZ31	Hanks' solution (pH = 7)	icorr PEO = 1.6×10^{-7} A/cm^2 icorr PEO/sol-gel = 2.50×10^{-8} A/cm^2	46
Composite sol-gel coating (PEO/sol-gel)	Mixing GPS and TEOS	AM6	NaCl (3.5 wt.%)	Rp PEO = 3.37×10^5 W cm^2 Rp PEO/sol-gel = 3.58×10^9 W cm^2	47
Composite sol-gel coating (N-GQDs/sol-gel)	PMTMS: (MTMS: ethanol: DI water = 3: 10: 20)	AZ91D	NaCl (3.5 wt.%)	Rct N-GQDs /sol-gel = 1.7×10^4 W cm^2	48
Composite sol-gel coating (sol-gel/GO/sol-gel)	Mixing APS/BTESPT	AZ31B	NaCl (3.5 wt.%)	icorr sol-gel/GO/sol-gel = 1.381×10^{-8} A/cm^2	49
Composite sol-gel coating (MAO/sol-gel)	PMTMS: (MTMS: ethanol: DI water = 3:10: 20)	AZ31	NaCl (3.5 wt.%)	icorr MAO/sol-gel = 2.86×10^{-8} A/cm^2 Rct MAO/sol-gel = 2.24×10^6 W cm^2	50
Composite sol-gel coating (CLP/sol-gel)	Mixing TEOS and MTES	AZ91	NaCl (3.5 wt.%)	Rtotal conversion coating = 0.681 kW cm^2 Rtotal conversion coating /sol-gel = 127.382 kW cm^2	51

Notes: Rf: the overall resistance of the coating response, icorr: Corrosion current density, Rp: Polarization resistance, Rct: The charge transfer resistance, Rtotal: values are calculated as the sum of all the faradaic resistance by using the fitted data, PEO: Plasma electrolytic oxidation, CLP: Clinoptilolite, MAO: Micro-arc oxidation, GQD: Graphene quantum dots.

© 2025 The Authors. This article is licensed under a Creative Commons Attribution 4.0 International License.

In fact, the complexing and dispersing agents determine the size, shape, and porosity of the particles [23,43]. Also, the porous aerogels materials increase the conductivity and maintain the amorphous morphology [43]. One of the applications of sol-gel materials (such as olivine-type materials, nickel-based materials, manganese-based materials, carbon aerogels, and perovskites) is to produce supercapacitors [23,43]. The sol-gel process can be considered a flexible method to produce coatings because a denser layer with high adhesion can be created with this process, in this regard studies in this field are widely underway, and some of the results of these studies in Table 2 are reported.

Although sol-gel is considered a green method, some of the additives used in this method, especially corrosion inhibitors, are very toxic and harmful to health and the environment [8]. Hence, in the past years, researchers have investigated the use of green corrosion inhibitors (GCIs) in this method. Among the classifications of GCIs, plants and their extracts are of great interest [6,8]. Because plants are rich in bioactive compounds, many of them have antimicrobial properties in addition to anti-corrosion properties [8,52-55]. All parts of a plant can be used to prepare the inhibitor, but usually, the leaves are more important due to the abundance of phytochemicals [8]. In general, the reason for their popularity can be attributed to their cheap price, easy preparation method, and non-toxicity [8,52]. The inhibition mechanism and their inhibition efficiency (IE) depend on the active phytochemical compounds in them, and also the absorption mechanism is through three methods of chemisorption, physisorption, or a combination of the two (mixed) [8]. Table 3 reports the use of some plants as corrosion inhibitors in the sol-gel process.

4. Conclusions

In summary, silane-based sol-gel coatings were explored for their potential to protect metal structures, offering an alternative to toxic chromate-containing coatings. The sol-gel process has several advantages, including low processing temperatures, ease of operation, high chemical diversity, and the ability to coat various geometric shapes. Additionally, the use of plants as GCIs was reviewed. Given the acceptable performance of sol-gel coatings under different conditions and their environmental compatibility the adoption of these coatings is expected to increase in the future.

Conflict of Interest

The author declares no conflict of interest.

References

1. 1. D. Xia, et al. Electrochemical measurements used for assessment of corrosion and protection of metallic materials in the field: A critical review. *Journal of Materials Science & Technology*, **2022**, *112*, 151.
2. K.M. Shwetha, et al. A review on corrosion inhibitors: types, mechanisms, electrochemical analysis, corrosion rate and efficiency of corrosion inhibitors on mild steel in an acidic environment. *Results in Surfaces and Interfaces*. **2024**, *16*, 100258.
3. P. Baskar, et al. An Outline of Employing Metals and Alloys in Corrosive Settings with Ecologically Acceptable Corrosion Inhibitors. *Surfaces,* **2023**, *6*, 380.

Table 3. Use of plants in sol-gel hybrid coatings

Plants	Sol-Gel Solution Composition	Substrate	Corrosive medium	IE (%)	Ref.
Clitoria Ternatea	Mixing TEOS and GPTMS	MS	NaCl (3.5 wt.%)	86	18
Clitoria Ternatea	Mixing TEOS and GPTMS	Mild steel (MS)	HCl (0.5 M)	83.78	56
Caffeine extracted from tea leaves	Mixing TEOS and APTES	MS	NaCl (3.5 wt.%)	84.22	57
Ethanolic extract of Beta vulgaris	Mixing TEOS and APTES	MS	NaCl (3.5 wt.%)	83.03	58
Tea leaf aqueous extract	Mixing TEOS and APTES	MS	NaCl (3.5 wt.%)	85.66	59
Henna extract	Mixing TMSM and poly(methyl methacrylate)	Carbon steel (CS)	HCl (0.5 M)	95.6	60
Aqueous and ethanolic extracts of Mulberry	Mixing TEOS and GPTMS	Low-CS	NaCl (3.5 wt.%)	85.57	61
Henna extract	Polymerized vinyltrimethoxysilane	316L Stainless steel	SBF solution	92.53	62

© 2025 The Authors. This article is licensed under a Creative Commons Attribution 4.0 International License.

4. M. Sheydaei. Heavy Metals Contamination in Soil and Rice and their Removal Processes: A Brief Review. *Geomicrobiology Journal*, **2024**, *41*, 721.

5. M. Sheydaei. Investigation of Heavy Metals Pollution and Their Removal Methods: A Review. *Geomicrobiology Journal*, **2024**, *41*, 213.

6. M. Edraki and M. Sheydaei. Investigation of date seed powder as green corrosion inhibitor for mild steel: a study of solution and coating phases. *Hybrid Advances*, **2024**, *6*, 100238.

7. M. Sheydaei, et al. Matcha-modified clay polyurethane coating: improving thermal, mechanical, antimicrobial, and anticorrosion performance. *Iranian Polymer Journal*, **2023**, *32*, 1643.

8. M. Sheydaei. The Use of Plant Extracts as Green Corrosion Inhibitors: A Review. *Surfaces,* **2024**, *7*, 380.

9. B. Pradhan. A study on effectiveness of inorganic and organic corrosion inhibitors on rebar corrosion in concrete: A review. *Materials Today: Proceedings*, **2022**, *65*, 1360.

10. A.H. Khalaf, et al. Emerging AI technologies for corrosion monitoring in oil and gas industry: A comprehensive review. *Engineering Failure Analysis*. **2024**, *155*, 107735.

11. M. Edraki, et al. Protective nanocomposite coating based on ginger modified clay and polyurethane: preparation, characterization and evaluation anti-corrosion and mechanical properties. *Polymer Science, Series B*, **2022**, *64*, 756.

12. M. Edraki and M. Sheydaei. Investigation of the Dual Active/Barrier Corrosion Protection, Mechanical and Thermal Properties of a Vinyl Ester Coating Doped with Ginger Modified Clay Nanoparticles. *Russian Journal of Applied Chemistry*, **2022**, *95*, 1481.

13. S. Yadav, et al. Drugs: On Sustainable and Green Solution for the Prevention of Metallic Corrosion. *Journal of Bio-and Tribo-Corrosion,* **2023**, *9*, 79.

14. M. Sheydaei, et al. *Ganoderma Lucidum*-Modified Clay Epoxy Coating: Investigation of Thermal, Mechanical, Anticorrosion, and Antimicrobial Properties. *Polymer Science, Series B*, **2023**, *65*, 991.

15. M. Edraki, et al. Enhanced mechanical, anticorrosion and antimicrobial properties of epoxy coating *via* pine pollen modified clay incorporation. *Iranian Journal of Chemistry and Chemical Engineering,* **2023**, *42*, 2775.

16. D. Bokov, et al. Nanomaterial by sol-gel method: synthesis and application. *Advances in materials science and engineering*, **2021**, *1*, 5102014.

17. M. Parashar, et al. Metal oxides nanoparticles via sol–gel method: a review on synthesis, characterization and applications. *Journal of Materials Science: Materials in Electronics*, **2020**, *31*, 3729.

18. M. Sheydaei, et al. Anticorrosion and Antimicrobial Evaluation of Sol-Gel Hybrid Coatings Containing Clitoria ternatea Modified Clay. *Gels,* **2023**, *9*, 490.

19. Y. Wu, et al. 2D nanomaterials reinforced organic coatings for marine corrosion protection: State of the art, challenges, and future prospectives. *Advanced Materials*, **2024**, 2312460.

20. M. M. Megahed, et al. Flawless polyaniline coating for preservation and corrosion protection of ancient steel spearheads: an archaeological study from military museum, Al-Qala, Egypt. *Scientific Reports*, **2024**, *14*, 7215.

21. Y. He, et al. Investigation of Antiaging Performance and Service Life of OMMT/SBS Modified Bitumen Waterproof Membranes. *Journal of Materials in Civil Engineering*, **2024**, *36*, 04024025.

22. M. H. Nazari, et al. Nanocomposite organic coatings for corrosion protection of metals: A review of recent advances. *Progress in Organic Coatings*, **2022**, *162*, 106573.

23. R. B. Figueira, et al. Hybrid sol-gel coatings: Smart and green materials for corrosion mitigation. *Coating,* **2016**, *6*, 12.

24. S. Amiri and A. Rahimi. Hybrid nanocomposite coating by sol–gel method: A review. *Iranian Polymer Journal*, **2016**, *25*, 559.

25. O. Razaghi Kashani, et al. Self-Healing and Anti-Corrosion Nanocomposite Coatings Based on Polyurethane Nanocapsules containing Mercapto Benzimidazole. *Journal of Nanostructures*, **2022**, *12*, 726.

26. M. L. Zheludkevich, et al. Nanostructured sol–gel coatings doped with cerium nitrate as pre-treatments for AA2024-T3: corrosion protection performance. *Electrochimica Acta*, **2005**, *51*, 208.

27. P. Kardar and R. Amini. Study the self-healing properties of sol-gel coatings containing reversible tetra sulfide groups. *Advanced Materials and New Coatings*, **2020**, *8*, 2302.

28. G. Wu, et al. Robust microcapsules with polyurea/silica hybrid shell for one-part self-healing anticorrosion coatings. *Journal of materials chemistry A*, **2014**, *2*, 11614.

29. R. B. Figueira, et al. Organic–inorganic hybrid sol–gel coatings for metal corrosion protection: a review of recent progress. *Journal of Coatings Technology and Research*, **2015**, *12*, 1.

30. M. Masudi and A. Rahimi. silica based sol-gel nanocomposite coatings containing corrosion inhibitors. *Iran Polymer Technology, Research and Development*, **2017**, *2*, 27.

31. A. Javidparvar, et al. A review on the sol-gel based coatings used for the protection of metal substrates against corrosion. *Journal of Studies in Color World*, **2015**, *5(3)*, 31.

32. A. Dehghanghadikolaei, et al. Sol-gel process applications: A mini-review. *Proceedings of the Nature Research Society*, **2018**, *2(1)*, 02008.

© 2025 The Authors. This article is licensed under a Creative Commons Attribution 4.0 International License.

33. E. Alibakhshi, et al. Evaluation of the corrosion protection performance of mild steel coated with hybrid sol-gel silane coating in 3.5 wt.% NaCl solution. *Progress in Organic Coatings*, **2018**, *123*, 190.

34. H.Y. Su, et al. Sol–gel coatings doped with organosilane and cerium to improve the properties of hot-dip galvanized steel. *Corrosion Science*, **2016**, *102*, 63.

35. A. Samsadi Najibzad, et al. Feasibility of using an eco-friendly substitution of silane-based sol-gel based coatings for conversion coatings. *Journal of Studies in Color World*, **2019**, *9*, 1.

36. A. Zanurin, et al. Research progress of sol-gel ceramic coating: A review. *Materials today: proceedings*, **2022**, *48*, 1849.

37. N. Farhadyar, et al. 2005. Synthesis and Characterization of Hybrid Organic-inorganic Nanocomposite Coatings Based on Tetramethoxysilane and Epoxy Resin by Sol-gel Method. *Iranian Journal of Polymer Science and Technology*. **2005**, *18*, 19-27.

38. J. Gąsiorek, et al. Functionalizable sol-gel silica coatings for corrosion mitigation. *Materials*. **2018**, *11(2)*,197.

39. J. Li, et al. Advances in the modification of Silane-Based Sol-Gel coating to improve the corrosion resistance of magnesium alloys. *Molecules*. **2023**, *28(6)*, 2563.

40. L. Rodríguez-Alonso, et al. Hybrid sol-gel coatings doped with non-toxic corrosion inhibitors for corrosion protection on AZ61 magnesium alloy. *Gels*. **2022**, *8(1)*, 34.

41. S. Sfameni, et al. Waterborne eco-sustainable sol–gel coatings based on Phytic acid intercalated graphene oxide for corrosion protection of metallic surfaces. *International Journal of Molecular Sciences*. **2022**, *23(19)*, 12021.

42. Y. Li, et al. Preparation of sol-gel derived anticorrosive coating on Q235 carbon steel substrate with long-term corrosion prevention durability. *Materials*. **2019**, *12(12)*,1960.

43. T.N. Myasoedova, et al. Sol-gel materials for electrochemical applications: recent advances. *Coatings*. **2022**, *12(11)*,1625.

44. C.A. Hernández-Barrios, et al. Effect of cerium on the physicochemical and anticorrosive features of TEOS-GPTMS sol-gel coatings deposited on the AZ31 magnesium alloy. *Surfaces and Interfaces*. **2020**, *21*, 100671.

45. A. Nikbakht, et al. Silane coatings modified with hydroxyapatite nanoparticles to enhance the biocompatibility and corrosion resistance of a magnesium alloy. *RSC advances*. **2021**, *11(42)*, 26127.

46. J.P. Fernández-Hernán, et al. Anticorrosion and cytocompatibility assessment of graphene-doped hybrid silica and plasma electrolytic oxidation coatings for biomedical applications. *ACS Biomaterials Science & Engineering*. **2021**, *7(12)*, 5861-77.

47. Z. Chen, et al. Microstructural Changes of the Peo Coating Induced by Silane-Based Sol–Gel Treatment. *Surface Review and Letters*. **2022**, *29(07)*, 2250098.

48. B.K. Jiang, et al. Corrosion resistance enhancement of magnesium alloy by N-doped graphene quantum dots and polymethyltrimethoxysilane composite coating. *Carbon*. **2020** ,*157*, 537.

49. Y. Wang, et al. An organic/inorganic composite multi-layer coating to improve the corrosion resistance of AZ31B Mg alloy. *Surface and Coatings Technology*. **2019**, *360*, 276.

50. L.Y. Cui, et al. Corrosion resistance of a self-healing micro-arc oxidation /poly methyl tri methoxysilane composite coating on magnesium alloy AZ31. *Corrosion Science*. **2017**,*118*,84.

51. H. Ashassi-Sorkhabi, et al. Salt-nanoparticle systems incorporated into sol-gel coatings for corrosion protection of AZ91 magnesium alloy. *Progress in Organic Coatings*. **2019**, *135*,475.

52. M. Edraki, et al. A brief review of the performance of azole-type organic corrosion inhibitors. *Chemical Review and Letters*. **2022**, *6(1)*, 79.

53. M. Edraki, et al. Characterization and antimicrobial properties of Matcha green tea. *Chemical Review and Letters*. **2022**, *5(1)*, 76.

54. M. Sheydaei, et al. An overview of the use of plants, polymers and nanoparticles as antibacterial materials. *Chemical Review and Letters*. **2022**, *5(3)*, 207.

55. M. Sheydaei and M. Edraki. Vinyl ester/C-MMT nanocomposites: investigation of mechanical and antimicrobial properties. *Journal of Chemistry Letters*. **2022**, *3*, 95.

56. N.A. Ghuzali, et al. Study on Clitoria ternatea extracts doped sol-gel coatings for the corrosion mitigation of mild steel. *Applied Surface Science Advances*. **2021**,*6*,100177.

57. T.S. Hamidon and M.H. Hussin. Susceptibility of hybrid sol-gel (TEOS-APTES) doped with caffeine as potent corrosion protective coatings for mild steel in 3.5 wt.% NaCl. *Progress in Organic Coatings*. **2020**, *140*, 105478.

58. N.F. Norizan, et al. Corrosion-resistant performance of mild steel employing flavonoids and phenols-rich Beta vulgaris extract-doped hybrid sol-gel coatings. *Journal of Sol-Gel Science and Technology*. **2023**, *107(2)*, 347.

59. T.S. Hamidon, et al. Enhanced corrosion inhibition of low carbon steel in aqueous sodium chloride employing sol–gel-based hybrid silanol coatings. *Journal of Sol-Gel Science and Technology*. **2021**, *97*, 556.

60. Z. Khoshkhou, et al. Corrosion inhibition of henna extract on carbon steel with hybrid coating TMSM-PMMA in HCL solution. *Open Journal of Synthesis Theory and Applications*. **2018**, *7(1)*, 1.

© 2025 The Authors. This article is licensed under a Creative Commons Attribution 4.0 International License.

61. N.A. Mohamad Azran, et al. Corrosion-resistant mulberry fruit (Morus nigra L.) extracts incorporated hybrid (GPTMS-TEOS) composite silanol coatings for low carbon steel protection. *Journal of Sol-Gel Science and Technology*. **2023**, *105*,734.

62. A. Motalebi, et al. Improvement of corrosion performance of 316L stainless steel via PVTMS/henna thin film. *Progress in Natural Science: Materials International*. **2012**, *22*,392.

Author Biography

Milad Sheydaei is an Assistant Professor at the Department of Chemical Engineering at the University of Garmsar. He received his Ph.D. in Polymer Engineering from Sahand University of Technology in 2021. His research interests and expertise include polysulfide rubbers, green corrosion inhibitors, antimicrobial materials, and sustainable polymer nanocomposites. He also works on food safety and the evaluation of toxic metals.

Milad Edraki currently works as a lecturer in the Department of Industrial Chemistry at Technical and Vocational University (Faculty of Chamran, Rasht Branch). He received his Ph.D. degree in Polymer Engineering from South Tehran Branch – Islamic Azad University in January 2019 under the supervision of Associate Professor Davood Zaarei. The research fields in which he has interest and expertise include corrosion, nanomaterial's synthesis, formulation, and Characterization of paints & surface coatings.

© 2025 The Authors. This article is licensed under a Creative Commons Attribution 4.0 International License.

Mechanically Synthesized Zirconium-based MOFs for Adsorptive Removal of Nerve Agent Simulants

Hosein Ghasempour *, Behnam Habibi, Paria Soleimani Abhari

Department of Chemistry, Faculty of Sciences, Tarbiat Modares University, Tehran, Iran

Editor's note: Metal-organic frameworks (MOFs) have shown great potential for the adsorptive removal of various hazardous compounds due to their high specific surface areas and tunable molecular structures. Ghasempour et al. reported an easy, eco-friendly solvent-assisted mechanochemical grinding method for synthesizing Zr-based MOFs, which exhibit a high removal capacity against organophosphorus nerve agents.

doi: 10.22034/jams.2025.210132

How to cite: H. Ghasempour et al. *Journal of Applied Material Science*, **2025**, *1*, 210132.

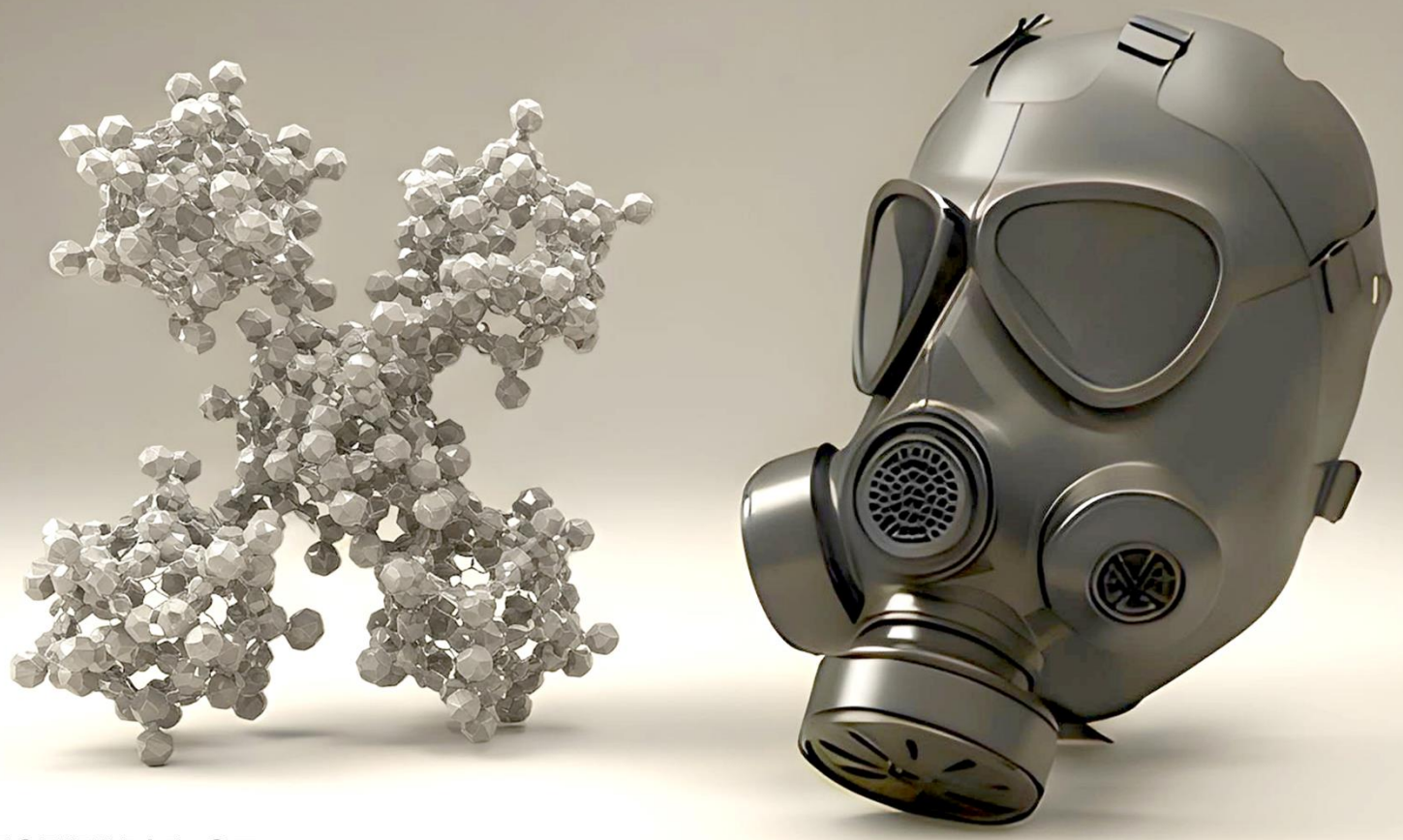

JOURNAL OF
APPLIED
MATERIAL
SCIENCE
jams.hsu.ac.ir

© 2025 *J. Appl. Mat. Sci.* This material is licensed under a Creative Commons Attribution 4.0 International License.

Journal of Applied Material Science **2025**, *1*, 210132
How to cite: H. Ghasempour et al., *Journal of Applied Material Science*, **2025**, *1*, 210132.
Journal homepage: **www.jams.hsu.ac.ir**

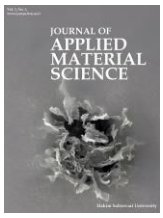

Original Research

Mechanically Synthesized Zirconium-based MOFs for Adsorptive Removal of Nerve Agent Simulants

Hosein Ghasempour *, Behnam Habibi, Paria Soleimani Abhari

Department of Chemistry, Faculty of Sciences, Tarbiat Modares University, Tehran, Iran

Abstract

In this study, two zirconium-based metal-organic frameworks (Zr-MOFs), namely UiO-66 and NH_2-UiO-66, were synthesized using a simple, fast, and eco-friendly solvent-assisted grinding (mechanochemically) approach. The purity and quality of prepared Zr-MOFs were fully characterized via powder X-ray diffraction (PXRD), Fourier transform infrared (FT-IR) spectroscopy, and N_2 adsorption/desorption analyses. Due to its structural similarity to phosphorus nerve agents, dimethyl methylphosphonate (DMMP) was used in this study as the model nerve agent to evaluate the adsorption capacity of prepared Zr-MOFs toward nerve agents. Photoluminescence (PL) spectroscopy was employed to monitor the DMMP concentration during the removal process. Adsorption capacity values of 667 and 834 mg/g were obtained for UiO-66 and NH_2-UiO-66, respectively, indicating their strong interaction with phosphorus nerve agents. Furthermore, the stability and recyclability of the absorbents after the absorption process were confirmed using FT-IR and PXRD results, confirming that Zr-MOFs are perfect candidates for applications related to chemical warfare protection.

Keywords: Metal-organic frameworks; Phosphorus nerve agents; DMMP; Adsorptive removal.

1. Introduction

Chemical warfare agents (CWAs) are a class of chemicals designed to kill, harm, or incapacitate human beings [1]. More than 70 types of compounds have been employed or stored as CWAs in liquid, gas, or solid form during the 20th century [2]. CWA can be categorized based on their biological effects on human health. They may also be classified by their chemical structure or their strategic purpose. Some of the most known CWAs are blister agents, pulmonary/choking agents, blood agents, nerve agents, vomiting agents, and incapacitating agents. It is crucial to take precautions to avoid exposure to these agents.

Among various types of CWAs, organophosphorus nerve agents (OPNs) are considered a serious hazard to living organisms due to their high production rate as a byproduct in phosphorus pesticide manufacturing. One of the distinguishing features of OPNs, compared to other CWAs, is their extreme toxicity, which arises from their ability to bind to the acetylcholinesterase enzyme (AChE) in the synaptic space, leading to neurological impairment and ultimately death [3]. The reactivity of

* Corresponding author.
Email addresses: h.ghasempour@modares.ac.ir, h.ghasempoor92@gmail.com (H. Ghasempour)

Received 9 January 2025
Revised 30 January 2025
Accepted 31 January 2025
Available online 1 February 2025

https://doi.org/10.22034/jams.2025.210132
© 2025 The Authors. This article is licensed under a Creative Commons Attribution 4.0 International License.

OPNs is related to their similarity in structure to organophosphate esters, which contain a P=O group, a leaving group (X), and two alkyl/alkoxy substituents (Scheme 1a).

Due to their structural similarity, phosphonate ester pesticides such as paraoxon, and dimethyl nitrophenyl phosphate (DMNP) have been extensively studied as G-type nerve agents, for example, tabun (GA), sarin (GB), and soman (GD) (Scheme 1b). Another G-type nerve agent simulant is dimethyl methylphosphate (DMMP), which, despite its structural resemblance to G-type nerve agents, exhibits significantly lower biological toxicity (Scheme 1c). For this reason, DMMP is one of the most commonly used nerve agent alternatives in research studies aimed at counteracting G-type nerve agents [4].

Metal-organic frameworks (MOFs) are a subset of coordination polymers constructed by connecting metal ions to organic ligands through coordination bonds [5]. Some characteristic properties of these materials include their high structural diversity, extremely high porosity, and tunable functionality [6]. MOFs have been considered for diverse applications, such as gas sorption and separation [7, 8], catalysis [9], and drug delivery [10]. In addition, these materials have attracted great attention due to their high potential for adsorptive removal of CWAs and toxic industrial chemicals (TICs) [3, 11]. Many studies have shown that Zirconium (VI)-based MOFs (Zr-MOFs) exhibit remarkable activity in the catalytic hydrolysis of OPNs [12].

The ability of Zr-MOFs to remove simulants of CWAs, such as DMMP, from aqueous environments is contributed to the presence of Zr–OH–Zr moiety on their clusters, which enables them to mimic the phosphodiesterase enzyme with a Zn–OH–Zn active center [13]. Awual et al. evaluated the adsorption of OPNs and their simulants on Zr-MOFs and concluded that OPNs interact with the framework through hydrogen bonding with Zr–OH sites, highlighting the critical role of this type of interaction at low concentrations [14]. In another similar work, Florénzia et al. investigated the impact of the network topology of Zr-MOFs on their adsorption capacity toward OPNs. This study concluded that the topology-based properties of Zr-MOFs, like specific surface area, pore aperture diameter, metal node connectivity, and accessibility to Lewis acidic Zr(VI) nodes, play a critical role in the adsorption and detoxification of sarin [15]. Herein, two classical Zr-MOFs, UiO-66 and NH_2-UiO-66, were mechanochemically fabricated to investigate their performance to remove the DMMP, as a nerve agent simulant from an aqueous solution. For the first time, photoluminescence spectroscopy was employed to study the adsorption of DMMP by Zr-MOFs.

2. Experimental

2.1. Materials

N,N-dimethylformamide (DMF), chloroform ($CHCl_3$), deuterated chloroform ($CDCl_3$), zirconium tetrachloride ($ZrCl_4$), Methanol, ethyl acetate, acetic acid, terephthalic acid (H_2BDC), 2-aminobenzenedicarboxylic acid (NH_2BDC), dimethyl methylphosphonate (DMMP), potassium bromide (KBr), and N-ethylmorpholine were purchased commercially and used without any purification.

2.2. Mechanical Synthesis of Zr-MOFs.

Zr-MOFs were synthesized by grinding method (Figure 1a). In this process, 3 mmol $ZrCl_4$ (0.7 g) and 3 mmol of the organic ligand (0.5 g of H_2BDC and 0.54 g of NH_2BDC for UiO-66 and NH_2-UiO-66, respectively) were ground together for 2 minutes to homogenize the powder. The resulting homogenous mixture was then wetted with 5 drops of DMF solvent. Subsequently, the

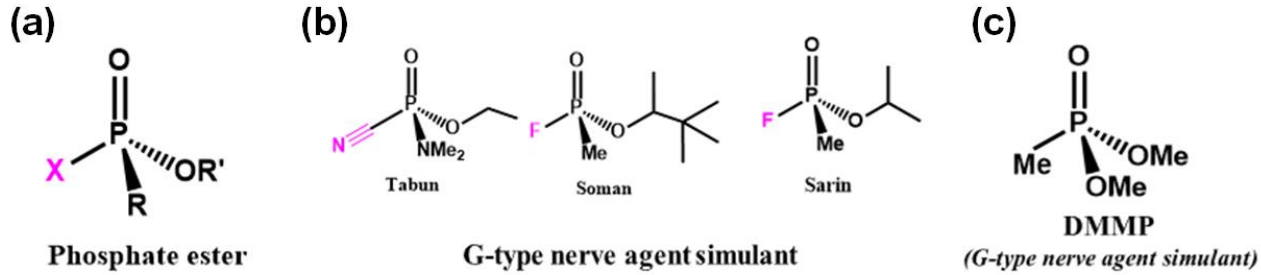

Scheme 1. The chemical structure of (a) phosphate ester, (b) G-type nerve agents, and (c) DMMP as a G-type nerve agent simulant.

© 2025 The Authors. This article is licensed under a Creative Commons Attribution 4.0 International License.

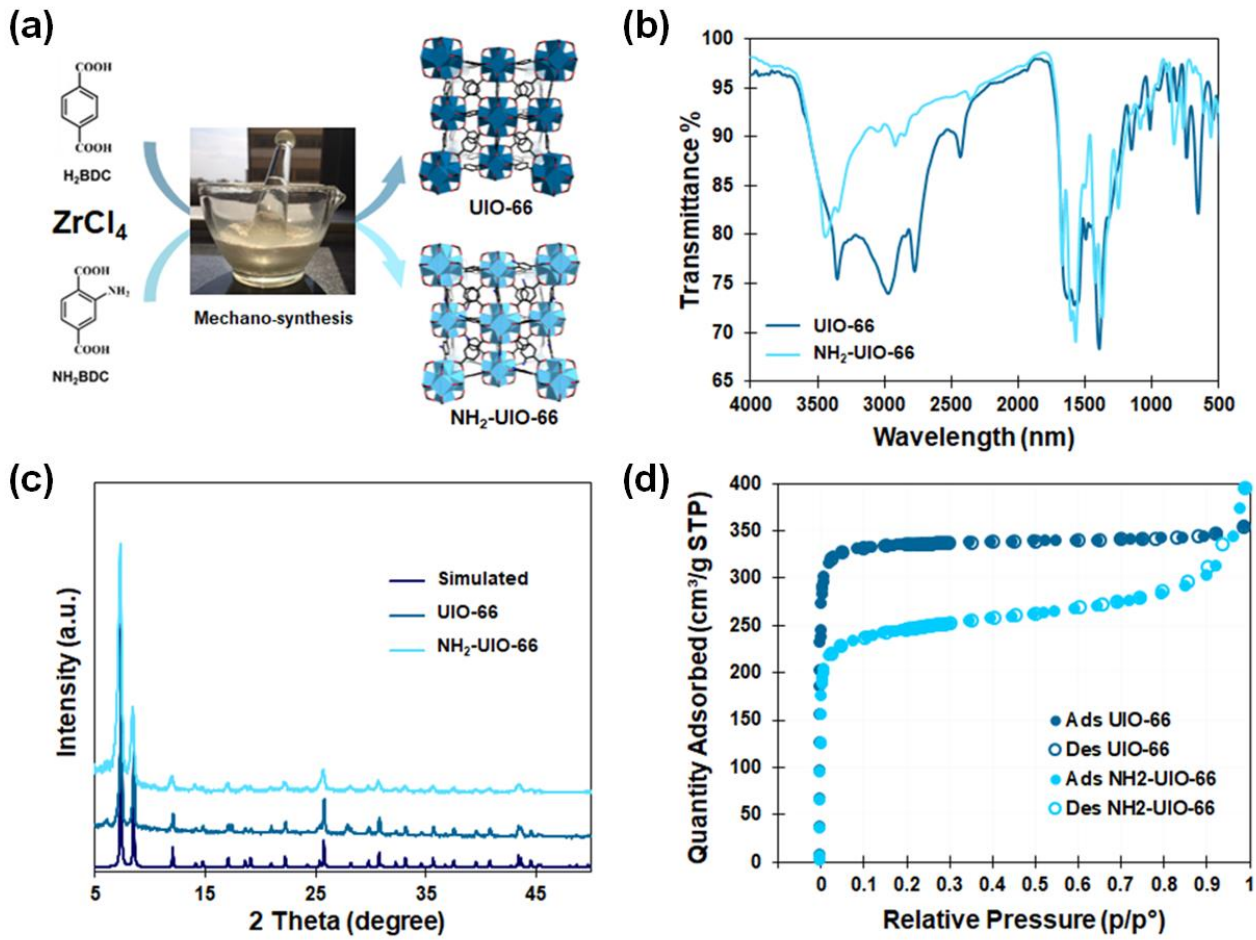

Figure 1. (a) Brief illustration of the mechanical synthesis of Zr-MOFs, characterization of prepared Zr-MOFs with (b) FT-IR, (c) PXRD, and (d) N_2 adsorption/desorption results.

solid-state mechanochemical synthesis was carried out for 30 minutes. The obtained powder was washed three times with a trace volume of DMF to eliminate the unreacted initial precursors. The washed sample was dried in a preheated oven under 100 °C and activated through vacuum degassing at 120 °C overnight.

2.3. *Measurements*

The materials were weighed using an analytical Sartorius balance with an accuracy of one milligram. Powder X-ray diffraction (PXRD) patterns were obtained using a Philips X'Pert diffractometer with a CuKα X-ray source (λ = 1.54 Å) over a 2θ range of 3–70°. Fourier transform infrared (FT-IR) spectra were recorded on a Thermo Nicolet FTS-7 spectrometer using the KBr pellet technique. UV spectra were collected using a Varian Cary 50 spectrophotometer. The nitrogen (N_2) sorption measurements were performed using a Micromeritics TriStar II 3020 volumetric gas adsorption instrument to calculate the BET surface area. A Perkin Elmer LS-5 luminescence spectrometer was employed to record the fluorescence emission spectra. A Hettich EBA20 centrifuge made in Germany was used for the centrifugation.

To evaluate the removal efficiency of adsorbents toward DMMP, 50 milligrams of Zr-MOFs were added to a DMMP solution in varying concentrations (100-800 ppm) and allowed to equilibrate under ambient conditions. The PL spectrum of the adsorbent-DMMP mixture was then measured to determine the adsorption capacity. The removal efficiency (R %) and adsorption capacity (Q_e, mg/g) of the adsorbent at equilibrium were calculated using equations (1) and (2), respectively:

© 2025 The Authors. This article is licensed under a Creative Commons Attribution 4.0 International License.

$$R\,\% = ((C_0 - C_e)/C_0) \times 100 \quad (1)$$

$$Q_e = (C_0 - C_e)\,V/m \quad (2)$$

where m, V, C_0, and C_e represent the mass of the adsorbent (mg), the volume of the DMMP solution (mL), and initial and equilibrium concentrations of DMMP (mg/L), respectively.

3. Results and discussion

As shown in Figure 1b, the FT-IR spectra of the as-prepared Zr-MOFs were compared. The evidence for Zr-MOFs formation is the disappearance of the broad band above 2500 cm^{-1}, which corresponds to hydrogen bonding in free organic ligands. Additionally, the presence of absorption bands at 1350-1700 cm^{-1}, corresponding to the symmetric and asymmetric stretching vibrations of the carboxylate groups, confirms the formation of Zr-MOFs. In the FT-IR spectrum of NH_2-UiO-66, a doublet band is observed in the range of 3350–3450 cm^{-1}, which can be attributed to the primary amine (-NH_2) group of the NH_2BDC linker. Moreover, multiple peaks associated with the –COO functional groups of the linkers appeared in the 1400–1650 cm^{-1} region.

A comparison of the experimentally measured PXRD patterns of the synthesized Zr-MOFs and the extracted pattern from the crystallographic data of UiO-66 confirms the successful synthesis of Zr-MOFs (Figure 1c). Moreover, the BET surface area values of UiO-66 and NH_2-UiO-66, determined *via* N_2 adsorption/desorption isotherms at 77 K, were 1323 and 963 m^2/g, respectively (Figure 1d). This range of surface area falls within the reported range for Zr-MOFs [16].

As previously mentioned, despite its high structural and physical similarity to G-type nerve agents, DMMP exhibits significantly lower biological toxicity. For this reason, it is widely used as one of the most common simulants for studying the detection and removal of G-type nerve agents. However, monitoring the concentration of DMMP presents significant challenges, as this material is not readily detectable by UV-Vis spectroscopy and gas chromatography.

Fortunately, according to the literature, DMMP can be easily detected by photoluminescence (PL) spectroscopy in aqueous solution [17]. Studies have shown that this molecule emits a very strong fluorescence emission band around 320 nm under exciting at 290 nm (λ_{max}) wavelength radiation. Therefore, in this study, the adsorption of this nerve agent simulant by UiO-66 and NH_2-UiO-66 adsorbents was investigated using the PL technique.

Combating chemical weapons such as phosphorus nerve agents in real-world conditions, especially in humid environments, presents significant challenges. Therefore, the main objective of this study is to adsorb DMMP from an aqueous environment. To achieve this, the fluorescence properties of DMMP, a simulant for nerve agents, in water need to be investigated. The preliminary test results showed that the fluorescence behavior of DMMP is not significantly dependent on the solvent. Similar to DMSO, the DMMP aqueous solution exhibits strong emission upon excitation. The only difference is that the excitation wavelength required for this strong emission in water is 280 nm instead of 290 nm (λ_{max}) as shown in Figure 2a.

In other words, DMMP exhibits its strongest fluorescence emission band upon excitation with a 280 nm wavelength instead of 290 nm, making it necessary to use a lower excitation wavelength for further work. To ensure that the DMMP fluorescence emission remains stable over time, 10 microliters of 50 ppm DMMP solution were transferred to 4 ml of distilled water in a fluorescence cell and scanned at different time intervals under 280 nm excitation. As illustrated in Figure 2b, there is no observable decrease in the fluorescence emission intensity of DMMP passing time, even after 24 hours.

For the preliminary test, a very small amount of UiO-66 (the tip of a spoon) was added to the same fluorescence cell, and the fluorescence spectrum was recorded again at the same excitation wavelength the next day. Figure 2b shows that the fluorescence emission of DMMP was completely quenched, which could indicate the adsorptive removal of DMMP from the solution by the adsorbent. To calculate the removal efficiency of adsorbents, 50 milligrams of UiO-66 and NH_2-UiO-66 Zr-MOFs were added to DMMP solution with different concentrations (100-800 ppm) and allowed to equilibrate.

The fluorescence spectrum of the adsorbent-DMMP mixture was then measured to investigate the progress of adsorption, as shown in Figures 2c and d. As expected, DMMP shows a significant decrease in the intensity of its fluorescence emission in the presence of

© 2025 The Authors. This article is licensed under a Creative Commons Attribution 4.0 International License.

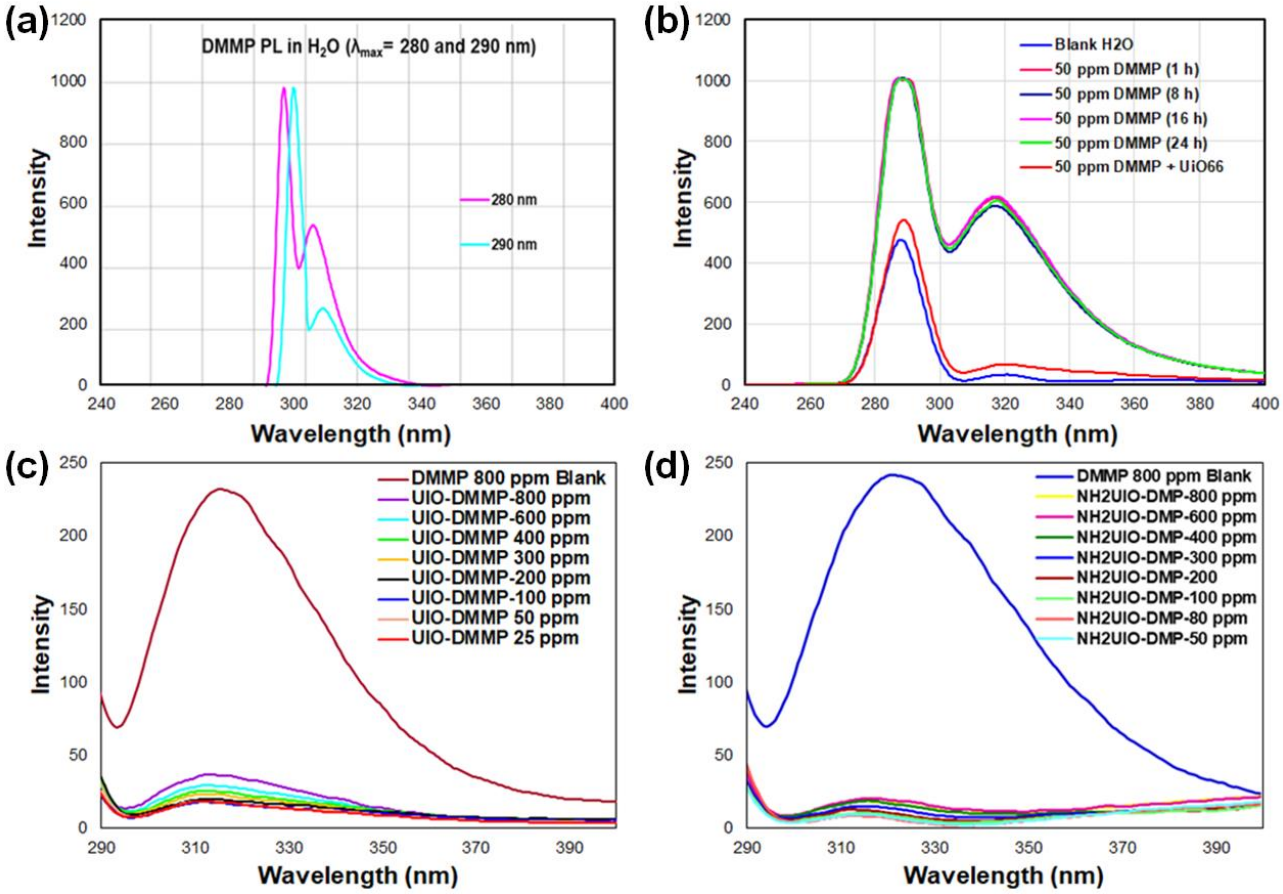

Figure 2. (a) Comparison of fluorescence emission spectra of DMMP in H_2O excited at 280 and 290 nm, (b) fluorescence emission spectra of DMMP in H_2O over time, as well as fluorescence emission spectra of DMMP at different concentrations in the presence of (c) 50 mg UiO-66 and (d) 50 mg NH_2-UiO-66 adsorbent.

the adsorbents, which is also evident from the PL spectra. The data showed that DMMP was completely removed at concentrations up to approximately 200 ppm. However, increasing the concentration above 400 ppm resulted in some remaining DMMP in the environment. The high adsorption capacity of UiO-66 and NH_2-UiO-66 toward DMMP can be identified by comparing the fluorescence emission intensity of blank DMMP solution with that of solution in the presence of the adsorbents at the same 800 ppm concentration (Figures 2c and d).

Based on the results, the intensity of the DMMP fluorescence band is significantly lower in the presence of the adsorbents compared to the control solution. Moreover, the removal efficiency for DMMP removal by UiO-66 and NH_2-UiO-66 is very high. According to equation (1), the removal efficiency for 200, 300, and 400 ppm DMMP concentrations are 97.3%, 89.7%, and 79.1% for the UiO-66 adsorbent, and 98.9%, 95.6%, and 95.3% for the NH_2-UiO-66 adsorbent, respectively. These results indicate that the adsorbents possess a very promising ability to remove DMMP, a pseudo nerve agent, from an aqueous environment, especially NH_2-UiO-66 adsorbent, which demonstrates a higher adsorption capacity than UiO-66 despite its relatively lower surface area.

According to the results, the superior performance of this framework with functionalized pores and surfaces containing free amino groups can be justified. These amino groups facilitate faster and more efficient adsorption of phosphorus nerve agents through increased hydrogen bonding interactions. To study the

© 2025 The Authors. This article is licensed under a Creative Commons Attribution 4.0 International License.

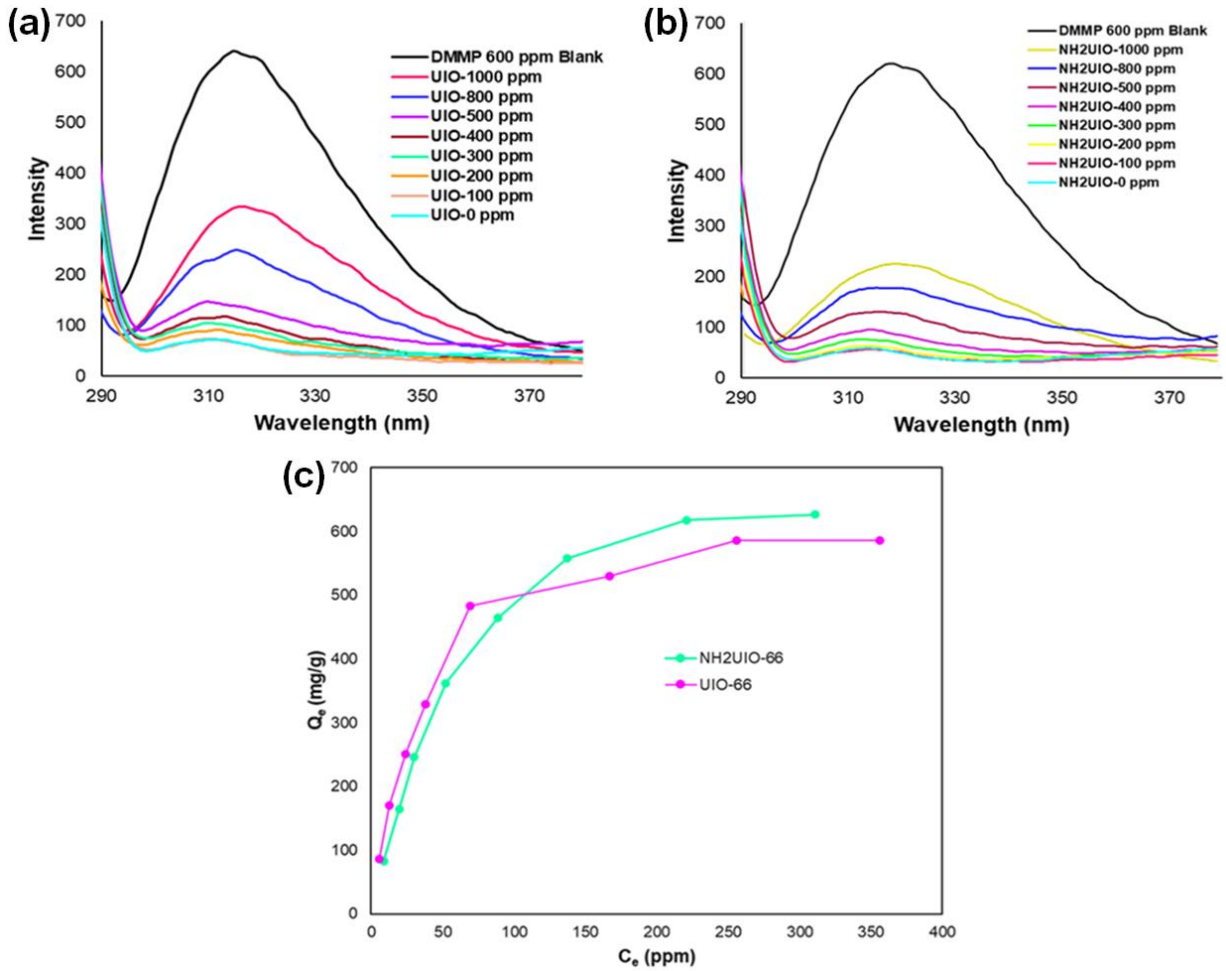

Figure 3. Fluorescence emission spectra of DMMP at different concentrations in the presence of (a) 10 mg UiO-66 and (b) 50 mg NH_2-UiO-66 adsorbent (b); (c) Comparison of the Q_e vs C_e plots for UiO-66 and NH_2-UiO-66 at different DMMP concentration.

adsorption of DMMP accurately and determine the relationship between the adsorption capacity Q_e (mg/g) of the adsorbent and the equilibrium concentration of the adsorbed substance, C_e (mg/L), at a constant temperature, Langmuir and Freundlich isotherm models were used. The equation (3) below shows the linear formula of the Langmuir equation;

$$C_e/q_e = 1/(K_l.q_m) + C_e/q_m \quad (3)$$

where q_m (mg/g) and K_l (L/mg) are the maximum adsorption capacity and the Langmuir adsorption rate constant (which reflects the dependence of adsorbent and adsorbate), respectively. The Freundlich isotherm defines non-ideal and reversible adsorption, which is attributed to multiple-layer adsorption on heterogeneous surfaces. This model can be expressed by equation (4):

$$log\ q_e = log\ K_F + 1/n\ log\ C_e \quad (4)$$

where K_F is the Freundlich constant, and 1/n is the adsorption intensity.

Typically, Langmuir and Freundlich adsorption isotherms provide valuable insights into the adsorption mechanism and behavior of the adsorbent. The Langmuir model defines the reversible chemical equilibrium between the adsorbent surface and the solution. This model adjudges that adsorption occurs uniformly as a monolayer on the surface of the adsorbent and that the adsorbed substance does not penetrate the surface of the adsorbent. The Langmuir isotherm is linear, as represented by equation (2). According to the Langmuir isotherm model, K_l is the Langmuir adsorption rate constant in L/mg, and Q_m is the

© 2025 The Authors. This article is licensed under a Creative Commons Attribution 4.0 International License.

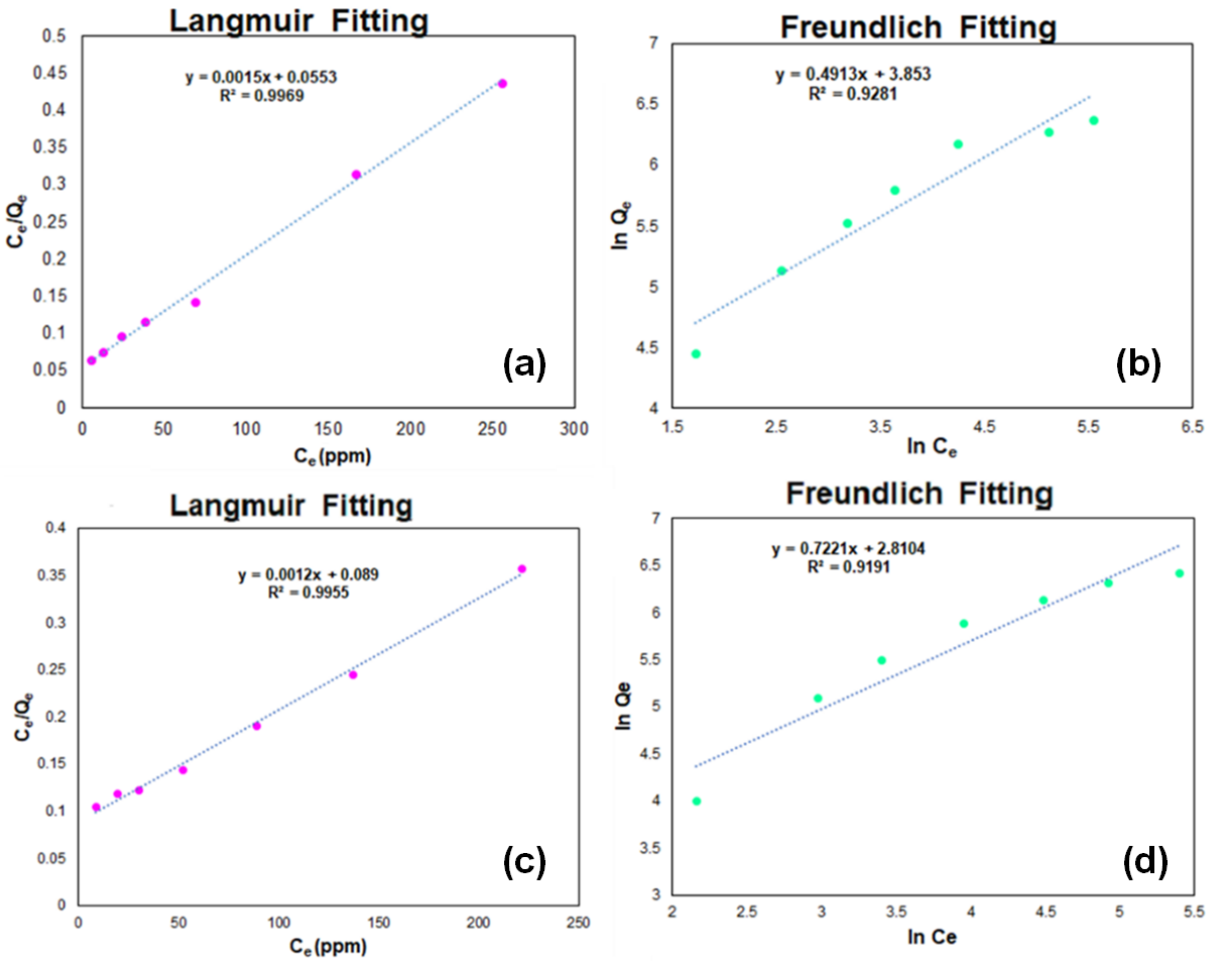

Figure 4. Langmuir and Freundlich fitting of experimental adsorption of DMMP by (a and b) UiO-66 and (c and d) NH_2-UiO-66 adsorbents.

maximum adsorption capacity in mg/g. The Freundlich isotherm is a non-ideal and reversible adsorption model in which adsorption occurs as a non-uniform multilayer on the adsorbent surface. Equation (4) reveals the relationship between adsorption capacity and the adsorbed concentration in the Freundlich adsorption model, where K_F and 1/n are the Freundlich constant and the adsorption intensity, respectively. The value of n also describes the desirability/undesirability of the adsorption intensity respectively.

To calculate the maximum adsorption capacity, 10 mg of the Zr-MOFs were immersed in a DMMP solution with varying concentrations (100-1000 ppm). The fluorescence spectrum of the adsorbent-DMMP mixture was measured to monitor the progress of adsorption, as shown in Figures 3a and b. Interestingly, the intensity of DMMP fluorescence in the 1000 ppm solution was significantly lower in the presence of the adsorbent compared to the control solution with a concentration of 600 ppm.

According to the experimental data, only 10 milligrams of the adsorbent is sufficient to almost completely quench the fluorescence band of DMMP solutions at a concentration of 200 ppm. At first glance, it appears that the adsorption capacity of NH_2-UiO-66 is higher than that of UiO-66. However, to confirm this, the adsorption isotherm, Langmuir and Freundlich plots were drawn. For this purpose, the experimental results obtained from both Langmuir and Freundlich models were evaluated to determine which model corresponds to the adsorption process. The Langmuir plot is obtained by plotting the ratio of equilibrium concentration to the corresponding adsorption capacity (C_e/Q_e) against the equilibrium concentration (C_e), while the Freundlich

© 2025 The Authors. This article is licensed under a Creative Commons Attribution 4.0 International License.

diagram is obtained by plotting the natural logarithm of the adsorption capacity (ln Q_e) versus the natural logarithm of the equilibrium concentration (ln C_e) (Figure 4). The obtained correlation coefficients R^2 (0.9969 and 0.9281 for Langmuir and Freundlich models, respectively, for UiO-66 adsorbent, and 0.9955 and 0.9191 for Langmuir and Freundlich models, respectively, for NH_2-UiO-66 adsorbent) indicate that DMMP adsorption by both adsorbents follows the Langmuir model, meaning that DMMP molecules interact uniformly and monolayer on the adsorbent surface and are adsorbed.

Given that the Langmuir adsorption is applicable, equation (3) was used to calculate the maximum adsorption capacity (Q_{max}), where the inverse of the slope is equal to Q_{max}. The calculated adsorption capacities for UiO-66 and NH_2UiO-66 were 667 and 834 mg/g, respectively, indicating the very high potential of these adsorbents for removing phosphorus nerve agents from an aqueous environment. The obtained maximum adsorption capacity for NH_2UiO-66 is approximately 25% higher than that of UiO-66, suggesting that the functional groups in NH_2-UiO-66 significantly enhance the adsorption performance. The only difference between two Zr-MOFs studied is the free amino decorated wall of NH_2-UiO-66 framework (Figure 1a), which can play a critical role in the enhancement of the adsorption capacity.

Using the Langmuir equation, the Langmuir adsorption isotherm can be obtained by plotting the adsorption capacity at equilibrium (Q_e) versus the concentration of DMMP at equilibrium (C_e). Figure 3c shows a comparison of the Langmuir adsorption isotherms for the two adsorbents. As observed, the adsorption behavior of both frameworks is very similar, with the notable difference that at low equilibrium concentrations (0 to 100 ppm), DMMP adsorption by UiO-66 occurs slightly faster than that of NH_2-UiO-66. However, as the concentration increases beyond 500 ppm, the adsorption capacity of NH_2-UiO-66 reaches

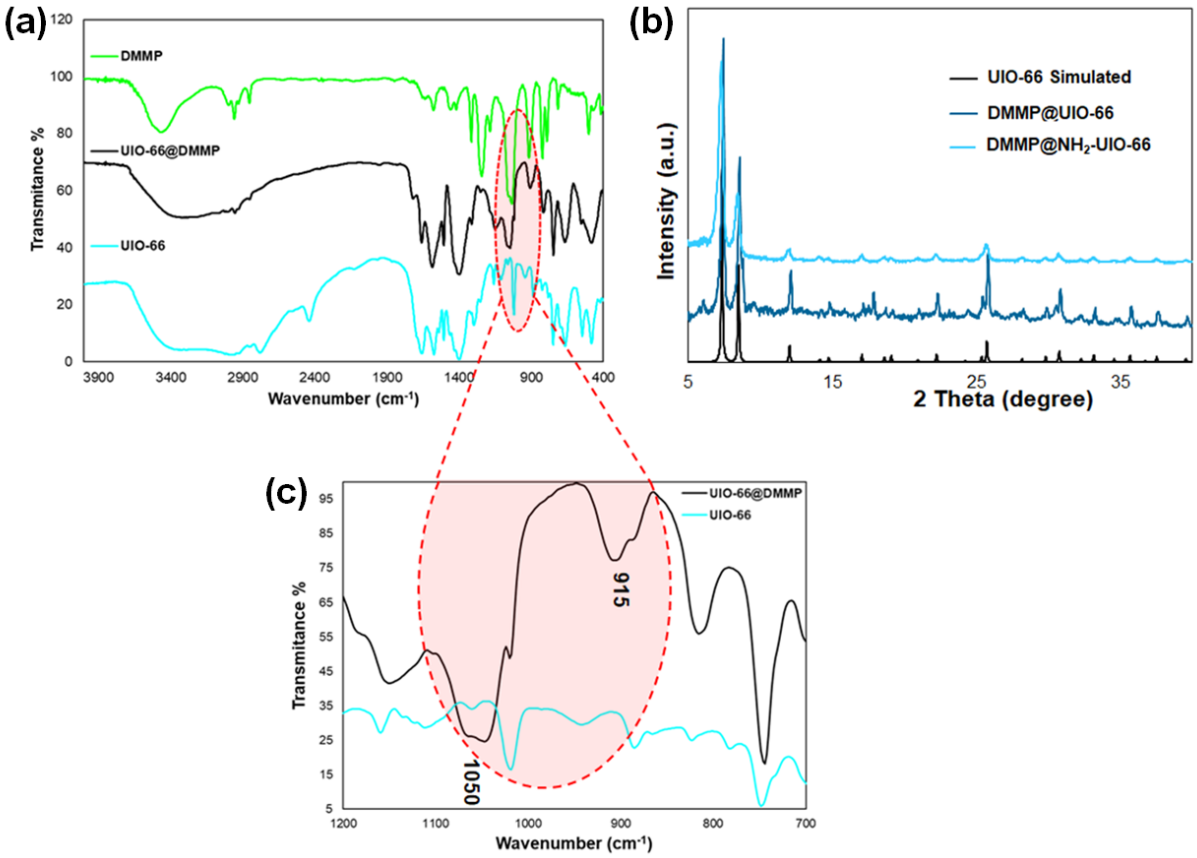

Figure 5. (a) FT-IR spectra of DMMP and UiO-66, before and after the adsorption of DMMP, (b) comparison of the simulated XRD pattern of UiO-66 with experimental PXRD of Zr-MOFs after adsorption of DMMP, and (c) selected wavenumber region of FTIR in panel a for UiO-66, before and after the adsorption of DMMP.

© 2025 The Authors. This article is licensed under a Creative Commons Attribution 4.0 International License.

saturation later than UiO-66. This difference in behavior can be attributed to the presence of functional amino groups in the NH_2-UiO-66 framework, which, despite the higher surface area of UiO-66, may contribute to stronger interactions and a slower but more efficient adsorption process at higher concentrations.

FT-IR and PXRD were applied to determine the absorbed DMMP on Zr-MOFs and to investigate the stability of the absorbent after absorption. Figure 5a shows the comparison of FT-IR spectra of DMMP, UiO-66, and DMMP@UiO-66 (after absorption) in the 400 to 2000 nm region. A magnified representation of the FT-IR spectrum in Figure 5c clearly shows two absorption bands at the wavenumbers of 915 and 1050 cm^{-1} in the spectrum of DMMP@UiO-66 (black line), which can be attributed to the P=O and C-P-C bonds in DMMP. These bands are not observed in the spectrum of pristine UiO-66 (blue line), confirming the presence of absorbed DMMP on the surface of the Zr-MOFs. To investigate the stability of the absorbent after absorption, we used the PXRD technique, and the results are presented in Figure 5b. As is evident from the figure, the lack of any shift in the peak positions or any significant decrease in their intensities indicates the stability of UiO-66 and NH_2-UiO-66 absorbents after absorption.

4. Conclusions

This study represented the green fabrication of two famous Zr-based MOFs, UiO-66 and NH_2-UiO-66, using a rapid and simple mechanochemical method, and their performance in adsorptive removal of OPNs. To investigate the ability of these absorbents to remove OPNs, DMMP, was used as a simulant model. Langmuir and Freundlich adsorption models were applied to calculate the maximum adsorption capacity, and it was found that DMMP adsorption by UiO-66 and NH_2-UiO-66 absorbents follows the Langmuir model. The adsorption capacity values for UiO-66 and NH_2-UiO-66 were calculated to be 667 and 834 mg/g, respectively, indicating their high capacity for adsorptive removal of nerve agents from the aqueous environment. Furthermore, the stability and recyclability of the absorbents after the absorption process were confirmed using FT-IR and PXRD techniques, demonstrating that Zr-MOFs are very promising materials to chemical weapon protection.

Conflict of Interest

The author declares no conflict of interest.

References

1. Y.C. Yang, J.A. Baker, and J.R. Ward. Decontamination of chemical warfare agents. *Chemical Reviews*, **1992**, *92*, 1729.

2. J.B. DeCoste and G.W. Peterson. Metal–organic frameworks for air purification of toxic chemicals. *Chemical reviews*, **2014**, *114*, 5695.

3. N.S. Bobbitt, et al. Metal–organic frameworks for the removal of toxic industrial chemicals and chemical warfare agents. *Chemical Society Reviews*, **2017**, *46*, 3357.

4. S. Mukherjee and R.D. Gupta. Organophosphorus nerve agents: types, toxicity, and treatments. *Journal of toxicology*, **2020**, *2020*, 3007984.

5. Q. Bao and K.P. Loh. Graphene photonics, plasmonics, and broadband optoelectronic devices. *ACS nano*, **2012**, *6*, 3677.

6. H. Ghasempour, et al. Metal–organic frameworks based on multicarboxylate linkers. *Coordination Chemistry Reviews*, **2021**, *426*, 213542.

7. J.-R. Li, J. Sculley, and H.-C. Zhou. Metal–organic frameworks for separations. *Chemical reviews*, **2012**, *112*, 869.

8. H. Li, et al. Porous metal-organic frameworks for gas storage and separation: Status and challenges. *EnergyChem*, **2019**, *1*, 100006.

9. J. Jiang and O.M. Yaghi. Brønsted acidity in metal–organic frameworks. *Chemical reviews*, **2015**, *115*, 6966.

10. P. Horcajada, et al. Porous metal–organic-framework nanoscale carriers as a potential platform for drug delivery and imaging. *Nature materials*, **2010**, *9*, 172.

11. L. Rani, et al. A critical review on recent developments in MOF adsorbents for the elimination of toxic heavy metals from aqueous solutions. *Environmental Science and Pollution Research*, **2020**, *27*, 44771.

12. H. Ghasempour and A. Morsali. Function–Topology Relationship in the Catalytic Hydrolysis of a Chemical Warfare Simulant in Two Zr-MOFs. *Chemistry–A European Journal*, **2020**, *26*, 17437.

13. M.J. Katz, et al. Simple and Compelling Biomimetic Metal–Organic Framework Catalyst for the Degradation of Nerve Agent Simulants. *Angew. Chem. Int. Ed.*, **2014**, *53*, 497.

© 2025 The Authors. This article is licensed under a Creative Commons Attribution 4.0 International License.

14. A. Michalkova and J. Leszczynski. Interactions of nerve agents with model surfaces: Computational approach. *Journal of Vacuum Science Technology A*, **2010**, *28*, 1010.

15. F.A. Son, et al. Uncovering the Role of Metal–Organic Framework Topology on the Capture and Reactivity of Chemical Warfare Agents. *Chemistry of Materials*, **2020**, *32*, 4609.

16. Y.-H. Huang, et al. Green and rapid synthesis of zirconium metal–organic frameworks via mechanochemistry: UiO-66 analog nanocrystals obtained in one hundred seconds. *Chemical Communications*, **2017**, *53*, 5818.

17. R. Puglisi, et al. Supramolecular recognition of a CWA simulant by metal–salen complexes: the first multi-topic approach. *Chemical Communications*, **2018**, *54*, 11156.

Graphical Abstract

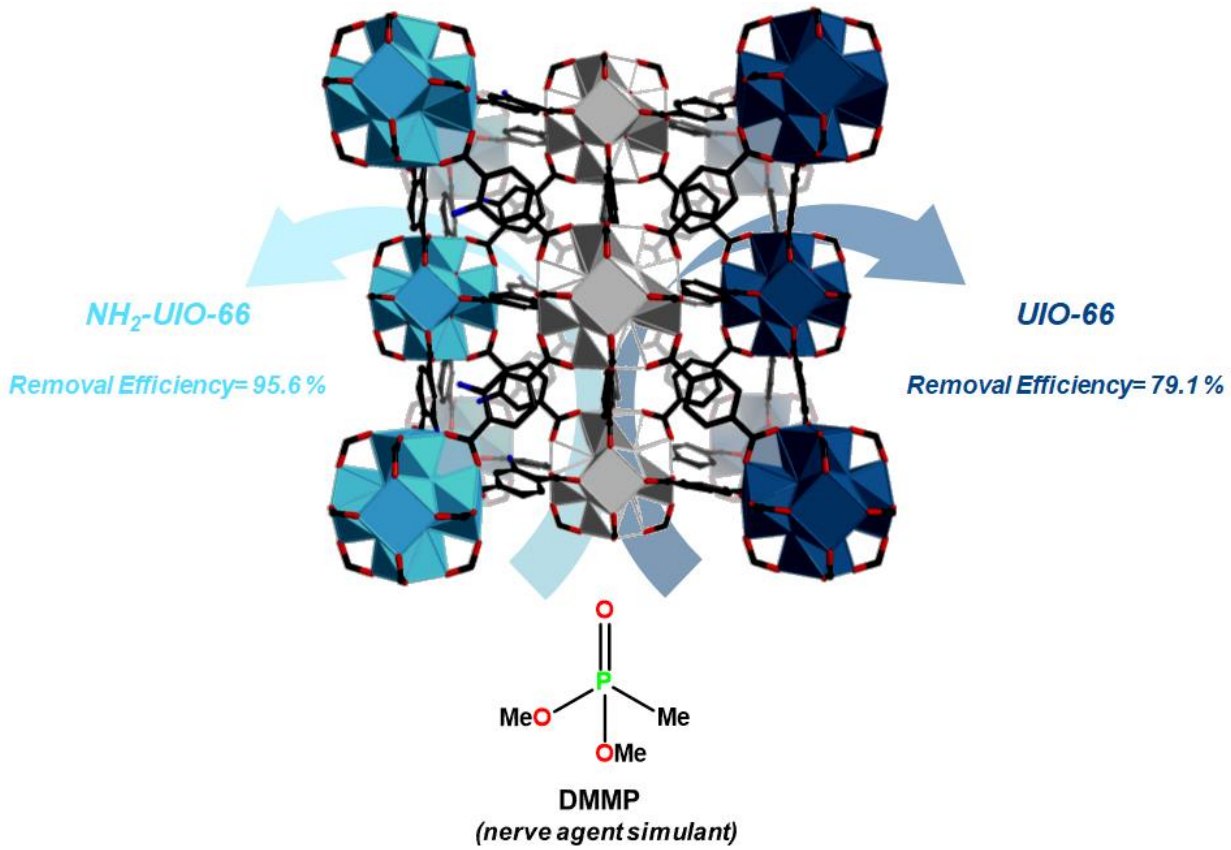

© 2025 The Authors. This article is licensed under a Creative Commons Attribution 4.0 International License.

Synthesis and Characterization of Novel Polyamide-imides Containing Thioether Linkages, Thiazole, and Nitrophenyl Units with High Solubility and Processability for Optical Film Applications

Aazam Jalali *

Department of Organic and Polymer Chemistry, Faculty of Chemistry, Kharazmi University, Tehran, Iran

Editor's note: Polyamide-imides (PAIs) are remarkable polymers that merge the beneficial properties of both polyamides and polyimides, making them suitable for various applications. Jalali synthesized a novel diimide-diacid monomer and utilized it to develop several sulfur-containing PAIs with high processability and solubility for optical film applications.

doi: 10.22034/jams.2025.210133

How to cite: A. Jalali. *Journal of Applied Material Science*, **2025**, *1*, 210133.

JOURNAL OF
APPLIED
MATERIAL
SCIENCE
jams.hsu.ac.ir

© 2025 *J. Appl. Mat. Sci.* This material is licensed under a Creative Commons Attribution 4.0 International License.

Journal of Applied Material Science **2025**, *1*, 210133
How to cite: A. Jalali, *Journal of Applied Material Science*, **2025**, *1*, 210133.
Journal homepage: **www.jams.hsu.ac.ir**

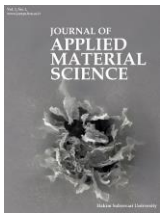

Original Research

Synthesis and Characterization of Novel Polyamide-imides Containing Thioether Linkages, Thiazole, and Nitrophenyl Units with High Solubility and Processability for Optical Film Applications

Aazam Jalali *

Department of Organic and Polymer Chemistry, Faculty of Chemistry, Kharazmi University, Tehran, Iran

Abstract

In this study, a novel diimide-diacid (DIDA) monomer featuring thiazole rings, nitrophenyl groups, and a thioether linkage has been introduced. Subsequently, several new sulfur-containing polyamide-imides (PAIs) were developed through the polycondensation reaction of DIDA with various aromatic diamines. This was achieved using a direct polycondensation method that employs triphenyl phosphite and pyridine. The resulting polymers were obtained in high yields, with inherent viscosities ranging from 0.73 to 0.92 dL/g. All synthesized polymers are amorphous and exhibit excellent solubility, easily dissolving in amide-type polar aprotic solvents such as *N*-methyl-2-pyrrolidone, dimethyl sulfoxide, *N*,*N*-dimethylacetamide, and dimethylformamide. Additionally, they can dissolve in less polar solvents like tetrahydrofuran, pyridine, and acetone. This solubility makes them promising candidates for the development of optical films, particularly given their confirmed high optical properties. The polymers also demonstrate good thermal stability, with a 10% weight loss occurring at temperatures ranging from 332.17 °C to 402.18 °C in a nitrogen atmosphere. Furthermore, the char yield of the synthesized polymers, defined as the percentage of solid residue remaining after heating from room temperature to 800 °C under nitrogen, ranges from 49.61% to 56.71%.

Keywords: Soluble polymer; Thioether linkage; Thiazole; Processible polymer; Polyamide-Imide.

1. Introduction

PAIs (Polyamide Imides) are high-performance polymers that combine the exceptional properties of both polyimides and polyamides. They exhibit excellent mechanical performance, outstanding thermal stability, and good processability [1]. Due to their high thermal stability, PAIs are promising candidates for various studies and industrial applications. For example, they are used to create coatings for optical fiber sensors in large-scale applications [2]. Compared to polyimides (PIs), PAIs have several advantages, including thermal and hydrolytic stability [2].

PAIs have a wide range of optical applications, ranging from protective coatings to flexible display devices [1-3]. PAIs and their nanocomposites have outstanding thermal

* Corresponding author.
Email address: aazamjalali@gmail.com (A. Jalali)

Received 23 January 2025
Revised 17 February 2025
Accepted 17 February 2025
Available online 18 February 2025

https://doi.org/10.22034/jams.2025.210133
© 2025 The Authors. This article is licensed under a Creative Commons Attribution 4.0 International License.

and mechanical properties [3], making them ideal for the development of protective coatings of optical fibers [2], thermally stable alternative materials for glass substrates [3], and flexible displays [4-6].

Sulfur-containing polymers, on the other hand, are unique polymers that have attracted significant interest in recent years [7, 8]. The incorporation of sulfur into the polymer backbone can improve thermal stability, mechanical properties, processability, solubility in common organic solvents, and flame resistance [9]. Several types of sulfur-containing polymers have been extensively studied, including poly(methacrylates) [10], epoxy resins [11], poly(arylene sulfide)s [12, 13], polyurethanes [14], polyamides (PAs) [15-18], PIs [19, 20], and thiol-containing cross-linked polymers [9].

Sulfur-containing PIs have high chemical and oxidative resistance, thermal stability, good mechanical properties, and inherently high refractive indices stemming, owing to their polarizable chains [21, 22]. However, despite their exceptional properties, most polyimides suffer from limitations such as poor solubility in common organic solvents, low processability due to high processing temperatures, deep colors, poor optical dispersion, and birefringence resulting from their rigid structures [23]. Consequently, extensive research has been conducted to improve the processability of polyimides while preserving their thermal stability [24, 25]. Strategies such as introducing flexible linkages, non-coplanar groups, bulky polar or non-polar pendant substituents, and heterocyclic units into the polymer backbone have attracted great research interest [26, 27]. In addition, copolymerization PAs and PIs can also lead to the synthesis of polymers that combine the beneficial properties of both polyamides and polyimides, as well as excellent thermal stability and good processability [1].

Thiazole ring as a sulfur-containing five-member hetero aromatic unit with one –C=N-C- bond, and a rigid structure has received considerable attention in academic studies and optoelectronic applications, with the preceding description introducing the thiazole ring into the polymer structure can improve the thermal stability, solubility of the polymer, processibility, and refractive index of polymer with increasing in sulfur content (Sc) while maintaining low molar volumes. Thiazole-containing polymers have widespread electrical and optical applications from this we can point to their application in transistors [28], polymer semiconductors [29, 30], electroluminescent devices [31], and non-linear optical (NLO) applications [32]. However, the design, synthesis, and properties study of high-refractive-index polymers (high-n) with thiazole units and high SC had not been done before our previous works [19, 33]. In these works, a new class of PAs and PAIs was introduced in which the monomers were designed with thioether bridges and thiazole units. The results demonstrate that the incorporation of both thiazole unit and thioether linkages resulted in organic-soluble and heat-resistant polymers [19, 33].

The solubility of polymers is directly affected by their chain structure. Replacing a hydrogen atom in the structure of a polymer with another group with higher polarity is a strategy to improve the solubility and processibility of polymers [34]. The nitro group has higher polarity than hydrogen and the replacement of one of the hydrogen atoms of the phenyl ring by this group in organic monomers can lead to a significant enhancement in the solubility and processibility of PAI polymers [34].

The present work introduces a novel DIDA monomer with thiazole ring, thioether-linkage, and nitrophenyl groups. Using this novel DIDA, a series of new PAIs is synthesized by polycondensation reaction of DIDA with aromatic diamines. The rigid thiazole units improved thermal stability. The bulky pendant nitrophenyl unit is expected to increase the processability and solubility of prepared polymers in conventional organic solvents concerning the reported analogous polymers containing phenyl groups [35]. Also, the flexible thioether linkage can improve the solubility and processability of synthesized polymer films by increasing the flexibility of the polymers. The structure-property relationships of the synthesized PAIs, such as the solubility, thermal resistance, inherent viscosity, moisture uptake, and morphological structure and crystallinity of the PAIs are also investigated in detail.

2. Experimental

2.1. Materials

5,5′-Thiobis(2-amino-4-nitrophenyl-thiazole) (DA) was synthesized following the established method described in the literature [36] and was subsequently recrystallized from a *N,N*-dimethylformamide (DMF, MERCK)/water mixture. Triphenyl phosphite (TPP, MERCK) and trimellitic anhydride (TMA, MERCK) were used

© 2025 The Authors. This article is licensed under a Creative Commons Attribution 4.0 International License.

without any additional purification. *N*-methyl-2-pyrrolidone (NMP, MERCK) and pyridine (Py, Fluka) were purified by distillation under reduced pressure over calcium hydride prior to use and were stored over 4 Å molecular sieves. Lithium chloride (LiCl, MERCK) was dried for 18 hours at 180°C under vacuum before its application. Both 1,4-phenylenediamine (MERCK) and 1,3-phenylenediamine (MERCK) were purified via vacuum sublimation. Additionally, 4,4′-oxydianiline (MERCK), 4,4′-diaminodiphenyl sulfone (MERCK), and 3,3′-diaminodiphenyl sulfone (MERCK) were purified by recrystallization from methanol. All other commercially available reagents and solvents were also used without further purification.

2.2. Monomer synthesis

For the synthesis of DIDA (Scheme 1), a 250-mL round-bottom flask was charged with a mixture of diacetylene (DA) (2.362 g, 5 mmol), trimethylamine (TMA) (1.921 g, 10 mmol), and glacial acetic acid (50 mL). The heterogeneous mixture was refluxed for 12 hours and subsequently allowed to cool to room temperature. The reaction mixture was then slowly transferred into 500 mL of water and the resulting precipitate was collected by filtration, boiled in methanol, and recrystallized from a solvent system of *N,N*-dimethylformamide (DMF)/water (v/v = 5:1). Finally, the product was dried under vacuum at 100°C for 24 hours, yielding a light-yellow solid.

Yield: 90%; melting point: 349-350°C; IR (KBr) 3400–2600 cm^{-1} (broad), 1792, 1732, 1703, 1529, 1346, 1296, 1227, 1169, 724, 695 cm^{-1}; ^1H NMR (300 MHz, DMSO-d6); δ 7.691–7.745 (t, 1H, J = 8.1 Hz), 8.025-8.051 (d, 1H, J = 7.8 Hz), 8.230- 8.273 (dd, 2H were overlapped), 8.301 (S), 8.376- 8.403 (d, 1H, J = 8.1 Hz), 8.625 (S), 13.5 (broad, 2H, C(O)O–H); ^{13}C NMR (75 MHz, DMSO-d6); δ 119.59, 124.90, 124.69, 128.02, 128.64, 128.92, 131.34, 132.33, 134.06, 136.29, 137.24, 153.99, 155.60, 163.24, 163.31, 165.61 ppm; Analysis calculated for $(C_{36}H_{16}N_6O_{12}S_3)n$: C, 52.68; H, 1.97; N,10.24. Found: C, 52.71; H, 2.00; N, 10.20.

2.3. Synthesis of polymers and film preparation

The polymerization reactions were carried out using the DIDA monomer and several aromatic diamines (1–5 in Scheme 2). The synthesis process for PAI-3 is detailed as follows: A mixture was prepared by combining 0.820 g (1 mmol) of DIDA, 0.108 g (1 mmol) of 4,4'-Diaminodiphenylsulfone, 0.3 g of LiCl, 0.6 mL of TPP, 0.5 mL of pyridine, and 3 mL of NMP in a suitable

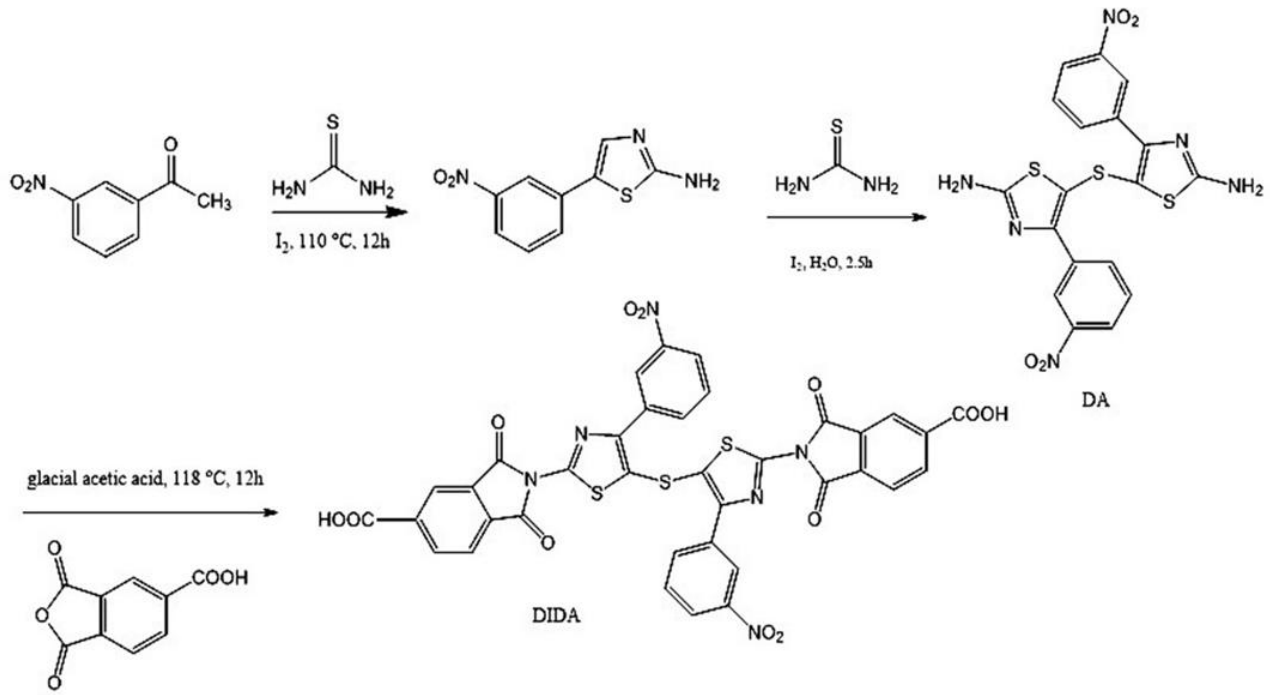

Scheme 1. Synthesis of DIDA.

© 2025 The Authors. This article is licensed under a Creative Commons Attribution 4.0 International License.

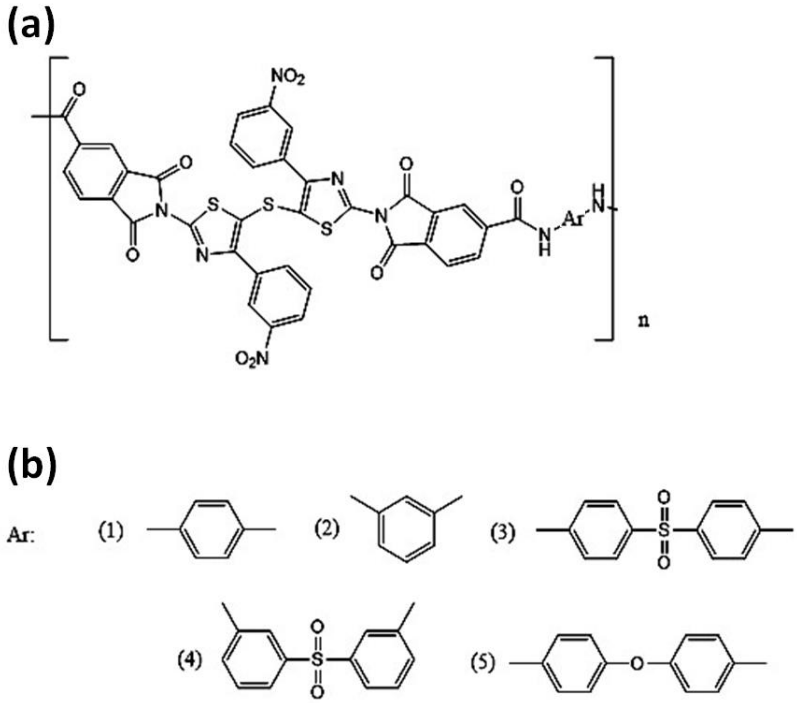

Scheme 2. (a) The general repeating unit of PAIs and (b) five aromatic diamines (labeled as Ar in panel a) used for the synthesis of different PAIs in this study.

round-bottom flask. This mixture was then reacted at 120 °C for 6 hours under a nitrogen atmosphere. During the polymerization, the viscosity of the mixture gradually increased and hence, 1 mL of NMP was added to the reaction mixture after 1 h. The resulting mixture was then slowly transferred into 200 mL of methanol while stirring vigorously. After filtration, the mixture was washed with 200 mL of hot water and 100 mL of methanol, then dried under vacuum at 100 °C overnight. For further purification, the polymer was dissolved in DMAc, the solution was filtered, and then the polymer was precipitated into methanol.

IR (KBr): 3358, 3099, 1791, 1729, 1683, 1591, 1532, 1496, 1400, 1435, 1350, 1321, 1255, 1182, 1152, 1107, 1075, 911, 837, 743, 722, 693, 594, 566 cm^{-1}. Elemental Analysis calculated for $(C_{48}H_{24}N_8O_{12}S_4)_n$: C, 55.76%; H, 2.44%; N, 10.84%. Found C, 55.64%; H, 2.62%; N, 10.70%.

2.4. Measurements

The ^{1}H-NMR (300 MHz) and ^{13}C-NMR (75 MHz) spectra were recorded on a Bruker DRX 300 AVANCE instrument at a temperature of 25 °C. Fourier transform infrared (FTIR) spectra were obtained using potassium bromide (KBr) pellets on a Perkin-Elmer FT Spectrum RX1, covering a range of 400–4000 cm^{-1}. Elemental analysis was performed with a Perkin-Elmer 2004 (II) CHN analyzer. Melting points (uncorrected) were measured via an Electrothermal Engineering LTD 9200 apparatus. Inherent viscosities (η_{inh} = ln ηr/c) were determined at a concentration of 0.5 g/dL using an Ubbelohde suspended-level viscometer at 30 °C, with *N,N*-dimethylacetamide (DMAc) as the solvent. Wide-angle X-ray diffraction (WAXD) measurements were taken at ambient temperature using a Philips PW 1800 diffractometer, equipped with graphite monochromatized Cu Kα radiation (λ = 1.5401 Å). The scanning rate was maintained at 0.08 °/s over a 2θ range of 4–80°. Thermogravimetric analyses (TGA) were conducted using a Du Pont 2000 thermal analyzer under a nitrogen atmosphere, with a heating rate of 10 °C/min.

3. Results and discussion

3.1. DIDA Monomer Characterization

The synthesis of a new DIDA monomer, which contains thiazole heteroaromatic rings, nitrophenyl groups, and a thioether linkage, is illustrated in Scheme

© 2025 The Authors. This article is licensed under a Creative Commons Attribution 4.0 International License.

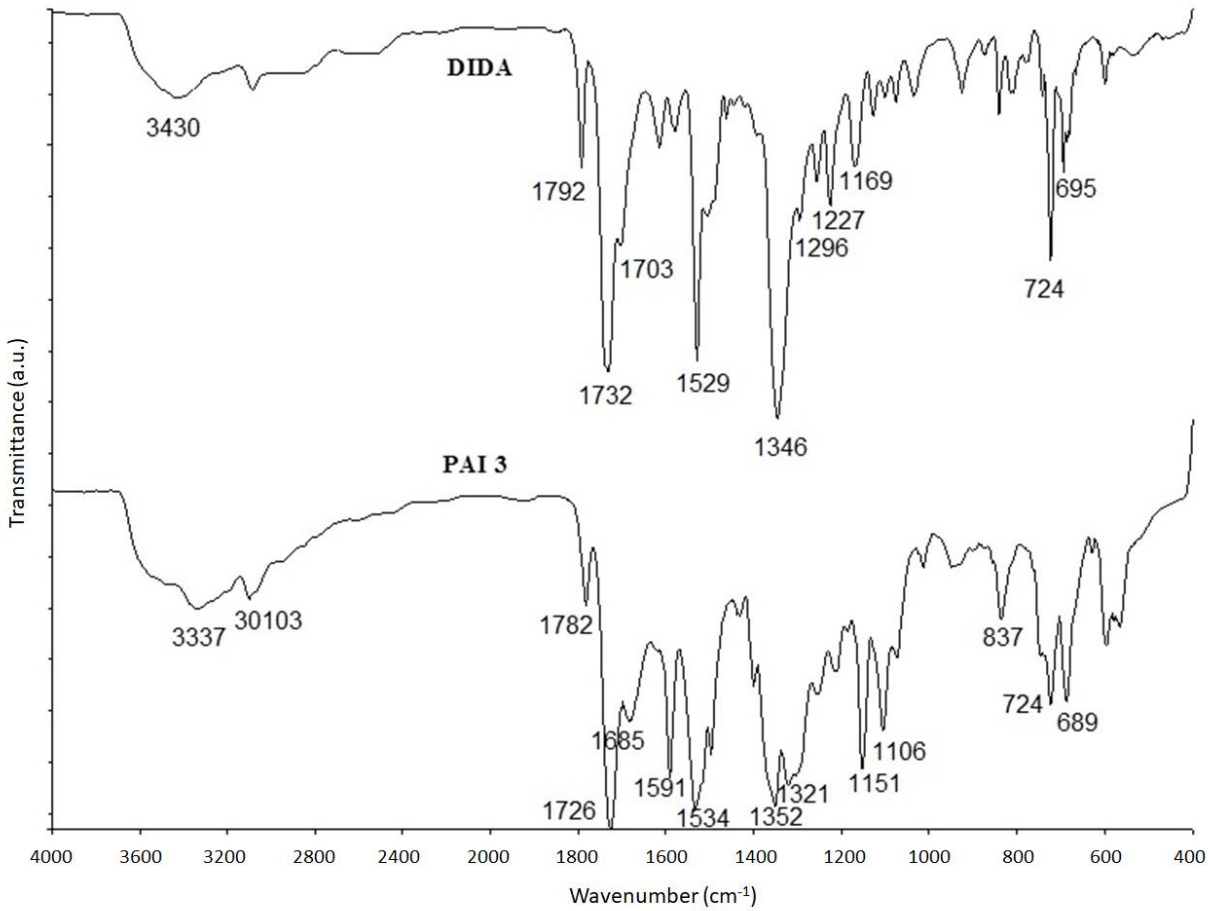

Figure 1. FTIR spectra of DIDA and PAI-3.

1. The DIDA was synthesized by polycondensation of DA with two-mole equivalents of TMA in refluxed glacial acetic acid. FTIR, ^{1}H-NMR, ^{13}CNMR, and elemental analysis confirmed the structure of the DIDA monomer. The FTIR spectrum of DIDA (Figure 1) displayed distinct spectral features indicative of carboxylic acid and cyclic imide functionalities. Notable absorption bands were observed in the range of 2400–3400 cm^{-1}, which correspond to C(O)O–H stretching vibrations. Additionally, peaks at 1792 cm^{-1} and 1732 cm^{-1} were observed, representing the asymmetrical and symmetrical C=O stretching vibrations of the imide group [37, 38]. Absorption bands at around 1346 cm^{-1} and 1529 cm^{-1} were also observed, corresponding to the symmetrical and asymmetrical stretching vibrations of nitro functionalities [39], confirming the presence of nitro substituents in the molecular structure of DIDA.

^{1}H- and ^{13}C-NMR spectra were also used to further confirm the successful synthesis of DIDA, as shown in Figures 2 and 3, respectively. In the ^{1}H-NMR spectrum of DIDA (Figure 2), downfield resonance signals at 8.025–8.051 ppm (d, J = 7.8 Hz), 8.301 ppm (s), and 8.376–8.402 ppm (d, J = 7.8 Hz) correspond to the protons of the trimellitimido moiety (c, a, and b protons in Figure 2b), supported by conjugation effects from the carboxylic acid and imide structure [19]. The nitrophenyl aromatic protons were detected at 7.691–7.745 ppm (f proton), 8.230–8.273 ppm (e and g protons), and 8.625 ppm (e proton).

The ^{13}C-NMR spectrum (Figure 3) revealed eighteen distinct carbon signals, consistent with the expected molecular structure. The carbonyl carbons of the carboxylic acid and imide groups resonate downfield at 172.00, 163.73, and 163.69 ppm. Elemental analysis

© 2025 The Authors. This article is licensed under a Creative Commons Attribution 4.0 International License.

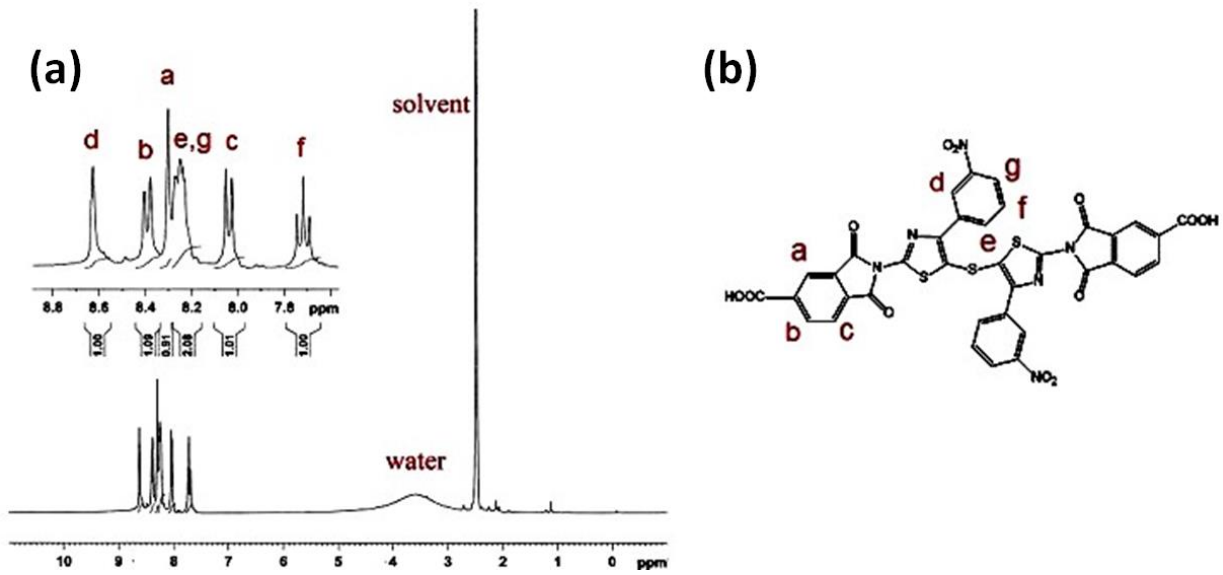

Figure 2. (a) The ^{1}H-NMR spectrum and (b) the proton assignments in the structure of synthesized DIDA.

results for DIDA also aligned with the calculated values for the proposed structure.

3.2. *Structural characterization of synthesized PAIs*

The Yamazaki-Higashi phosphorylation polycondensation method involves the reaction of aromatic diamines with aromatic dicarboxylic acids, utilizing TPP and Py as condensing agents. This classic technique has been widely used for preparing aromatic polyamides (PAs) on a laboratory scale [40]. One of the main advantages of this method over the diacid chloride preparation approach is that it avoids the boring work-up process and is less sensitive to moisture [41]. Additionally, it effectively synthesizes polymers with moderate to high degrees of polymerization. We have previously employed

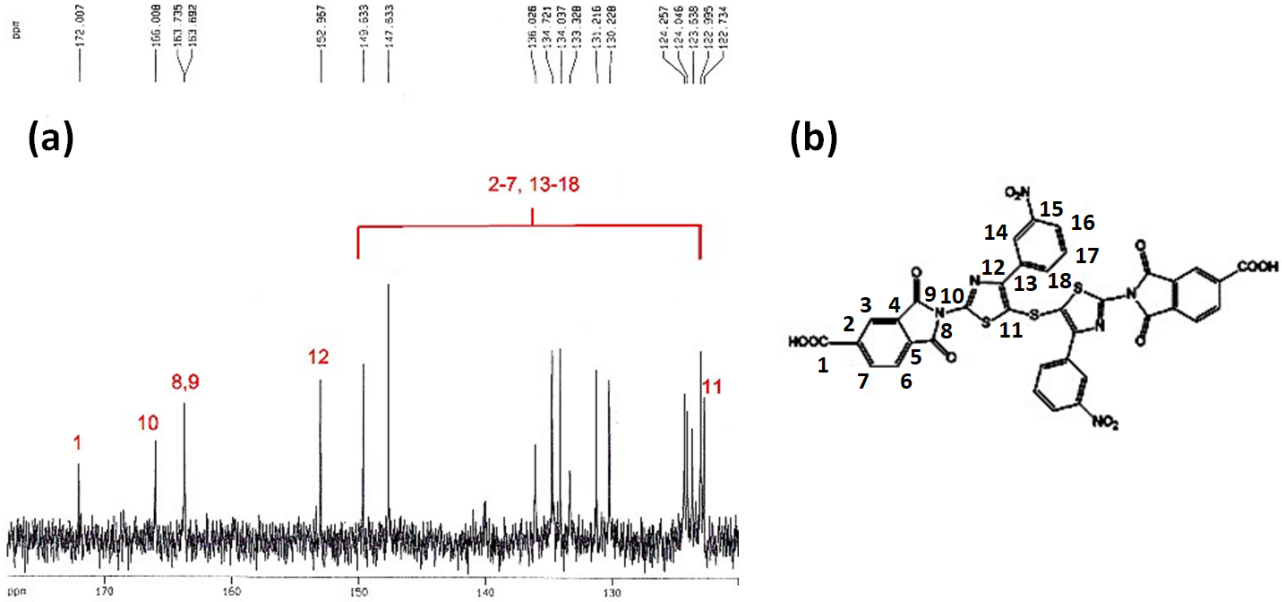

Figure 3. (a) The ^{13}C-NMR spectrum and (b) the carbon assignments in the structure of synthesized DIDA.

© 2025 The Authors. This article is licensed under a Creative Commons Attribution 4.0 International License.

Table 1. Synthetic conditions and inherent viscosities of PAIs

Polymer code	Amounts used			η_{inh} (dL/g)
	NMP (ml)	Py (ml)	LiCl (g)	
PAI-1	3+1	0.5	0.3	0.92
PAI-2	3	0.5	0.25	0.81
PAI-3	3+1	0.5	0.3	0.75
PAI-4	3	0.6	0.3	0.73
PAI-5	3	0.5	0.25	0.86

Notes: DIDA and diamine monomers= 1.0 mmol; TPP= 0.6mL; temperature= 120 °C; time= 6 h; 3+1: 3 mL initial and 1 mL additional.

this method in our research [19, 35], and the results demonstrated that these polymers exhibit excellent thermal stability, high refractive indices, and relatively good optical transparency.

In this study, a series of novel thiazole-containing PAIs with bulky pendant nitrophenyl groups and thioether linkages were synthesized using different functional groups (groups 1 to 5 for the synthesis of PA-1 to PA-5 in Scheme 2). All polycondensation reactions were carried out in freshly dried NMP, resulting in a homogeneous solution. The synthesis conditions and the inherent viscosities of the PAIs are reported in Table 1. The inherent viscosities of the polymers ranged from 0.73 to 0.92 dL/g, as measured in DMAc solutions.

The structural features of these PAIs were confirmed through elemental analysis, FTIR, and ^{1}H NMR spectroscopy. The results of the elemental analysis and moisture uptake of the PAIs are summarized in Table 2. Although the elemental analysis values generally aligned with the calculated values for the PAIs, the hygroscopic nature of the amide groups led to the observed carbon values being lower than those predicted for the proposed structures [42].

The FT-IR spectrum of PAI-3 revealed characteristic absorption bands associated with the imide ring and amide bonds, as shown in Figure 1. The imide ring shows stretching vibrations of the carbonyl groups at approximately 1780 cm^{-1} (asymmetric C=O stretching vibrations) and 1720 cm^{-1} (symmetric C=O stretching vibrations) [24, 37, 38]. Additionally, the C-N stretching vibrations are observed around 1380 cm^{-1}, while the imide ring deformation occurs at about 1092 cm^{-1} and 725 cm^{-1}. The amide group displays absorption peaks at around 3300 cm^{-1} (N-H stretching vibrations) and 1670 cm^{-1} (C=O stretching vibrations) [43]. These results confirm that the PAIs possess the expected chemical structures. Figure 4 illustrates a typical ^{1}H NMR spectrum for PAI-3, where all the proton signals align well with the proposed structure. A notable resonance peak appears in the downfield region at approximately 11.04 ppm, further supporting the formation of amide linkages.

Table 2. Elemental analysis and moisture uptake results of DIDA and PAIs

Sample code	Formula (Formula weight)		Elemental analysis (%)			Moisture uptake (%)
			C	H	N	
DIDA	$(C_{36}H_{16}N_6O_{12}S_3)_n$	Calculated	52.68	1.97	10.24	-
	(820.73)	Measured	52.71	2.00	10.20	
PAI-1	$(C_{42}H_{21}N_8O_{10}S_3)_n$	Calculated	56.44	2.37	12.54	1.40
	$(839.86)_n$	Measured	56.31	2.49	12.41	
PAI-2	$(C_{42}H_{21}N_8O_{10}S_3)_n$	Calculated	56.44	2.37	12.54	1.47
	$(839.86)_n$	Measured	56.35	2.53	12.43	
PAI-3	$(C_{48}H_{25}N_8O_{12}S_4)_n$	Calculated	55.76	2.44	10.84	1.5
	$(1034.01)_n$	Measured	55.61	2.56	10.69	
PAI-4	$(C_{48}H_{25}N_8O_{12}S_4)_n$	Calculated	55.76	2.44	10.84	1.68
	$(1034.01)_n$	Measured	55.72	2.55	10.72	
PAI-5	$(C_{48}H_{25}N_8O_{11}S_3)_n$	Calculated	58.47	2.56	11.37	1.38
	$(985.95)_n$	Measured	58.32	2.67	11.25	

Notes: Moisture uptake (%) = $[(W-W_0)/W_0] \times 100$; W and W_0 are the polymer weight after 72h at 25 °C and after drying at 100 °C for 12 h under vacuum, respectively.

© 2025 The Authors. This article is licensed under a Creative Commons Attribution 4.0 International License.

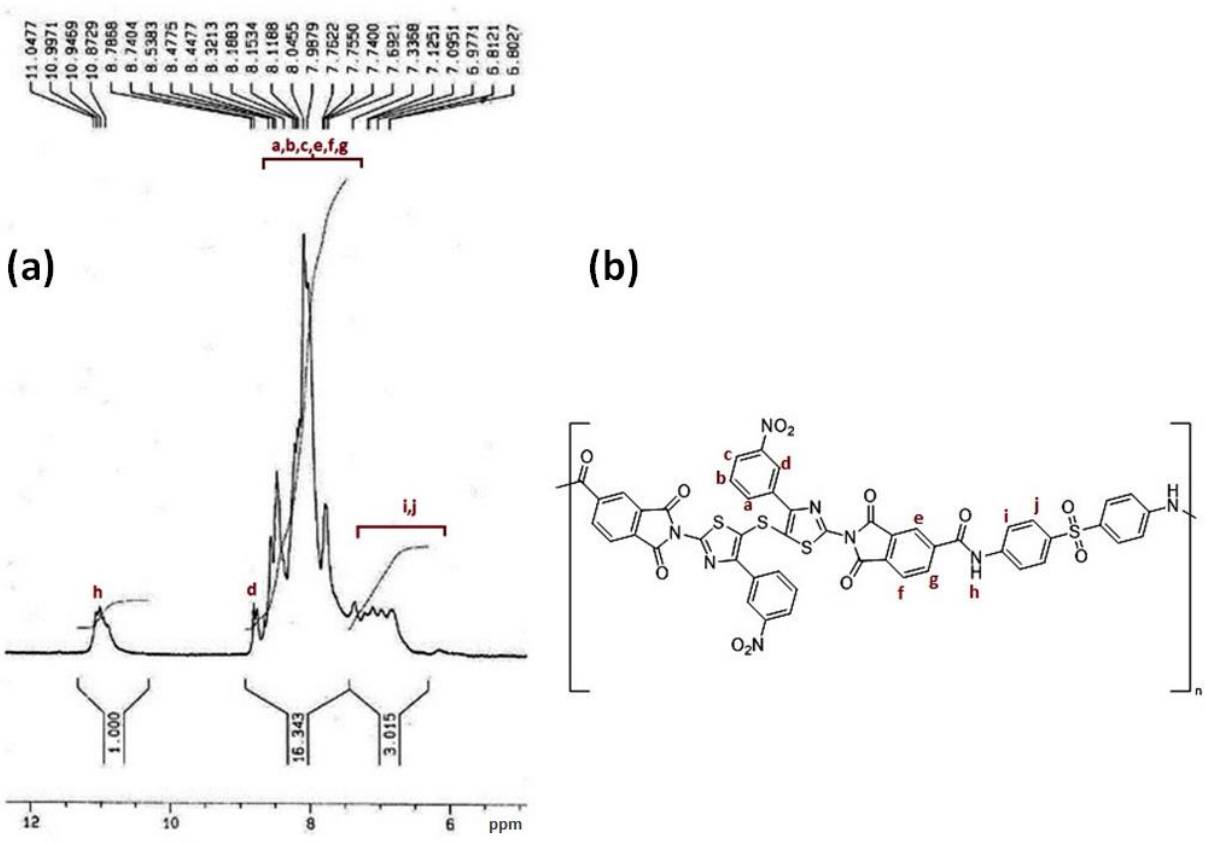

Figure 4. (a) The ^{1}H-NMR spectrum and (b) the proton assignments in the structure of the PAI-3 in DMSO-d6.

3.3. Solubility and microstructure of PAI films

The solubility of a polymer constitutes a critical determinant that influences its processability across various applications. Recently, several studies focused on the design and synthesis of polymers exhibiting a high refractive index, characterized by favorable solubility and processability, achieved through the incorporation of flexible thioether linkages within the polymer backbones [19, 33]. Furthermore, the incorporation of bulky moieties into either the polymer backbone or pendant groups can significantly enhance the solubility and processability of aromatic polyamides and polyimides, with a minimal decrease in thermal stability [19, 33].

The new DIDA monomer introduced in this work features thioether linkages and bulky pendant nitrophenyl rings. To assess the solubility of PAIs synthesized using this new DIDA, 0.05 g of each polymer was dissolved in 1 mL of various solvents, including N-methyl-2-pyrrolidone (NMP), dimethyl sulfoxide (DMSO), dimethylacetamide (DMAc), dimethylformamide (DMF), tetrahydrofuran (THF), pyridine, acetone, and chloroform at 25 °C for 24 h. As summarized in Table 3, all PAIs displayed excellent solubility in both moderately and highly polar solvents. The solubility varied based on the specific diamine used.

The presence of highly flexible ether linkages in the backbone of PAI-5, derived from 4,4′-oxydianiline, increased flexibility and disrupted the planarity of the aromatic units in this polymer. This alteration led to decreased close packing in the polymer chains. Consequently, PAI-5 was soluble not only in highly polar solvents like NMP, DMSO, DMAc, and DMF but also in moderately polar solvents such as acetone and chloroform when heated. In addition, a comparison with the solubility of PAIs containing methyl pendant groups was also reported in Table 3 [19, 35]. As observed in Table 3, PAIs with pendant nitrophenyl groups demonstrate better solubility compared to those with

© 2025 The Authors. This article is licensed under a Creative Commons Attribution 4.0 International License.

Table 3. Solubility of synthesized PAIs

Polymer code	Solvent							
	NMP	DMSO	DMAc	DMF	THF	Pyridine	Acetone	Chloroform
PAI-1	++ (+)	++ (+)	+ (+)	++ (+)	± (±)	±(-)	- (-)	- (-)
PAI-2	++ (++)	++ (+)	+ (+)	++ (+)	± (S)	±(±)	± (-)	- (-)
PAI-3	++ (++)	++ (+)	+ (+)	++ (+)	± (±)	±(±)	- (-)	- (-)
PAI-4	++ (++)	++ (+)	+ (+)	++ (+)	±(±)	++ (±)	± (-)	- (-)
PAI-5	++ (++)	++ (++)	++ (++)	++ (++)	++ (+)	++ (+)	+ (+)	+ (±)

Notes: (++) Soluble at room temperature (polymer concentration: 0.05 g/mL), (+) soluble after heating, (±) partially soluble, (S) swelling, (−) insoluble; Data in parentheses is those reported in the literature for PAIs containing methyl pendant groups [19]; NMP: *N*-methyl-2-pyrrolidone; DMF: *N,N*-dimethylformamide; DMAc: *N,N*-dimethylacetamide; DMSO: dimethyl sulfoxide; THF: tetrahydrofuran.

pendant methyl groups [19]. The bulky pendant Nitrophenyl groups disrupted the regularity and close packing of polymer chains.

The morphological structure and crystallinity of the synthesized PAI-1 were assessed using WAXD, as shown in Figure 5. PAI-1. The crystalline structure affects the refractive index and birefringence of the polymers applicable in optical industries and acts as a defect interrupting the guiding light [44, 45]. The diffractogram of the PAI-1 revealed a broad halo between 2θ = 15° and 25°, with no distinct peak features, indicating that the synthesized polymer is fully amorphous. This amorphous nature can be attributed to the presence of pendant nitrophenyl groups in the polymer backbone, which reduces the symmetry and regularity of the backbone. This reduction weakens the intermolecular forces, such as hydrogen bonding between the polymer chains, thereby hindering chain packing efficiency. As a result, the intermolecular forces diminish, leading to lower crystallinity. The excellent solubility in organic solvents and favorable film-forming properties of these PAIs contribute to their amorphous structure.

3.4. Thermal properties of synthesized PAIs

The thermal and thermo-oxidative stabilities of the polymers were evaluated using thermogravimetric analysis (TGA) under a nitrogen atmosphere, as shown in Figure 6. One of the key metrics for assessing the thermal stability of the polymers is the temperature of 10 wt.% loss occurs (T_{10}). Moreover, char yield can provide important information on the structure of polymers. These two thermal characteristics were extracted from Figure 6 and summarized in Table 4. All synthesized

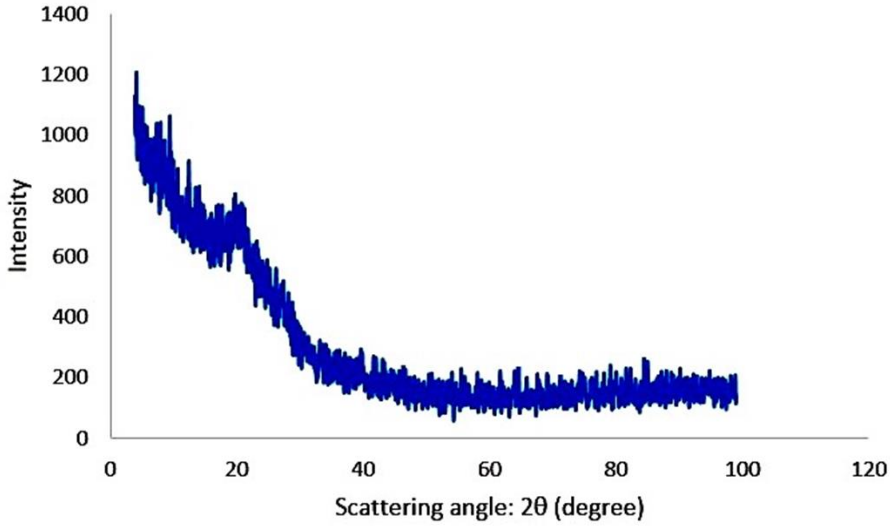

Figure 5. WAXD pattern of PAI-1.

© 2025 The Authors. This article is licensed under a Creative Commons Attribution 4.0 International License.

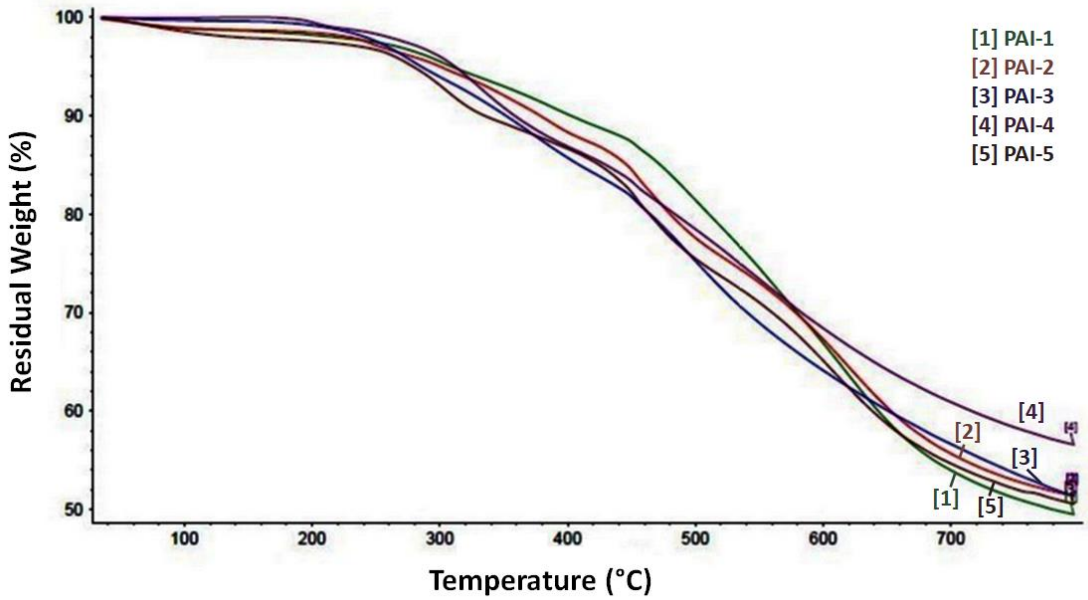

Figure 6. TGA results of the synthesized PAIs (heating rate: 10 °C/min under N_2).

PAIs demonstrated good thermal stability, exhibiting no significant weight loss below 330 °C. The T_{10} values for the PAIs ranged from 332 to 402 °C in nitrogen. Additionally, the residual weight of all the PAIs at 800 °C under N_2 was greater than 49%. As anticipated, these polymers maintained excellent thermal stability, even with the incorporation of flexible thioether linkages and pendant nitro phenyl groups, enabling them to withstand elevated processing temperatures.

Table 4. The thermal stability results of synthesized PAIs

Polymer	T_{10} (°C)	Char Yield at 800 °C (%)
PAI-1	402.18	49.61
PAI-2	372.01	51.49
PAI-3	342.06	51.51
PAI-4	351.98	56.71
PAI-5	332.17	50.68

4. Conclusions

In this study, a new non-coplanar DIDA monomer featuring bulky nitrobenzene rings and thiazole groups linked by thioether was synthesized and polymerized with various aromatic diamines to produce a series of sulfur-containing PAIs. As anticipated, the combined effects of the non-coplanar structure, nitro units, and flexible thioether bridges in the DIDA monomer contributed to the good solubility of the resulting PAIs in a range of organic solvents. These polymers exhibited high thermal and thermo-oxidative stability. Analysis of X-ray diffractograms and solubility data suggests that the non-coplanar structure and flexible linkages prevent the polyamide-imide chains from packing closely together, giving the polymers an amorphous nature and enhancing their solubility. Synthesized polymers can be used in the fabrication of high-performance optical films for various applications.

Acknowledgments

The author would like to greatly appreciate the Kharazmi University for the support of this work.

Conflict of Interest

The author declares no conflict of interest.

References

1. H. Toiserkani. Poly (amide-imide)/modified-TiO2 nanocomposites containing laterally-attached benzimidazole

© 2025 The Authors. This article is licensed under a Creative Commons Attribution 4.0 International License.

moieties: preparation, morphological, and thermal characterization. *Composite Interfaces*, **2023**, *30*, 187.

2. O.N. Zabegaeva, et al. Polyamide-imides as novel high performance primary protective coatings of silica optical fibers: Influence of the structure and molecular weight. *Reactive and Functional Polymers*, **2024**, *194*, 105775.

3. S.A. Ansari and N.G. Shimpi. Preparation of polyamide-imide: ZnO nanocomposites (PAI: ZnO nanocomposites): its characterization, limiting oxygen index, and antibacterial investigation. *Polymer Bulletin*, **2024**, *81*, 14587.

4. L. Yang, et al. High Tg, Low CTE Transparent Poly (Amide-Imide) s Based on Synergistic Regulation of Lithium Ions Coordination and Ortho-Position Effect of 9, 9-Bis (4-Aminophenyl) Fluorene. *Journal of Polymer Science*, *63*, 974.

5. Y.-Y. Liu, et al. Colorless Polyamide–Imide films with tunable coefficient of thermal expansion and their application in flexible display devices. *Polymer*, **2024**, *294*, 126712.

6. G. Zhu, et al. Synthesis and characterization of high Tg and colorless polyamide-imide films derived from amide-containing diamines with different trifluoromethyl substitution. *Polymer*, **2024**, *302*, 127033.

7. D.-F. Hong, et al. A sulfur-containing Cd (II) coordination polymer assembled from 4-(4-pyridinyl) thiazole-2-thiol: synthesis, crystal structure, properties, and Hirshfeld surface analysis. *Journal of Sulfur Chemistry*, **2025**, *46*, 80.

8. S. Yang and Q. Sun. Sulfur-containing polymers for enhancing rate and cycle performance of lithium-sulfur batteries. *Journal of Industrial and Engineering Chemistry*, **2025**, *143*, 144.

9. K. Mazumder, B. Voit, and S. Banerjee. Recent Progress in Sulfur-Containing High Refractive Index Polymers for Optical Applications. *ACS omega*, **2024**, *9*, 6253.

10. R. Okutsu, S. Ando, and M. Ueda. Sulfur-containing poly (meth) acrylates with high refractive indices and high Abbe's numbers. *Chemistry of Materials*, **2008**, *20*, 4017.

11. C. Lü, et al. Studies on syntheses and properties of episulfide-type optical resins with high refractive index. *Journal of applied polymer science*, **2003**, *89*, 2426.

12. M.J. Robb and D.M. Knauss. Poly(arylene sulfide)s by nucleophilic aromatic substitution polymerization of 2, 7-difluorothianthrene. *Journal of Polymer Science Part A: Polymer Chemistry*, **2009**, *47*, 2453.

13. Y. Nakagawa, et al. Synthesis of highly refractive poly (phenylene thioether) derived from 2, 4-dichloro-6-alkylthio-1, 3, 5-triazines and aromatic dithiols. *Macromolecules*, **2011**, *44*, 9180.

14. T. Matsuda, et al. Optical material of high refractive index resin composed of sulfur-containing aliphatic and alicyclic methacrylates. *Journal of applied polymer science*, **2000**, *76*, 45.

15. G. Zhang, et al. Synthesis of high refractive index polyamides containing thioether unit. *Journal of Polymer Research*, **2011**, *18*, 1261.

16. G. Zhang, et al. Synthesis of high refractive index polyamides containing thio-ether units. *Journal of Macromolecular Science, Part A: Pure and Applied Chemistry*, **2010**, *47*, 892.

17. G. Zhang, et al. Synthesis and properties of polyamides containing high contents of thioether units. *Reactive and Functional Polymers*, **2011**, *71*, 775.

18. G. Zhang, et al. Synthesis and properties of polyamides derived from 4, 6-bis (4-chloroformylphenylthio) pyrimidine and 3, 6-bis (4-chloroformylphenylthio) pyridazine. *Polymer International*, **2013**, *62*, 1358.

19. A. Shockravi, et al. Highly refractive and organo-soluble poly (amide imide) s based on 5, 5′-thiobis (2-amino-4-methyl-thiazole): Synthesis and characterization. *Journal of applied polymer science*, **2012**, *125*, 1521.

20. Z. Li, J.-G. Liu, and S.-Y. Yang. Synthesis and characterization of thioether and pyridine-bridged aromatic polyimides with high refractive indices and high glass transition temperatures. *High Performance Polymers*, **2009**, *22*, 468.

21. J.M. García, et al. High-performance aromatic polyamides. *Progress in polymer science*, **2010**, *35*, 623.

22. D.-J. Liaw, et al. Advanced polyimide materials: Syntheses, physical properties and applications. *Progress in Polymer Science*, **2012**, *37*, 907.

23. Y.Y. Liu, Y.K. Wang, and D.Y. Wu. Synthetic strategies for highly transparent and colorless polyimide film. *Journal of Applied Polymer Science*, **2022**, *139*, e52604.

24. G. Huang, et al. Acyloxy-Containing Fluorene-and Benzimidazole-Based Polyimides with Improved Solubility, Transparency, and Dielectric Properties by Postmodification. *ACS Applied Polymer Materials*, **2025**, *7*, 1522.

25. J. Park, R.M. Muthoka, and Y. Lee. Designing Thermally Resistant Polyimide Oligomers: Insights from Molecular Dynamics Simulations. *Macromolecules*, **2025**. https://doi.org/10.1021/acs.macromol.4c02181.

26. X. Wang, et al. Synthesis and characterization of novel polyimides derived from pyridine-bridged aromatic dianhydride and various diamines. *European polymer journal*, **2006**, *42*, 1229.

27. X. Zhao, et al. Synthesis and characterization of novel polyimides derived from 2-amino-5-[4-(4′-aminophenoxy) phenyl]-thiazole with some of dianhydride monomers. *Polymer*, **2007**, *48*, 5241.

28. I. Osaka, et al. Novel Thiophene-Thiazolothiazole Copolymers for Organic Field-Effect Transistors. *Advanced Materials*, **2007**, *19*, 4160.

© 2025 The Authors. This article is licensed under a Creative Commons Attribution 4.0 International License.

29. B. Kang, et al. π-Extended Thiazole-Containing Polymer Semiconductor for Balanced Charge–Carrier Mobilities. *Macromolecular Rapid Communications*, **2021**, *42*, 2000741.

30. T. Shen, et al. Rational molecular design of diketopyrrolopyrrole-based n-type and ambipolar polymer semiconductors. *Chemistry–A European Journal*, **2024**, *30*, e202401812.

31. I.H. Jung, et al. Synthesis and electroluminescent properties of fluorene-based copolymers containing electron-withdrawing thiazole derivatives. *Journal of Polymer Science Part A: Polymer Chemistry*, **2008**, *46*, 7148.

32. M. He, et al. The synthesis and optical properties of novel fluorinated polyimides incorporated with highly electro-optic active thiazole and benzothiazole based chromophores. *Dyes and Pigments*, **2010**, *86*, 107.

33. A. Javadi, et al. Solution processable polyamides containing thiazole units and thioether linkages with high optical transparency, high refractive index, and low birefringence. *Journal of Polymer Science Part A: Polymer Chemistry*, **2013**, *51*, 3505.

34. J.A. Dean, *Lange's Handbook of Chemistry*. 15 ed. **1998**: McGraw-Hill Companies.

35. A. Javadi, et al. Synthesis and structure–property relationships of novel thiazole-containing poly (amide imide) s with high refractive indices and low birefringences. *polymer international*, **2015**, *64*, 486.

36. R.G. Woodbridge and G. Dougherty. A novel sulfidation reaction and its application to some 4-substituted-2-aminothiazoles. *Journal of the American Chemical Society*, **1949**, *71*, 1744.

37. H. Kim, et al. Fluorescence behaviors of perylene-dispersed super engineering plastic films. *Polymer*, **2024**, *303*, 127147.

38. M.H. Kabir, et al. Plasticization-and Aging-Resistant Phenolphthalein-Based Thermally Cross-Linked PIM Polyimide Membranes for Efficient CO2 Separation. *ACS Applied Polymer Materials*, **2024**, *7*, 319.

39. R.B. Alnoman, et al. Post-crosslinked amino-functionalized molecularly imprinted polymers via click chemistry for selective chiral recognition of S-etodolac. *Microchemical Journal*, **2025**, *210*, 112983.

40. G. Maier. Low dielectric constant polymers for microelectronics. *Progress in polymer science*, **2001**, *26*, 3.

41. N. Yamazaki, M. Matsumoto, and F. Higashi. Studies on reactions of the N-phosphonium salts of pyridines. XIV. Wholly aromatic polyamides by the direct polycondensation reaction by using phosphites in the presence of metal salts. *Journal of Polymer Science: Polymer Chemistry Edition*, **1975**, *13*, 1373.

42. D.J. Liaw and B.Y. Liaw. Synthesis and characterization of new poly (amide–imide) s from 1, 4-bis (4-trimellitimidophenoxy)-2-tert-butylbenzene with various diamines. *Journal of Polymer Science Part A: Polymer Chemistry*, **1998**, *36*, 2301.

43. S.J. Kim, et al. Transparent Poly(amide-imide)s with Low Coefficient of Thermal Expansion from Trifluoromethylated Trimellitic Anhydride. *Polymers*, **2025**, *17*, 309.

44. N.-H. You, et al. Synthesis of high refractive index polyimides derived from 1, 6-bis (p-aminophenylsulfanyl)-3, 4, 8, 9-tetrahydro-2, 5, 7, 10-tetrathiaanthracene and aromatic dianhydrides. *Macromolecules*, **2008**, *41*, 6361.

45. N.-H. You, et al. Synthesis and characterization of highly refractive polyimides derived from 2, 7-bis (4′-aminophenylenesulfanyl) thianthrene-5, 5, 10, 10-tetraoxide and aromatic dianhydrides. *Polymer*, **2009**, *50*, 789.

© 2025 The Authors. This article is licensed under a Creative Commons Attribution 4.0 International License.

From Waste Polypropylene to Carbon Dots

Faezeh Mahdavian, Haleh Naeim, Denis Rodrigue *

Department of Chemical Engineering, Université Laval, Quebec City, QC, G1V 0A6, Canada

Editor's note: Converting plastics into advanced nanomaterials is an effective recycling strategy that addresses the growing problem of polymer waste, making it crucial for environmental sustainability. Mahdavian et al. introduced a two-step method to convert polypropylene waste from food packaging into carbon dots, which can be utilized in bioimaging, energy conversion, and sensing applications.

doi: 10.22034/jams.2025.210134

How to cite: F. Mahdavian et al. *Journal of Applied Material Science*, **2025**, *1*, 210134.

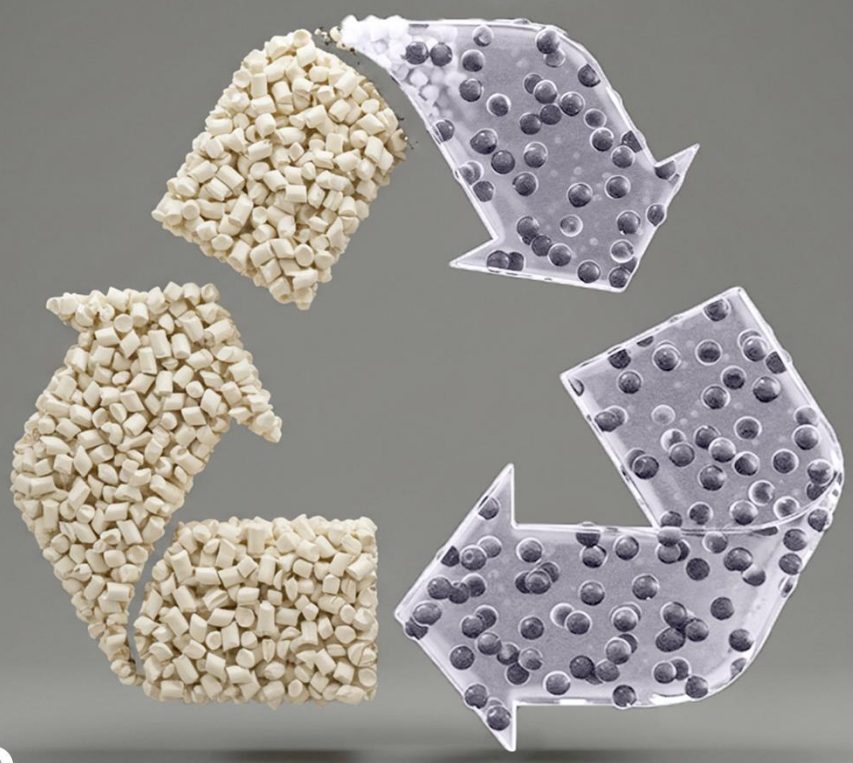

JOURNAL OF
APPLIED
MATERIAL
SCIENCE
jams.hsu.ac.ir

© 2025 *J. Appl. Mat. Sci.* This material is licensed under a Creative Commons Attribution 4.0 International License.

Journal of Applied Material Science **2025**, *1*, 210134
How to cite: F. Mahdavian et al., *Journal of Applied Material Science*, **2025**, *1*, 210134.
Journal homepage: **www.jams.hsu.ac.ir**

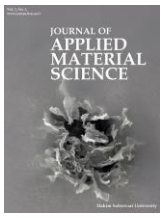

Original Research

From Waste Polypropylene to Carbon Dots

Faezeh Mahdavian, Haleh Naeim, Denis Rodrigue *

Department of Chemical Engineering, Université Laval, Quebec City, QC, G1V 0A6, Canada

Abstract

This study presents the successful synthesis of carbon dots (C-Dots) from polypropylene (PP) from a two-step method. PP waste from food packaging was converted into C-Dots through a thermal process followed by a solvothermal approach. Thermal analysis of PP waste provided insights into its stability, decomposition, and phase transitions, optimizing its use as the precursor for C-Dots synthesis and impurity identification. FTIR analysis confirmed the presence of oxygen-containing functional groups in the PP-derived C-Dots, highlighting the successful conversion of polymeric waste into a high-value material. The formation of C-Dots nanoparticles was further confirmed via transmission electron microscopy analysis. The particles were characterized by an average size of 43 nm and a standard deviation (SD) of 17 nm. Additionally, the combination of strong UV absorption and a narrow band gap absorption highlights the unique electronic properties of these C-Dots, making them suitable and sustainable candidates for applications such as bioimaging, energy conversion, and sensing.

Keywords: Polypropylene; Waste management; Recycling; Carbon dots.

1. Introduction

Polymers serve as fundamental components in modern life because of their remarkable versatility, durability, and extensive applicability across diverse industrial sectors. However, it is imperative to address the significant drawbacks associated with polymers, especially about sustainability and environmental issues [1]. Minimizing environmental impact, reducing carbon footprints, and decreasing residual wastes are key strategies in polymer waste management [1, 2]. This is why polymer recycling represents a sustainable approach that not only decreases energy consumption compared to the production of virgin polymers, but also substantially reduces greenhouse gas (GHG) emissions, contributing to cleaner and more environmentally friendly manufacturing processes [2].

Recent advancements in recycling technologies catalyzed the development of a variety of innovative techniques for the sustainable management of polymer waste [3]. One of them is mechanical recycling which includes the physical reprocessing of polymers into new materials without changing their chemical structure, making it a straightforward and widely used method [4]. In contrast, chemical recycling involves the depolymerization of macromolecules into their constituent monomers or other fundamental components, enabling the production of high-quality, new polymers

* Corresponding author.
Email address: denis.rodrigue@gch.ulaval.ca (D. Rodrigue)

Received 4 February 2025
Revised 18 February 2025
Accepted 19 February 2025
Available online 20 February 2025

https://doi.org/10.22034/jams.2025.210134
© 2025 The Authors. This article is licensed under a Creative Commons Attribution 4.0 International License.

with properties close to virgin materials [5]. Another objective is upcycling which transforms waste polymers into high-value and functional products offering a creative and sustainable approach to polymer reuse [6].

Efforts to upcycle (added-value) plastic waste into lubricants, biofuels, construction materials, and combustible gases often led to inconsistencies, thereby limiting their scalability. The development of a cost-effective methodology for polymer wastes into carbon dots (C-Dots) represents a viable solution to these challenges, enabling the generation of high-value products while concurrently mitigating waste accumulation [7]. Unlike conventional recycling, which often yields lower-grade materials, this approach significantly improves the value of waste polymers. This method offers an innovative and sustainable solution to manage polymer wastes by converting them into non-toxic functional nanomaterials rather than conventional downcycling (fillers) or disposal (landfilling). Moreover, it aligns with sustainable chemistry and materials science principles, contributing to waste reduction and promoting a circular economy. Thus, C-Dots synthesis from waste polymers is in line with green chemistry principles by minimizing waste generation and the optimization of resource efficiency, showcasing a practical and environmentally responsible strategy to address the challenges associated with polymer waste management [8].

The synthesis of C-Dots can be divided into two main approaches: "top-down" and "bottom-up". The top-down technique involves breaking down larger carbon structures into nanoscale materials using methods such as laser ablation, arc discharge, high-energy ball milling, and electrochemical techniques [9, 10]. On the other hand, the bottom-up approach involves synthesizing C-Dots from small organic precursors or polymers through processes such as thermal decomposition, microwave pyrolysis, plasma treatment, and hydrothermal oxidation [11]. Initially, C-Dots synthesis used energy-intensive top-down methods with graphite, carbon nanotubes, or graphene, while more recent strategies use organic molecules or carbon-rich polymers as precursors, requiring less energy [12].

One of the most efficient methods to synthesize C-Dots involves thermal decomposition processes of carbon-rich raw materials at elevated temperatures. For example, Aji et al. studied the synthesis of C-Dots from polypropylene (PP) wastes by heating at 200, 250, and 300 °C for 20 min. Their findings highlighted the significant effect of temperature on C-Dots formation, where higher temperatures led to higher carbon chain rupture and the formation of smaller particles with higher energy levels. The polymerization of carbon chains during the heating process resulted in the creation of new functional groups, a confirmation of the temperature-dependent evolution of C-Dots' structure and properties [13]. This approach offers several advantages, including high yield, cost-effectiveness, shorter reaction times, broader raw material compatibility, and more straightforward syntheses [10].

Since most of the plastics today are derived from carbon, this makes them suitable precursors for the synthesis of C-Dots with precise and tunable properties [10, 14]. The conversion of waste polymers based on polylactide (PLA) [15], polyethylene terephthalate (PET) [16], polystyrene (PS) [17], and polypropylene (PP) [13] into high-value C-Dots nanomaterials represents an advanced form of upcycling for different polymer waste management approaches [18]. In particular, PP gained attention as a precursor to synthesize C-Dots due to its widespread availability, low cost, and high thermal stability [19].

Unlike most polymers, such as polyethylene (PE) or PS, PP has a relatively higher melting point (around 160 °C) and a stable carbon backbone, making it suitable for high-temperature carbonization processes [20-22]. Studies on PP as a precursor also showed promising results of 10.3% C-Dot yield and optical properties like UV-Vis absorption and fluorescence emission for catalyst-free methods [7, 12, 13]. However, compared to more commonly used polymers such as PET, which has been widely explored for C-Dot synthesis due to its higher aromatic content [16], PP's lack of aromaticity may influence the size and surface functionality of the resulting C-Dots. In contrast, polymers such as PS, which are rich in aromatic rings, tend to form C-Dots with high photoluminescence (PL) quantum yield (around 20%), but often require harsher conditions (high temperature), or the use of surface passivating agents such as ethylenediamine, to achieve high yields [23].

Although PP is a promising precursor for sustainable C-Dot production, it may not offer the same optical properties or ease of synthesis as more aromatic polymers. Nonetheless, its use in C-Dot synthesis from waste plastics presents significant advantages in terms of cost-effectiveness and scalability for commercial

© 2025 The Authors. This article is licensed under a Creative Commons Attribution 4.0 International License.

applications. Thus, recycling PP wastes into polymer-based carbon nanomaterials represents an opportunity to use waste materials for high-value and cutting-edge applications. These C-Dots exhibit remarkable versatility, making them promising candidates for several advanced technological fields including photocatalytic materials, water treatment [24], bioimaging agents, energy storage [25], and sensors [26, 27].

Although a growing interest in the synthesis of C-Dots from plastic waste was observed, the number of studies remains limited, often relying on microwave heating or the introduction of catalysts (metals, acids, and bases) leading to difficult scalability [10, 28]. This is why the catalyst-free production of C-Dots from available precursors offers a promising step toward sustainability [15]. This study highlights the critical role of waste management in reducing environmental pollution, while creating new opportunities for technological advancements by the transformation of PP wastes into valuable C-Dot nanomaterials. Beyond their technical applications, the results of this study hold broader implications for environmental sustainability. By providing an innovative and scalable approach to PP recycling, this work addresses one of the most pressing environmental challenges of our time: the accumulation of non-biodegradable plastic waste. The successful transformation of plastic residues into valuable polymer C-Dots represents a practical and impactful strategy to mitigate environmental pollution. Moreover, this approach highlights the promising potential of waste recycling, turning discarded materials into functional resources, thereby contributing to a circular economy and advancing global efforts toward environmental protection and conservation.

2. Experimental

2.1. *Materials*

The recycled polypropylene (PP) was obtained from bags daily used in food-related applications (Figure 1). Ethanol was purchased from Greenfield Global Inc. (Canada) and sodium hydroxide (NaOH) was obtained from Fisher BioReagents (USA).

2.2. *Carbon Dots preparation*

A step-by-step scheme of C-Dots production is shown in Figure 1. The PP bags were first cleaned by soaking

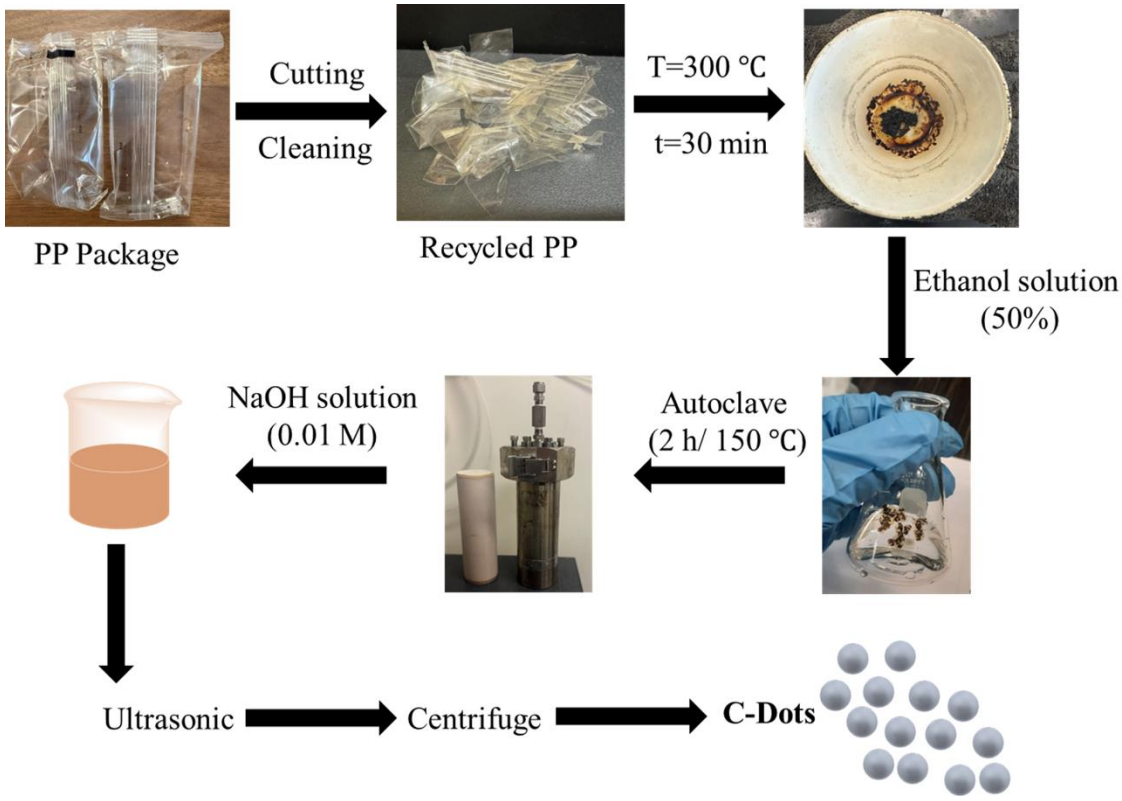

Figure 1. Steps leading to the preparation of C-Dots preparation from waste PP.

© 2025 The Authors. This article is licensed under a Creative Commons Attribution 4.0 International License.

them in warm water containing a small amount of liquid soap for a short period. It was then thoroughly rinsed with clean water to remove the detergent and any remaining contaminants. Following this step, the PP was rinsed with distilled water and dried at room temperature, then cut into parts having smaller dimensions. They were then heated in an oven at 300 °C for 30 min. The resulting dark brown solid was added to a 50% ethanol solution and stirred continuously for 2 h. Then, the material was transferred to a 450 ml Teflon-lined autoclave and heated for 2 h at 150 °C. Upon cooling to room temperature, 0.1 M NaOH was added to the solution while stirring. Then, the particles were dispersed and the solution was homogenized using an ultrasonic water bath (model 75T, VWR Scientific Products, USA) for 2 h. Finally, the solution containing C-Dots was carefully extracted from the upper layer following centrifugation at 4000 rpm for 30 min. An ultrasonic cleaning process was performed using a VWR Scientific Products Aquasonic Ultrasonic Cleaner Water Bath (model: 75T).

2.3. Measurements

Thermogravimetric analysis (TGA) was performed on a Q5000 IR (TA Instruments, USA) with a heating ramp of 10 °C/min from room temperature to 850 °C under air. To confirm the composition of the recycled material, differential scanning calorimetry (DSC) analysis was carried out using a Discovery DSC 25 (TA Instruments, USA). The analysis involved a single heating and cooling cycle over a temperature range of 0 °C to 250 °C under a nitrogen atmosphere at a rate of 10 °C/min. The chemical structure of PP bags and C-Dots was characterized using a Nicolet iS50 Fourier transform infrared (FTIR) spectrometer (Thermo Fisher Scientific, USA). A JEOL JEM-1230 transmission electron microscope (TEM) (JEOL, Japan) detected the formation, morphology, and size distribution of C-Dots. UV-Vis absorption spectra were recorded using a Cary 7000 universal measurement spectrophotometer (UMS, Agilent Technologies, USA), with a wavelength range of 200–800 nm. Moreover, the band gap energy was calculated as:

$$(\alpha\, h\nu)^{1/n} = A(h\nu - E_g) \quad (1)$$

where α is the absorption coefficient, hν is the photon energy, A is a proportionality constant, and E_g is the band gap energy. The exponent n depends on the type of electronic transition. For direct transitions, the band gap was determined by plotting $(\alpha\, h\nu)^2$ as a function of hν and extrapolating the linear region of the curve to the hν-axis at α = 0 [29, 30].

3. Results and discussion

The thermal behavior of waste PP was investigated using TGA and DSC, as shown in Figures 2(a) and (b). These analyses provide insights into the thermal stability, decomposition characteristics, and phase transitions of waste PP, to facilitate and optimize its use as a precursor for C-dots synthesis. Additionally, these tests offer valuable information to identify any additives or impurities in the waste plastic, which could influence the final properties.

In the TGA analysis (Figure 2(a)), the material exhibits a thermal onset at 250 °C, with the decomposition process completing around 354 °C. This indicates that the material remains stable up to 250 °C, then the degradation process starts progressively, with complete decomposition occurring at 354 °C. The DSC analysis (Figure 2(b)) shows no significant thermal degradation within the temperature range of 0 °C to 250 °C, with a melting temperature of around 167 °C. By correlating the DSC and TGA results, it can be concluded that the material undergoes softening (onset) around 154 °C, followed by thermal degradation starting at 250 °C. These results suggest that 300 °C is an optimal temperature for the synthesis of C-Dots, as it allows for controlled thermal degradation while avoiding the complete decomposition of the material around 354 °C. This temperature ensures controlled degradation, promoting carbonization, while preventing complete material decomposition, thus facilitating the formation of C-Dots.

The FTIR analysis of the PP and C-Dots is shown in Figure 2(c). The peak around 2951 cm^{-1} is associated with the asymmetrical stretching of the $-CH_3$ group, and its intensity decreased in the C-Dots spectrum, indicating that PP conversion occurred [12]. The less intense symmetrical bending peaks at 1455 cm^{-1} and 1376 cm^{-1}, attributed to the $-CH_3$ group, provide evidence for the substantial reduction of PP into C-Dots. The FTIR spectrum of C-Dots reveals distinct new absorption peaks compared to PP, suggesting the formation of new functional groups or structural modifications associated with the conversion process.

© 2025 The Authors. This article is licensed under a Creative Commons Attribution 4.0 International License.

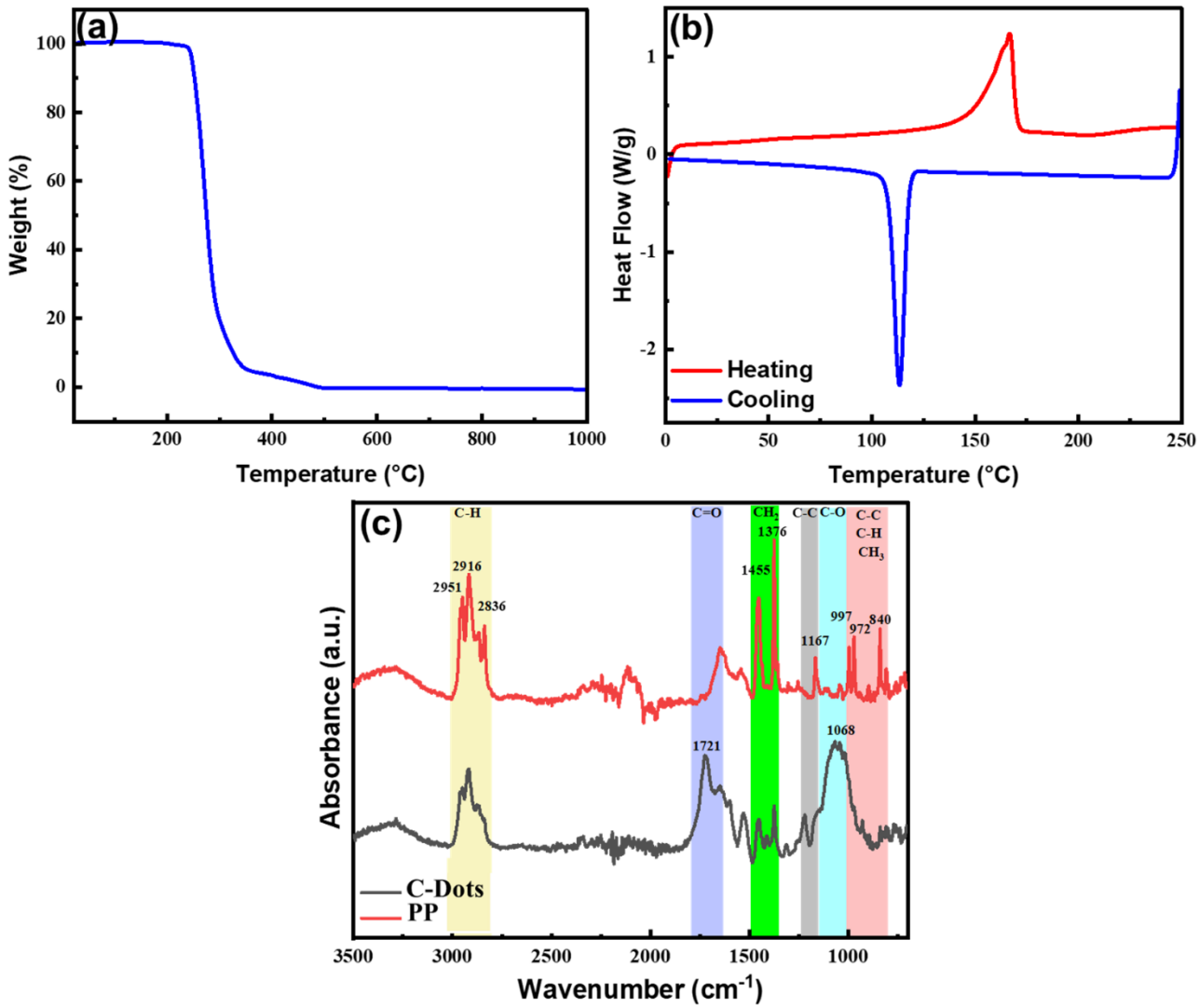

Figure 2. Characterization of waste PP and synthesized C-Dots: (a) TGA and (b) DSC of waste PP, as well as (c) FTIR spectra of waste PP and synthesized C-Dots.

During PP waste heating, the carbon chains react with oxygen from the surrounding environment. This interaction results in the formation of carbonyl groups (C=O), which are observed at 1721 cm^{-1}. These carbonyl groups are a key structural component of polymer C-Dots. A peak around 1068 cm^{-1} is typically attributed to the stretching vibrations of C-O bonds, especially in molecules with hydroxyl (-OH), ether (C-O-C), or ester (-COO-) functionalities [31]. This peak reflects the presence of oxygen-containing functional groups on the C-Dots surface, which are commonly introduced during the thermal treatment involving the polymerization, oxidation, and carbonization of PP [32]. Surface oxygen-containing groups play a crucial role in determining the solubility, stability, and photophysical properties of C-Dots. For instance, hydroxyl or ether groups contribute to hydrophilicity and facilitate interactions with different surrounding media, making the C-Dots suitable for bioimaging or sensing applications. These methods introduce functional groups enhancing fluorescence and modulating electronic properties.

High-resolution TEM analysis of C-Dots can provide valuable insights into their morphology and size distribution. TEM images shown in Figure 3(a) revealed that the carbon particles are spherical and well dispersed (no agglomeration). The conversion method used in this

© 2025 The Authors. This article is licensed under a Creative Commons Attribution 4.0 International License.

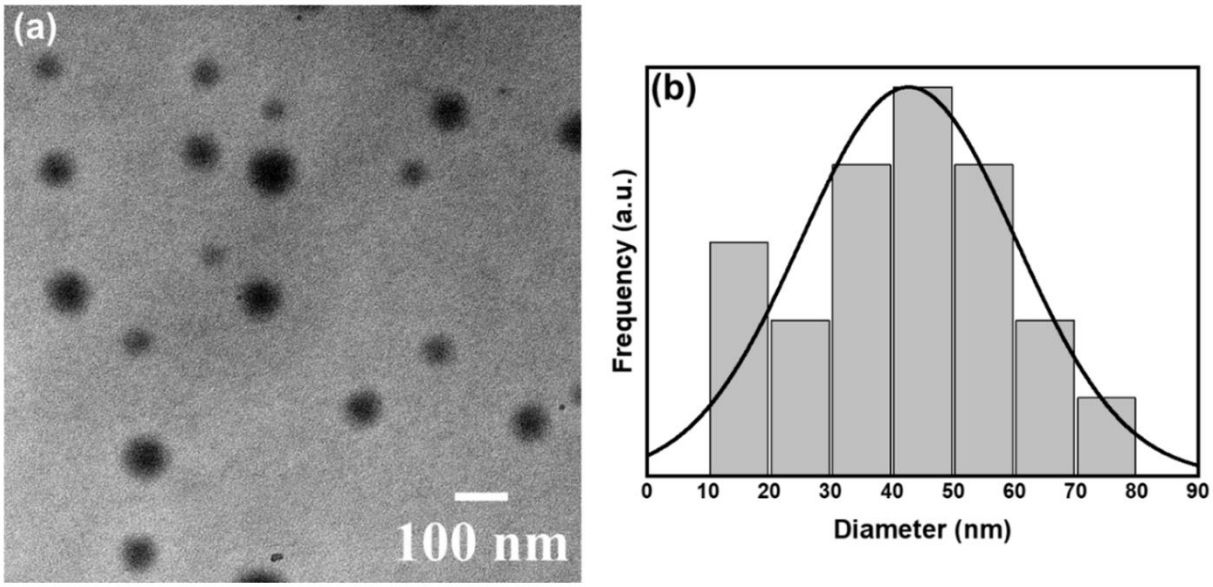

Figure 3. Morphological analysis of the C-Dots: (a) TEM image and (b) particle size distribution.

study successfully produced particles with minimal aggregation and a uniform size distribution with diameters ranging from 11 to 73 nm. The particles exhibit an average size of 43 nm with a standard deviation (SD) of 17 nm, suggesting good uniformity in the synthesis process (Figure 3(b)). The combination of structural and chemical analysis indicates that these particles are well-suited for advanced applications, such as electrode materials in lithium-ion batteries or as supports in catalysis.

Figure 4(a) presents the UV-Vis absorption spectrum of the synthesized C-Dots. An absorption peak around 250 nm is observed, which is commonly attributed to π-π* electronic transitions of aromatic sp^2 domains in the carbon core [16]. This feature is characteristic of graphitic domains within the C-Dots structure, which significantly contributes to their optical properties. The weak absorption peak around 280 nm is associated with n-π* transitions. This peak also provides valuable information about the surface chemistry of the C-Dots, which plays a

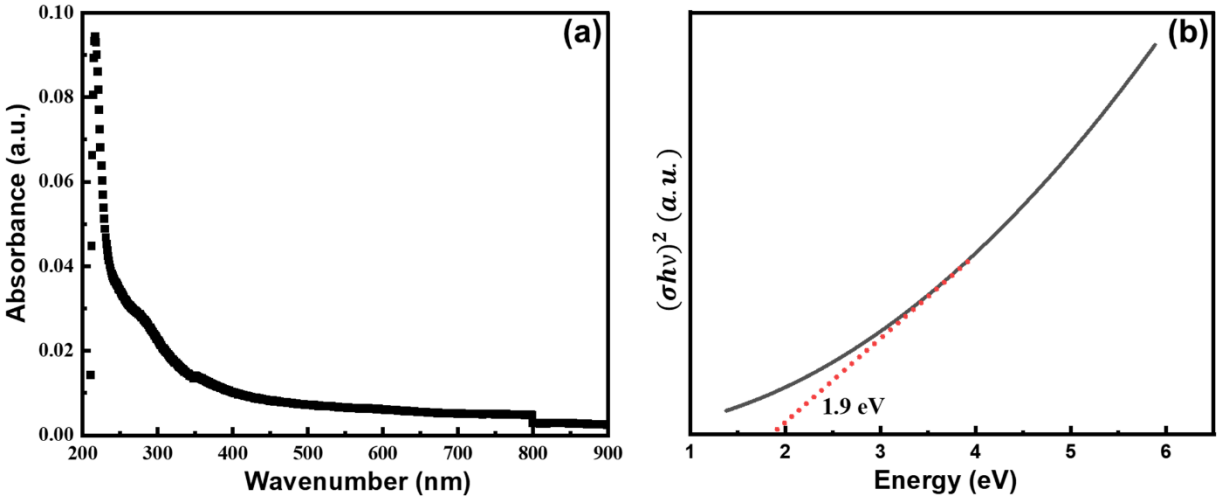

Figure 4. (a) UV-Vis absorption spectrum and (b) band gap energy estimation of C-Dots derived from waste PP.

© 2025 The Authors. This article is licensed under a Creative Commons Attribution 4.0 International License.

crucial role in determining their photophysical behavior and interaction with their environment. These transitions arise from non-bonding electron pairs present in surface functional groups, such as carbonyl (C=O) or hydroxyl (-OH), commonly introduced during the C-Dots synthesis [32].

In addition, the band gap energy of the C-Dots shown in Figure 4(b), estimated at 1.9 eV. This suggests a significant quantum confinement effect which is influenced by the size, surface functionalization, and chemical composition of the C-Dots [33]. Aji et al. showed that decreasing the size of C-Dots from 15 nm to 8 nm increased the band gap energy from 2.8 eV to 3.45 eV [13]. In microwave radiation techniques, increasing the power results in a smaller size of the material and increases the C-Dots' energy band gaps (2.47–2.53 eV), remaining within the typical range of 1.5–3.5 eV [34]. In addition, the band gap energy decreases with different dopant types, reaching 2.14 eV for pyridine N, 1.94 eV for amino N, and 1.54 eV for C=O groups [35].

The narrow band gap is indicative of the nanometer-scale dimensions of the C-Dots and the electronic structure modulated by both core size and surface states. A band gap of this magnitude implies that the C-Dots can absorb visible light and positions them as versatile materials for light-harvesting and imaging applications, suggesting potential for optoelectronic, photocatalysis, and bioimaging. The combination of π-π* transitions, surface-related n-π* features, and the observed band gap energy underscores the interplay between the intrinsic core structure and the surface chemistry of the C-Dots. This unique optical profile makes them promising materials for diverse applications requiring tunable electronic and photonic properties. Table 1 compares the C-dots prepared from various polymeric waste materials and techniques.

4. Conclusions

This work investigated the synthesis of carbon dots (C-Dots) from polypropylene (PP) waste (flexible food packaging), presenting an energy-efficient and sustainable approach to plastic waste management. The conversion process was characterized by FTIR analysis,

Table 1. Synthesis of C-Dots from different sources of waste materials

Precursor	Method	Absorption peaks (nm)	Size (nm)	Functional groups	Application	Reference
Plastic waste (polybags, cups, bottles)	Thermal calcination	260	5-30	-OH, -COOH	Analytical applications/ selective Cu^{2+} ions sensing	[31]
Plastic wastes (PP, PE, PS, etc.)	Oxidative acid treatment	-	4-7	-OH, C=O, C-O, C–O–C, -COOH, $-SO_3H$	O_2 harvesting	[36]
PE plastic waste	Acid-mediated plastic charring/chemical oxidation	209, 215, 300, 350	5–7	-OH, -COOH, Sulfate/ Sulfonate	Photocatalyst/ O_2 harvesting	[37]
PET bottles	Pyrolysis/ hydrothermal	-	1.3–4.0	Oxygen-containing groups	Nano-priming agents	[38]
Medical plastic waste	Thermal calcination/ hydrothermal procedure	220-280	5-10	-OH, -COOH, C=O, $-NH_2$	Fe^{3+} ions sensor	[39]
HDPE plastic bags	Pyrolysis-sonication-hydrothermal	290	1-4.5	-OH, -COOH, C=O	Fe^{3+} ions sensor	[40]
Polylactide	One-pot hydrothermal	240, 280	2.5-3.5	-OH, -COOH	-	[15]
Nylon 66 waste fibers	Hydrothermal	251	2.3-8.2	-OH, -COOH, $-NH_2$	Fe^{3+} and pH sensors/ fluorescent inks for encryption and information storage	[41]
PP plastic waste	Thermal/solvothermal process	250, 280	11-73	-OH, -COOH	Bioimaging, energy conversion, and sensing	This work

Notes: PE: Polyethylene; PET: Polyethylene terephthalate; HDPE: High-density polyethylene.

© 2025 The Authors. This article is licensed under a Creative Commons Attribution 4.0 International License.

which confirmed the presence of oxygen-containing functional groups in the C-Dots. The carbon-based spherical dots with an average particle size of 43 nm were observed via TEM which validated the formation of nanoparticles. Based on the UV-Vis results, this material exhibits unique optical properties with an electronic band gap energy of 1.9 eV making it suitable for a wide range of applications in optoelectronic, photocatalysis, and bioimaging. The bottom-up synthesis described here is straightforward, free of catalysts, and relies on available recycled materials, offering a practical and scalable option for industrial applications.

Conflict of Interest

The authors declare no conflict of interest.

References

1. N. Evode, et al. Plastic waste and its management strategies for environmental sustainability. *Case Studies in Chemical and Environmental Engineering*, **2021**, *4*, 100142.

2. N. Singh and T.R. Walker. Plastic recycling: A panacea or environmental pollution problem. *Npj materials sustainability*, **2024**, *2*, 17.

3. I. Vollmer, et al. Beyond Mechanical Recycling: Giving New Life to Plastic Waste. *Angewandte Chemie (International ed. in English)*, **2020**, *59*, 15402.

4. R. Kumar, et al. Mechanical, chemical, and bio-recycling of biodegradable plastics: A review. *Science of The Total Environment*, **2023**, *882*, 163446.

5. H. Ahmad and D. Rodrigue. Upcycling of recycled polyethylene for rotomolding applications via dicumyl peroxide crosslinking. *Journal of Applied Polymer Science*, **2024**, *141*, e56236.

6. T.H. Epps, et al. Sustainability of Synthetic Plastics: Considerations in Materials Life-Cycle Management. *JACS Au*, **2021**, *2*, 3.

7. M. Abdelhameed, et al. High-yield, one-pot upcycling of polyethylene and polypropylene waste into blue-emissive carbon dots. *Green Chemistry*, **2023**, *25*, 1925.

8. T. Kuang, et al. Functional carbon dots derived from biomass and plastic wastes. *Green Chemistry*, **2023**, *25*, 6581.

9. A. Vibhute, et al. Fluorescent carbon quantum dots: Synthesis methods, functionalization and biomedical applications. *Applied Surface Science Advances*, **2022**, *11*, 100311.

10. Arpita, et al. Plastic Waste-Derived Carbon Dots: Insights of Recycling Valuable Materials Towards Environmental Sustainability. *Current pollution reports*, **2023**, *9*, 433.

11. Z. Feng, et al. Carbon dot/polymer nanocomposites: From green synthesis to energy, environmental and biomedical applications. *Sustainable Materials and Technologies*, **2021**, *29*, e00304.

12. Y. Yang, et al. Polypropylene-Derived Luminescent Carbon Dots. *ACS Materials Letters*, **2024**, *6*, 1968.

13. M.P. Aji, et al. Polymer carbon dots from plastics waste upcycling. *Environmental Nanotechnology, Monitoring & Management*, **2018**, *9*, 136.

14. H. Jung, et al. Review of polymer technologies for improving the recycling and upcycling efficiency of plastic waste. *Chemosphere*, **2023**, *320*, 138089.

15. A. Lauria and E. Lizundia. Luminescent carbon dots obtained from polymeric waste. *Journal of Cleaner Production*, **2020**, *262*, 121288.

16. R. Wang, et al. Preparation of Carbon Dots from PET Waste by One-step Hydrothermal Method and its Application in Light Blocking Films and LEDs. *Journal of Fluorescence*, **2023**, *33*, 1305.

17. J. Huang, et al. Solid protonic acids and luminescent carbon dots derived from waste expanded polystyrene. *Materials Letters*, **2014**, *117*, 112.

18. Z. Hallaji, Z. Bagheri, and B. Ranjbar. The role of fluorescent carbon dots in the fate of plastic waste. *Journal of Environmental Chemical Engineering*, **2023**, *11*, 110322.

19. A. Alsabri, F. Tahir, and S.G. Al-Ghamdi. Environmental impacts of polypropylene (PP) production and prospects of its recycling in the GCC region. *Materials Today: Proceedings*, **2022**, *56*, 2245.

20. L. Baltes, et al. Differential scanning calorimetry—a powerful tool for the determination of morphological features of the recycled polypropylene. *Journal of Thermal Analysis and Calorimetry*, **2019**, *138*, 2399.

21. C. Budiyantoro, H. Sosiati, and J.W. Joharwan. The influence of the number of recycling cycles on the thermal and physical properties of polypropylene. *Jurnal Polimesin*, **2023**, *21*, 2023.

22. J. Gong, X. Chen, and T. Tang. Recent progress in controlled carbonization of (waste) polymers. *Progress in Polymer Science*, **2019**, *94*, 1.

23. V. Ramanan, et al. Green Synthesis of Multifunctionalized, Nitrogen-Doped, Highly Fluorescent Carbon Dots from Waste Expanded Polystyrene and Its Application in the Fluorimetric Detection of Au3+ Ions in Aqueous Media. *ACS Sustainable Chemistry & Engineering*, **2018**, *6*, 1627.

24. S. Singh, N. Shauloff, and R. Jelinek. Solar-Enabled Water Remediation via Recyclable Carbon Dot/Hydrogel Composites. *ACS Sustainable Chemistry & Engineering*, **2019**, *7*, 13186.

© 2025 The Authors. This article is licensed under a Creative Commons Attribution 4.0 International License.

25. F. Mahdavian, et al. Polyethylene glycol-impregnated carbon quantum dots-phenolic phase change composites for highly efficient thermal energy storage. *Carbon*, **2024**, *219*, 118840.

26. N.K. Khairol Anuar, et al. A Review on Multifunctional Carbon-Dots Synthesized From Biomass Waste: Design/ Fabrication, Characterization and Applications. *Frontiers in Energy Research*, **2021**, *9*, 626549.

27. M. Das, et al. Repurposing the domestic organic waste into green emissive carbon dots and carbonized adsorbent: A sustainable zero waste process for metal sensing and dye sequestration. *Journal of Environmental Chemical Engineering*, **2021**, *9*, 106312.

28. X. Li, et al. Green synthesis of carbon quantum dots from wasted enzymatic hydrolysis lignin catalyzed by organic acids for UV shielding and antioxidant fluorescent flexible film. *Industrial Crops and Products*, **2022**, *188*, 115568.

29. C.S. Pathak, et al. Blue light emission from barium doped zinc sulfide nanoparticles. *Ceramics International*, **2012**, *38*, 5497.

30. J. Dharma and A. Pisal, *Simple Method of Measuring The Band Gap Energy Value of TiO2 in the Powder Form Using a UV/Vis/NIR Spectrometer*. **2009**, PerkinElmer. p. 1.

31. S. Chaudhary, et al. Upcycling of plastic waste into fluorescent carbon dots: An environmentally viable transformation to biocompatible C-dots with potential prospective in analytical applications. *Waste Management*, **2021**, *120*, 675.

32. K. Tungare, et al. Synthesis, characterization and biocompatibility studies of carbon quantum dots from Phoenix dactylifera. *3 Biotech*, **2020**, *10*, 540.

33. B. Zhao, et al. Narrow-bandwidth emissive carbon dots: A rising star in the fluorescent material family. *Carbon Energy*, **2022**, *4*, 88.

34. H. Sutanto, et al. High green-emission carbon dots and its optical properties: Microwave power effect. *AIP Advances*, **2020**, *10*, 055008.

35. J. Yu, et al. Luminescence Mechanism of Carbon Dots by Tailoring Functional Groups for Sensing Fe(3+) Ions. *Nanomaterials*, **2018**, *8*, 233.

36. B. Kommula, et al. Landscaping sustainable conversion of waste plastics to carbon dots and enormous diversity in O2 harvesting, hypoxia, autophagy. *Carbon*, **2023**, *213*, 118304.

37. B. Kommula, et al. A two-step strategy for residue-free chemical conversion of plastic waste to carbon dots: Upscaling and solvent recycling prospects. *Carbon*, **2025**, *234*, 119960.

38. L. Liang, S.C. Wong, and G. Lisak. Effects of plastic-derived carbon dots on germination and growth of pea (Pisum sativum) via seed nano-priming. *Chemosphere*, **2023**, *316*, 137868.

39. M. Kumari, G.R. Chaudhary, and S. Chaudhary. Transformation of medical plastic waste to valuable carbon dots: A sustainable recycling of medical waste to efficient fluorescent marker. *Journal of Molecular Liquids*, **2024**, *395*, 123910.

40. R. Lestari, et al. Transforming high-density polyethylene plastic bags into eco-friendly carbon dots for detecting ferric (Fe3+) ions. *Diamond and Related Materials*, **2023**, *139*, 110271.

41. R. Wang, et al. Simple and Green Synthesis of Carbonized Polymer dots from Nylon 66 Waste Fibers and its Potential Application. *ACS omega*, **2021**, *6*, 32888.

© 2025 The Authors. This article is licensed under a Creative Commons Attribution 4.0 International License.